DESIGN OF WIRELESS OPTICAL MIMO LINKS

DESIGN
OF
WIRELESS OPTICAL MIMO LINKS

BY
AWAD DABBO , B. Eng.

A THESIS
SUBMITTED TO THE
DEPARTMENT OF ELECTRICAL & COMUPUTER ENGINEERING
AND THE SCHOOL OF GRADUATE STUDIES
OF MCMASTER UNIVERSITY
IN PARTIAL FULFILLMENT OF THE REQUIREMENTS
FOR THE DEGREE OF
MASTER OF APPLIED SCIENCE

Master of Applied Science (2009)
(electrical & computer engineering)

McMaster University
Hamilton, Ontario, Canada

TITLE:	Design of Wireless Optical MIMO Links
AUTHOR:	Awad Dabbo B. Eng.
SUPERVISOR:	Dr. Steve Hranilovic
NUMBER OF PAGES:	xv, 160

Abstract

Wireless optical MIMO links can achieve very high data transmission rates by exploiting spatial diversity at a grand scale. Although such links can achieve high rates, their practical implementation remains challenging. The difficulty in implementation arises due to the complex transmitter and receiver designs required to overcome the channel impairments. This thesis considers practical transmitter and receiver designs for the wireless optical MIMO channel in the presence of channel impairments.

In the first part of the thesis, two techniques to improve channel capacity for wireless optical MIMO channels are presented. The first technique uses multi-level halftoning to reduce quantization noise power. For quantization noise-limited systems, increasing the number of quantizer levels provides gains in capacity. For example, at a rate of 200fps, a four-level quantizer gives approximately a two-fold increase in capacity over a binary-level quantizer for all frame sizes considered. The second technique uses higher order noise shaping to shape the quantization noise to the out-of-band spatial frequency spectrum. This technique is shown to be useful when the number of levels is small, i.e., near 2.

In the second part of the thesis, the receiver design for wireless optical MIMO channels with magnification is considered. The work done in this part constitute a step towards the practical implementation of such links since it is the first time the effects of spatial transformations are considered. Signal magnification introduces varying spatial frequency inter-channel interference (SF-ICI) at the receiver. A novel receiver design that uses complex windowing with decision feedback equalization is used to equalize the SF-ICI in spatial frequency domain. For SF-ICI limited channels, the novel receiver design achieved a low bit-error rate compared with rectangular windowing with zero-forcing equalization. However, for noise limited channels, rectangular windowing with zero-forcing equalization is the receiver design of choice.

Acknowledgements

I would like to extend my sincere gratitude to my thesis supervisor, Dr. Steve Hranilovic. Throughout my study period, he provided guidance, motivation, and lots of good ideas. In addition he was always available and willing to help. I would have been lost without him. I would also like to thank Dr. Tim Davidson for his valuable feedback on the projects undertaken in his optimization and digital communication courses.

I am indebted to Mr. Mohamed D.A. Mohamed for his continuous support and help during my research period, and for reviewing an earlier version of this thesis. I would also like to extend my thanks to my lab colleagues, especially Mohamed D.A. Mohamed and Ahmed Farid, for the many interesting discussions, and their valuable insight into optical communications. I would also like to extend many gratitude to Anthony Chiarelli for his help in implementing some of the practical aspects of the prototype link I built during the course of my masters thesis.

I would also like to thank all the technical and administrative staff in the electrical and computer engineering department of McMaster University for helping the department run smoothly, and for assisting me in many different ways. Cosmin Coroiu, Cheryl Gies, Helen Jachna, Terry Greenlay and Steve Spencer deserve a special mention.

Finally, i am forever indebted to my parent for their encouragement and endless support when it was most required.

Contents

List of Figures

List of Tables

Abbreviations

1D	One Dimensional
2D	Two Dimensional
BER	Bit Error Rate
CCD	Charged Couples Device
CMOS	Complementary Metal Oxide Semiconductor
DFE	Decision Feedback Equalizer
DFT	Discrete Fourier Transform
DLP	Digital Light Projection
DMD	Digital Micro-mirror Device
DMT	Discrete Multi-Tone
fps	frames per second
FTER	Feedback to Total Energy Ratio
Gbps	Gega bits per second
HDS	Holographic Data Storage
ICI	Inter Channel Interference
IDFT	Inverse Discrete Fourier Transform
ISI	Inter Symbol Interference
LCD	Liquid Crystal Display
LED	Light Emitting Diode
LD	Laser Diode

Mbps	Mega bits per second
MIMO	Multiple Input Multiple Output
OTF	Optical Transfer Function
OLED	Organic Light Emitting Diode
PAN	Personal Area Network
PSD	Power Spectral Density
PSF	Point Spread Function
QAM	Quadrature Amplitude Modulation
RF	Radio Frequency
SDMT	Spatial Discrete Multi-Tone
SF-ICI	Spatial Frequency Inter Channel Interference
SINR	Signal Interference to Noise Ratio
SISO	Single Input Single Output
SLM	Spatial Light Modulator
SNR	Signal to Noise Ratio
ZF	Zero Forcing Equalizer

Symbols

$[.]$	Discrete Domain
$(.)$	Continuous Domain
$*$	Continuous two-dimensional convolution
$\bigotimes$	Two dimensional discrete convolution
$\mathcal{Q}$	Commutative distribution function
Δ	Quantizer step size
Δ_1, Δ_2	Translation in space in each dimension
θ	Angle of rotation
ϵ	Optical magnification in space
σ_H^2	A measure of the bandwidth of the optical transfer function
σ_q^2	Variance of quantization noise (Quantization noise power)
σ_v^2	Variance of the input signal to the quantizer
σ_x^2	Variance of the input signal (Average electrical power per bin)
σ_ψ^2	Power of channel noise
ξ_j	Energy of the error diffusion filter j
Φ_x	Power allocation matrix
$\Phi\tilde{q}$	Power spectral density of shaped quantization noise
$\Phi_{\tilde{\psi}}$	Power spectral density of the effective channel noise
ψ	Channel noise in space
Ψ	Spatial frequency response of the channel noise

$\tilde{\Psi}$	Spatial frequency response of the effective channel noise
C	Aggregate channel capacity
d	Separation distance between constellation points
D_r	Pixel spacing at the receiver
D_t	Pixel spacing at the transmitter
f_1, f_2	Continuous spatial frequency coordinates
$\tilde{f}_1, \tilde{f}_2$	Transformed continuous spatial frequency coordinates
h	Channel point spread function
H	Channel optical transfer function
i	$\sqrt{-1}$
j	Error diffusion filter
J	Spatial frequency spectrum of the error diffusion filter
k_1, k_2	Discrete spatial frequency coordinates at the transmitter
$\tilde{k}_1, \tilde{k}_2$	Discrete spatial frequency coordinates at the receiver
L	Number of quantization levels (Halftoning levels)
m_1, m_2	Discrete spatial coordinates at the receiver
M_1, M_2	Size of received frame (pixels)
n_1, n_2	Discrete spatial coordinates at the transmitter
N_1, N_2	Size of transmit frame (pixels)
P	Penalty function
P_t	Average optical power
q	Quantization noise
Q	Spatial frequency spectrum of the quantization noise
$\tilde{q}$	Shaped Quantization noise
$\tilde{Q}$	Spatial frequency response of the shaped quantization noise
t_1, t_2	Continuous spatial coordinates
$\tilde{t}_1, \tilde{t}_2$	Continuous coordinates of the spatial transformed image
x	Continuous-tone spatial image

X	Spatial frequency spectrum of the Continuous tone image
x'	Halftoned spatial image
X'	Spatial frequency spectrum of the Halftoned image
x_T	Transmit image in space
$\tilde{x}_T$	Transformed transmit spatial image
$\tilde{X}_T$	Spatial frequency spectrum of the transformed transmit image
$\hat{X}_T$	Estimated transmit frame at the receiver side
x_R	Received spatial image
X_R	Spatial frequency spectrum of the received image
U	A weighing factor signifying the spatial frequency varying ICI
v	Input signal to the quantizer
w	Windowing function
W	Spatial frequency response of the windowing function
y	Optimization vector with filter parameters

Chapter 1

Introduction

1.1 Overview and Motivation

As advancements in semiconductor technology keep pushing the envelop on the size, processing power, and functionality of electronic devices, portable electronic devices are gaining popularity. Such devices include cellular telephones, laptop computers, personal digital assistants and portable music/video players. In the late 1990's, there has been an emerging trend towards joint operation of the devices, where the devices interact with each other wirelessly, to enhance the user experience. Joint operation is done via a personal area network (PAN), which connects and exchanges information among devices [3, 4]. As portable devices increase in complexity and functionality, the need for high rate communication is likely to grow. This growth is largely owed to the increase of digital audio/video exchange among devices.

At present, Bluetooth technology remains the preferred choice for implementing PANs [5]. Bluetooth is a wireless protocol utilizing short-range communication technology, facilitating both voice and data transmissions over short distances to different devices [6]. Bluetooth communication is done over radio frequency (RF) with data rates up to 3 Mbps [6] for "Bluetooth version 2.0 + EDR". Due to this low transfer rate, new methods for exchanging information between devices must be devised to keep up with the increase in demand for high data rate communication systems. Recently, WiFi technology has been considered as a potential candidate to replace Bluetooth technology in PANs [7]. Although WiFi (IEEE 802.11) can achieve data rates as high as 54 Mbps [8], it consumes large amounts of power compared with Bluetooth. Moreover, this technology operates in the 2.4 GHz frequency band, thus making it susceptible to interference from a range of wireless devices. Such devices include microwave ovens, Bluetooth devices, baby monitors and cordless phones. Another possible candidate for implementing PANs, is the use of wireless optical links. Wireless optical links has been shown to achieve high data rates in the range of Gbps [9, 10], without interfering with other devices.

In the last decade, it has been shown that introducing transmit and receive diversity in radio frequency (RF) systems is beneficial. By introducing this diversity to RF systems, improvements in data rate, error performance, and capacity have been achieved [11]. Systems utilizing transmitter and receiver diversity are termed multiple-input multiple-output (MIMO) RF systems. In contrast, Bluetooth and WiFi utilize a single transmit and receive antennas, thus dubbed single-input single-output (SISO) RF systems. Currently, efforts are begin made to standardize RF MIMO in WiFi systems (IEEE 802.11n). By applying MIMO technology to WiFi systems, data rate is expected to increase to at least 100 Mbps [12].

Note that in a practical MIMO implementation, the rates achieved are less than the theoretical capacity limits. The reduction in the achieved rate is due to correlation between the signal in each receive antenna [13, 14]. This effect has been investigated theoretically in [15, 16], and practically verified in [17]. In [13] it was shown that the correlation is proportional to the separation distance between the antennas. In [18], a MIMO link using dipole and small ceramic antennas operating at

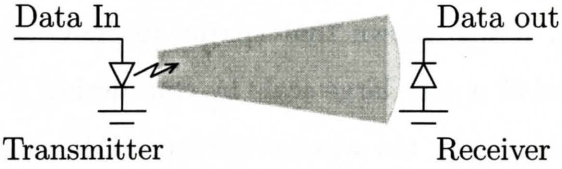

FIGURE 1.1: A one-dimensional optical intensity channel.

2.4/2.6 GHz was simulated. From this experiment it was shown that if the antenna separation is 0.1λ, then the correlation between the received signals is 0.8, where λ is the wavelength. Based on the previous discussion, one can conclude that in RF MIMO system, the required separation distance between the antennas is larger than that of the Optical MIMO system. As a result, the number of antennas in a practical RF MIMO system is limited. In wireless optical systems, transmit and receive diversity can also be implemented to reap considerable benefits. Since optical wavelengths are orders of magnitude shorter that RF wavelengths, an optical MIMO system can be implemented practically at a large scale. Thus achieving an immense increase in channel capacity.

Wireless optical MIMO systems are realized by using a two-dimensional array of coupled optical intensity channels. An optical intensity channel uses intensity modulation and direct detection. Meaning that information is transmitted by modulating the instantaneous intensity of a light source [19]. For a typical configuration, the transmitter is a light emitting diode (LED), and the receiver is a photodiode. Figure 1.1 shows the layout of an optical intensity channel. At the transmit side, the brightness of the LED changes in correspondence to an electrical data signal. At the receive side, the photodetector converts changes in light intensity to changes in electrical signal. The electrical signal is then decoded and the data extracted. Since data are modulated as an intensity, a line-of-sight between the transmitter and the receiver must be established to convey information. In addition, the optical signal must have a non-negative amplitude, and it's average and peak optical power are restricted due to skin and safety regulations [20].

In this section, it was shown that spatial diversity can be exploited in the wireless optical channel at a very large scale by considering a 2D array of optical intensity channels. Consequently, the wireless optical MIMO channel can achieve much higher data rates compared with their RF counterpart. Moreover, the use of optical wavelengths in data transmission adds a layer of security in a closed indoor environment. This layer of security is a direct result of requiring a line-of-sight between the transmitter and the receiver to establish communication. Unlike RF MIMO, wireless optical MIMO links utilize the unregulated optical spectrum. As a result, such links are not subject to spectrum licensing fees. Due to these benefits, the wireless optical MIMO channel presents a good choice for short-range, high data rate, low cost, and secure communication link.

1.2 Wireless Optical MIMO Applications

Current spatial light modulation technology can modulate millions of pixels (channels) independently. Moreover, these devices can operate at a very fast frame rate. As a result, wireless optical MIMO channels can provide high data rate. Due to their inherent high data transmission rates, wireless optical MIMO systems have found a niche in many future applications. Such applications include holographic data storage systems [21–23], optical interconnects [24, 25], two-dimensional (2D) bar codes [26, 27], and wireless optical MIMO communication systems [28–31].

1.2.1 Holographic Data Storage

Recently, the introduction of high-definition digital multimedia caused an increase in demand for realtime, high capacity storage systems. Although current serial storage technologies are keeping pace with the increase in demand, there is strong evidence that these technologies are approaching their fundamental limits [32]. Therefore, new storage techniques must be devised to cope up with future increase in demand. Holographic data storage (HDS) is a digital storage technology that is being considered as a replacement for current serial storage systems. In serial storage technologies, bits are stored individually on the surface of a storage medium. In contrast, holographic data storage stores pages of binary data throughout the volume of the recording medium [33, 34]. Due to the volumetric approach in storing information, such systems are theorized to achieve capacities exceeding 1 Tb/cm^3 [35]. Moreover, holographic data storage systems are expected to achieve data transfer rates exceeding 10 Gbps [36, 37]. In 2006, InPhase Technologies published a white paper reporting an achievement of 500 Gb/in^2 and a read/write rate of 13 MBytes/s and 23 MBytes/s respectively [38].

Figure 1.2, shows a typical setup for a holographic data storage system. To write data in a holographic data storage system, binary data are multiplexed spatially into two-dimensional images. A spatial light modulator modulates the data frame into a coherent image. The coherent image is then projected into a crystal, and is stored as an interference pattern with a reference beam. To recover the binary data, a reference beam is shined at the position where data is stored. A holographic reconstruction of the stored image is then projected onto a detector array [39]. The reconstructed frame is processed and binary data are extracted.

Holographic data storage systems suffer from many channel impairments, as is the case for other wireless optical MIMO based systems. These impairments affect the reliability of data detection. The major impairments are due to many sources of noise present, misalignment, and spatial inter-symbol interference (ISI) [21, 23, 40]. Much research is being done to increase the reliability of detection. In [41], a detection technique combining the application of the Viterbi algorithm across each row, with decision feedback from previous rows was introduced for ISI limited systems. In their work, the combined detector achieved a BER in the order of 10^{-4}, compared with

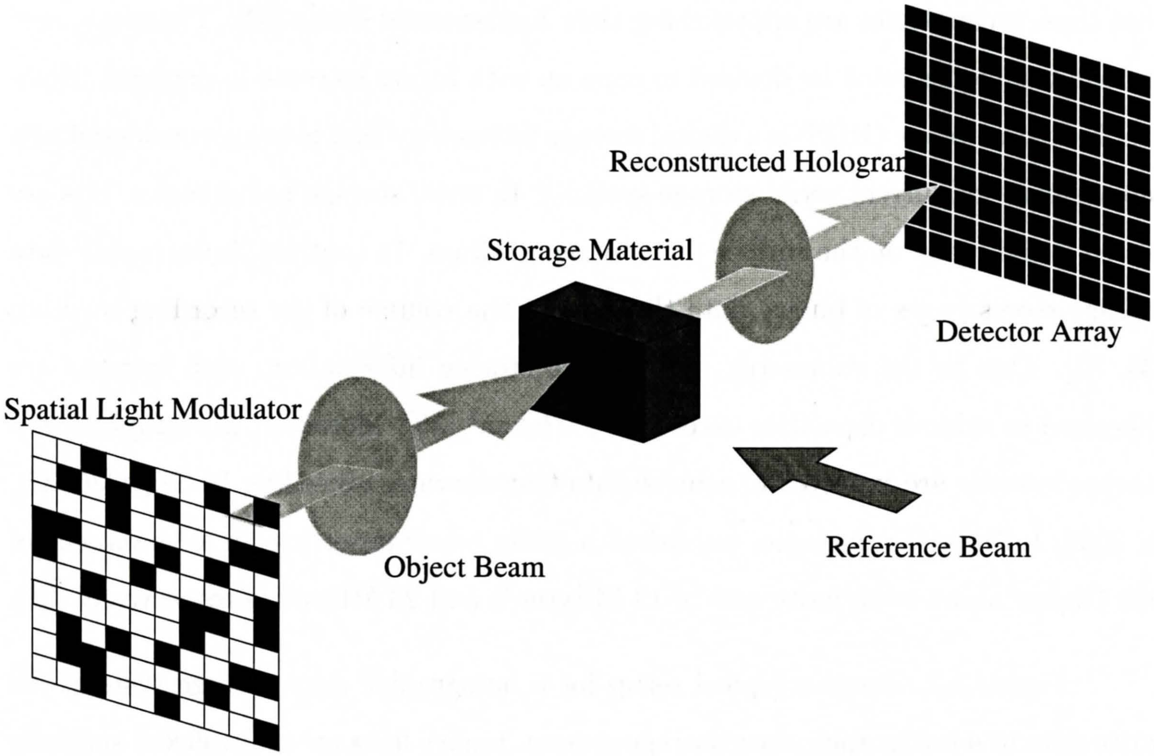

FIGURE 1.2: A holographic data storage system utilizing optical MIMO techniques.

10^{-1} for threshold detection. In [42], the authors considered using decision feedback equalization (DFE) with arbitration. In their work, the DFE algorithm was started from different locations in the image. The final value of each pixel was determined by comparing the output of all algorithm runs for that pixel position, and choosing the most common value. Other techniques to improve the BER performance is to consider constrained coding. In constrained coding, 2D codes are applied to load data into an image in a way that forbids some patterns from occurring. These patterns are associated with causing a high bit error rate. Therefore by removing theses patterns, the BER is reduced. In [43], a constrained code with code rate of 3/4 was applied to a 2D holographic data storage channels. In simulation, the new code achieved a BER on the order of 10^{-3} with a coding gain of 5 dB. To reduce the effect of misalignment the oversampling of holographic data images was considered in [44, 45]. In their work, the reconstructed hologram was over-sampled then resampled to reduce the effect of misalignment.

1.2.2 Optical Interconnects

As technological advancements in microelectronics push the envelope on the computational power of microprocessors, the need for higher data flow to and from the processor is required. Current technology rely on copper interconnects inlaid to printed circuit boards. However, as the operating frequency increases, the attenuation, crosstalk, and inductance in the copper wires constitute challenges during the design process [46]. Moreover, copper interconnects are near reaching their physical limit of 15 Gbps [47]. Currently, research is begin done to replace copper interconnects with optical ones. The use of optical interconnects is expected to eliminate many design problems [47], and achieve data rates exceeding 20 Gbps [46]. There exist a variety of optical interconnects, the most relevant to this work are two-dimensional wireless optical interconnects. In such systems, there are multiple interconnects working in parallel to communicate data at the chip-to-chip, board-to-board, or board-to-backplane levels.

In [48], a 4×4 wireless optical interconnect demonstrated with an aggregate data rate > 1.7 Gbit/s. A 256-channel bidirectional optical interconnect between two circuit boards was demonstrated in [49]. The link used an array of vertical cavity surface emitting lasers (VCSEL) and an array of photodetectors (PD) as a receiver. This demonstration proved the viability of free-space optical interconnects at the board level. As with any wireless optical MIMO system, spatial misalignment can degrade link performance. In [50], a real time active alignment system for wireless optical interconnects was demonstrated. Their proposed system for misalignment error compensation was demonstrated for a range of dynamic disturbances up to 118Hz.

1.2.3 Two-dimensional Barcodes

A barcode is machine readable, optical representation of an alphabetical and/or numerical sequence of symbols. This representation is commonly used for reliable and rapid identification of products, documents and people [51]. In recent years, barcodes have been integrated into a vast number of applications, some of which require a large number of symbols for identification. This led to the development of two dimensional barcodes. Two-dimensional barcodes are spatial codes that encode data symbols into patterns along two spatial dimensions. As a result of using spatial diversity, 2D barcodes have higher capacity than traditional 1D barcodes. There exist many variations of 2D barcodes. Figure 1.3 shows some examples of common 2D barcodes. From a communication perspective, the 2D barcode is equivalent to a pixelated transmitter. And the barcode scanner is equivalent to the receiver. To read a 2D barcode, a scanner captures an image of the 2D barcode. This image is then processed and data in each pixel detected. Blocks of pixels are then used to decode transmit symbols. For this channel, noise, spatial misalignment and ISI constitute the major sources for error. In [26, 27], the authors consider the design of such codes to increase the probability of correct detection.

1.2.4 Wireless Optical MIMO Communications

In an information age driven by the exchange of mass multimedia content, the need for secure and high data transmission rate links is impeccable. As a result, wireless optical MIMO systems are being contemplated for short-range indoor communication links. This is due to their high security and fast data transmission rates.

For wireless optical MIMO links, each transmit and receive element is termed a pixel, thus the name *pixelated optical transmission.* A typical configuration for a wireless optical MIMO communication channel is shown in Figure 1.4. For such

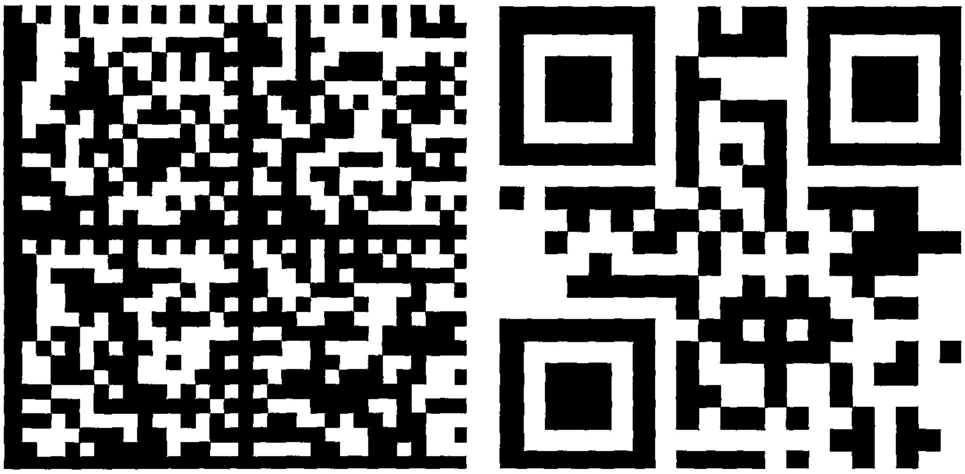

Data Matrix Barcode QR Barcode

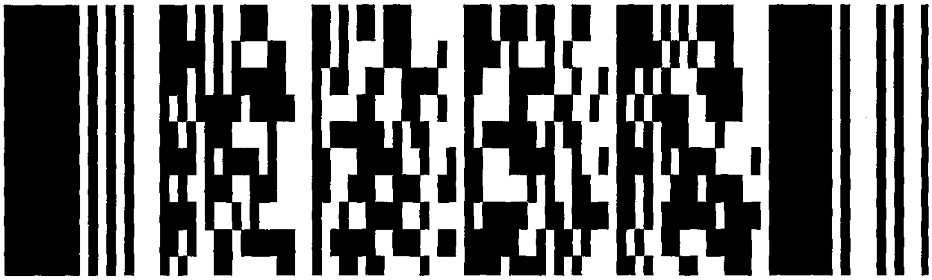

PDF417 Barcode

FIGURE 1.3: Various types of two-dimensional barcodes, (Generated online from [1]).

a channel, a spatial light modulator (SLM) is used as a transmitter, and a two-dimensional array of photodetectors is used as a receiver. To transmit information, data is multiplexed spatially by modulating the intensity of each transmit pixel at the SLM. Consequently, generating an intensity image corresponding to the input data. Note that the generated intensity image must satisfy non-negativity, and its average and peak powers must adhere to safety regulation as in [20]. At receive side, imaging optics project the transmit intensity image onto a two-dimensional photodetector array. The detector array samples the spatial intensity distribution of the projected image to create an electrical equivalent. The electrical signal is then processed to extract the transmitted data.

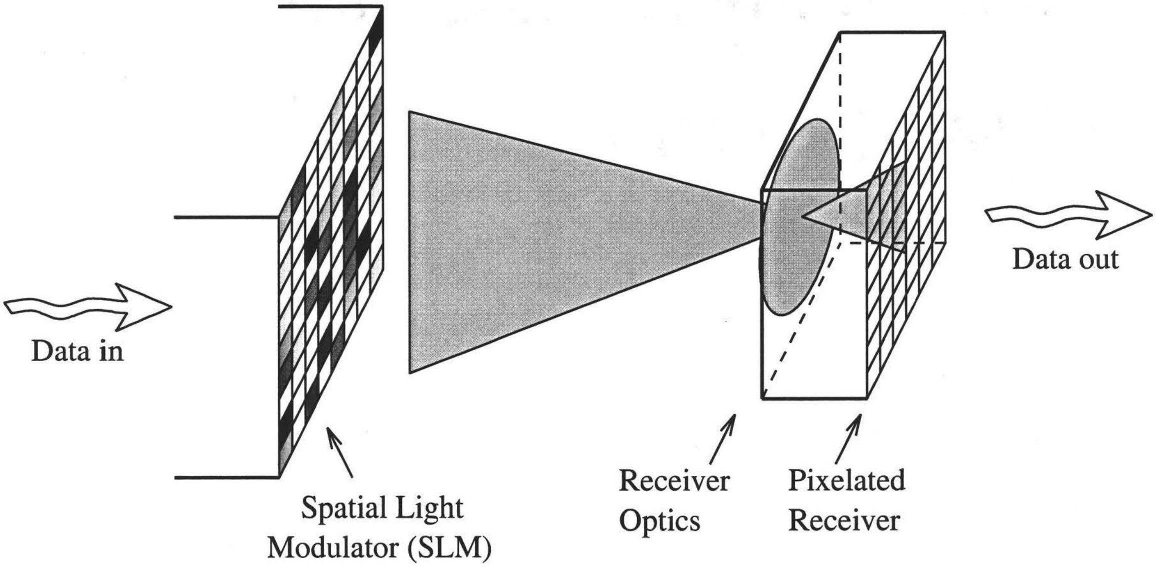

FIGURE 1.4: A wireless optical MIMO system.

In [30], a prototypical wireless optical MIMO communication system was implemented. The system was realized using a 512 × 512 pixel liquid crystal display with 256 intensity levels. The receiver consisted of a CCD digital camera with 154 × 154 pixels operating at 60 frames per second. In their work, data was multiplexed in spatial frequency domain using spatial discrete multi-tone modulation (SDMT) [52, Chapter 7]. By applying multi-level coding coupled with multi-stage decoding, the link achieved rates of approximately 17 kbits per frame, which is about 76% of estimated channel capacity [30].

In [31], the authors introduced binary halftoned SDMT modulation. In contrast to SDMT modulation, binary half-toned SDMT resulted in a great reduction in implementation complexity. Reduction in complexity was brought by limiting transmit intensity to a *binary* set, i.e. transmitter can only output two intensities on or off. Such transmitters are far simpler to build and can operate at very high frame rates (thousands of frames per second). A digital micro-mirror device (DMD) is an example of a binary transmitter [53]. As an example, a DMD device with a 1024 × 768 pixels, can operate at ≈ 10,000 frames per second [54], resulting in a maximum total data transmission rate of 1 GB/s. In [55], the channel capacity was simulated for a binary halftoned SDMT system, using actual channel measurements. The simulation predicted rates on the order of 450 Mbps for a 1m link using 0.5 megapixel arrays at 7000 frames per second.

In [56], the authors studies spatial multiplexing in optical wireless MIMO communications over indoor environments. In their work, a one-dimensional array of laser diodes acted as the transmitter, and an array of photodetectors acted as the receiver. Intensity modulation and direct detection was utilized to transmit information across the link. Using this system, the data was split into different streams for each transmitting element. For each transmitting element, the data was used to modulate its intensity. At the receiver, each photodiode received a weighted sum of the transmit intensities. As a result, the wireless optical MIMO channel was modeled as begin a spatial ISI channel. To equalize the spatial ISI, a system of linear equations was used to relate the received data with the transmit data. Then, joint equalization was performed to equalize the ISI. Note that joint equalization is computationally expensive for the wireless optical MIMO links considered in this work. This is due to the large number of transmitters and receivers used. A more detailed look at joint equalization is presented in Section 4.4.1.

1.3 Contributions

The goal of this research is to provide a foundation for the practical implementation of wireless optical MIMO communication links. In previous work done on optical MIMO communication channels, SDMT modulation was used to mitigate the effects of spatial misalignment [30]. Such a modulation scheme requires a complex design, thus limiting its practical implementation. Binary halftoned SDMT modulation was then introduced to reduce the complexity at the cost of reducing channel capacity [31].

In the first part of this thesis, methods to increase the channel capacity are introduced for halftoned SDMT systems. The first method uses multi-level halftoned SDMT which achieves gains in capacity, while maintaining low transmitter complexity. The second method considers the use of higher order noise shaping to realize gains in the capacity. While in other literature, noise shaping filters were designed heuristically [31]. In this thesis, optimization techniques are used to design the filters, in order to maximize the channel capacity.

In the second part of this thesis, a receiver is designed to counter the impact of channel impairments. In practice, wireless optical MIMO communication channels suffer from many channel impairments. Spatial misalignment, magnification and rotation are examples of such impairments. In previous research, the effects of magnification and rotation on transmit signals were ignored. Realizing such systems in practice is infeasible, especially for the indoor wireless optical MIMO communication systems considered in this work. The presence of such impairments in the channel causes severe inter-channel interference. Thus, causing a high probability of error. This thesis is novel because it considers a low complexity receiver design to overcome such impairments. The solution relies on a model that was derived to encompass the effects of spatial misalignment, magnification and rotation. With perfect knowledge of channel impairments, the channel model is used along with windowing techniques and decision feedback equalization to reduce the probability of error.

Moreover, a prototype optical wireless MIMO communication system was built. The system was used to characterize and quantify channel parameters. These measurements were used to simulate the channel capacity for binary halftoned SDMT systems. The results of this work were presented at the *International Conference on Communications* (ICC 2008) in Beijing, China [55]. These results were also used to estimate the channel capacity of multi-level halftoned systems with higher order noise shaping. The results were presented at the 24^{th} *Queens Biennial Symposium on Communications*, Kingston, ON [57].

1.4 Thesis Structure

In Chapter 1, the wireless optical MIMO channel was introduced. This subject was motivated by a brief discussion regarding some of its applications. In Chapter 2, the details of the channel model are discussed. The application of spatial discrete multitone modulation in wireless optical MIMO communication channels is discussed. A prototype wireless optical MIMO communication systems is presented. The prototype link is used to measure the channel parameters. Chapter 3 introduces multilevel halftoning and higher order noise shaping as methods to reduce the practical complexity of SDMT systems while enhancing the channel capacity. The channel capacity for multilevel SDMT systems is approximated. The chapter is concluded with some simulation results. In Chapter 4, the effects of translation, magnification and rotation on transmit SDMT signals are discussed and modeled. Detection techniques are developed to combat the effects of magnification. The thesis is concluded in Chapter 5, with some conclusions and future research directions.

FIGURE 1.4: A wireless optical MIMO system.

In [30], a prototypical wireless optical MIMO communication system was implemented. The system was realized using a 512×512 pixel liquid crystal display with 256 intensity levels. The receiver consisted of a CCD digital camera with 154×154 pixels operating at 60 frames per second. In their work, data was multiplexed in spatial frequency domain using spatial discrete multi-tone modulation (SDMT) [52, Chapter 7]. By applying multi-level coding coupled with multi-stage decoding, the link achieved rates of approximately 17 kbits per frame, which is about 70% of estimated channel capacity [30].

In [31], the authors introduced binary halftoned SDMT modulation. In contrast to SDMT modulation, binary half-toned SDMT resulted in a great reduction in implementation complexity. Reduction in complexity was brought by limiting transmit intensity to a *binary* set, i.e. transmitter can only output two intensities on or off. Such transmitters are far simpler to build and can operate at very high frame rates (thousands of frames per second). A digital micro-mirror device (DMD) is an example of a binary transmitter [53]. As an example, a DMD device with a 1024×768 pixels, can operate at $\approx$ 10,000 frames per second [54], resulting in a maximum total

Chapter 2

Channel Modeling, Modulation and Measurements

2.1 Background

In Chapter 1, the motivation behind applying spatial degrees of freedom in wireless optical channels was introduced. In such channels, spatial diversity is exploited at a grand scale by considering a large assembly of optical intensity channels. For the systems considered in this work, the number of optical channels is on the order of thousands. To effectively utilize the added spatial diversity, knowledge and understanding of the channel is essential. In this chapter, a wireless optical MIMO communication channel is studied, and a channel model is developed. The use of spatial discrete multi-tone modulation (SDMT) is discussed, and the channel capacity is approximated for SDMT modulated systems. A prototype wireless optical MIMO links is presented. The links is used to measure and quantify the channel parameters.

2.2 Channel Modeling

2.2.1 Channel Topology

Wireless optical MIMO channels require the transmit data to be in the field-of-view of the receiver, i.e., a line-of-sight must exist between both ends of the link. In the channels considered, there are two possible topologies that satisfy this condition. Figure 2.1(a) shows the first topology where the transmitter and the receiver are facing each other. As a result, there is a direct line-of-sight between both ends of the link. Figure 2.1(b) shows the second topology where the transmitter projects data images in the field-of-view of the receiver. Thus, there exist a direct line-of-sight between the projected transmit image and receiver. In both topologies, the transmit data image and the receiver elements are not assumed to be pixel-matched, only that their optical axis coincide so that the received image is an orthographic projection of the transmitted image.

To generate data images, the transmitter makes use of a two-dimensional (2D) spatial light modulator (SLM). By modulating each pixel, an intensity image is formed. For links utilizing the first topology, a liquid crystal display (LCD) [58], and organic light emitting diode (OLED) display [59], constitute two possible choices for a SLM. For the second topology, any SLM with light projection capabilities can be used. Examples of such technology include, liquid crystal on silicone (LCOS) [60], and digital light projection (DLP) technology. Digital light projection is based on a two-dimensional array of independently controlled digital micro-mirror devices (DMDs), where each mirror corresponds to a pixel in the projected image. The application of a positive voltage to the mirror, causes the mirror to tilt towards a light source, thus, forming a bright spot. The application of a negative voltage causes the mirror to tilt away from a light source, thus forming a dark spot [53].

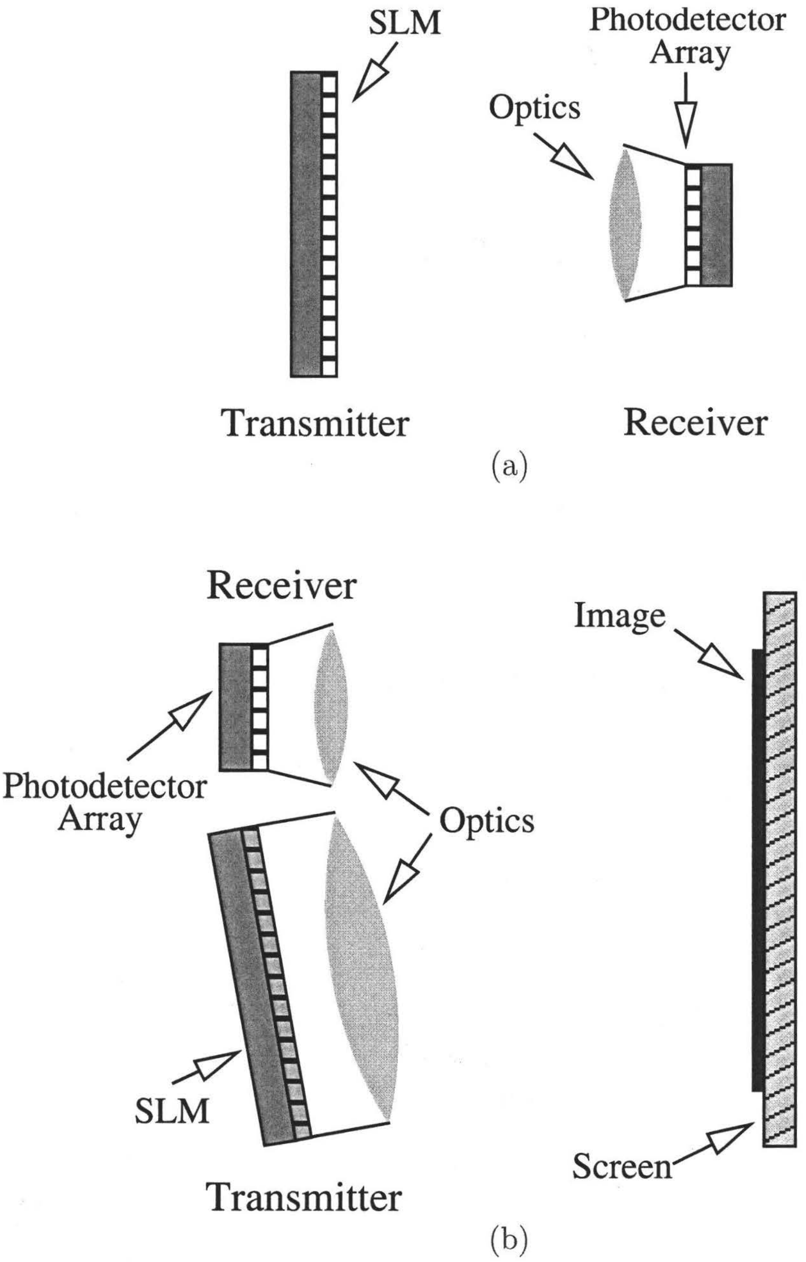

FIGURE 2.1: Different topologies for the wireless optical MIMO communication system. (a) Direct line-of-site between transmit and receive sides, (b) Direct line-of-site between the projected image and receive side.

An optical MIMO receiver consists of a 2D array of photodetectors. The photodetector array samples the spatial light intensity distribution of the projected data image, and outputs an equivalent electrical signal. A possible receiver implementation makes use of a digital camera. The imaging sensor for a standard digital camera can be implemented using a 2D array of charged coupled devices (CCD), complementary metal oxide semiconductors (CMOS), or photodiodes. For the application considered in this work, a CMOS imaging sensor is most suited for realizing a wireless optical MIMO receiver. This is due to its ability to operate at high frame rates, and its high signal to noise ratio (SNR) compared with other image sensing technologies [61, Ch. 6]. Moreover, since a CMOS imaging sensor can be easily integrated with CMOS based digital circuitry, it is possible to implement the wireless optical MIMO receiver on a single chip.

2.2.2 Channel Point Spread Function

A wireless optical MIMO channel is based on an imaging system, where imaging optics are used to project transmit data images onto the receiver's photodetector array. From scalar diffraction theory, the channel response of the imaging system can be modeled as a linear space-invariant, low-pass filter [62]. The impulse response of the channel is referred to as the point spread function (PSF), and its spatial frequency response is termed the optical transfer function (OTF). The effect of the PSF is exemplified by the blurring of received images, as illustrated in Figure 2.2 (a) and (b). Note that the images shown are not the actual transmit data image, they are merely an illustration of a concept. Figure 2.2 (c) and (d), show the spatial frequency content of the transmit and receive image respectively. Notice that the high spatial frequency content of the transmit image is attenuated at the receiver. The attenuation is caused by the low-pass characteristic of the channel OTF.

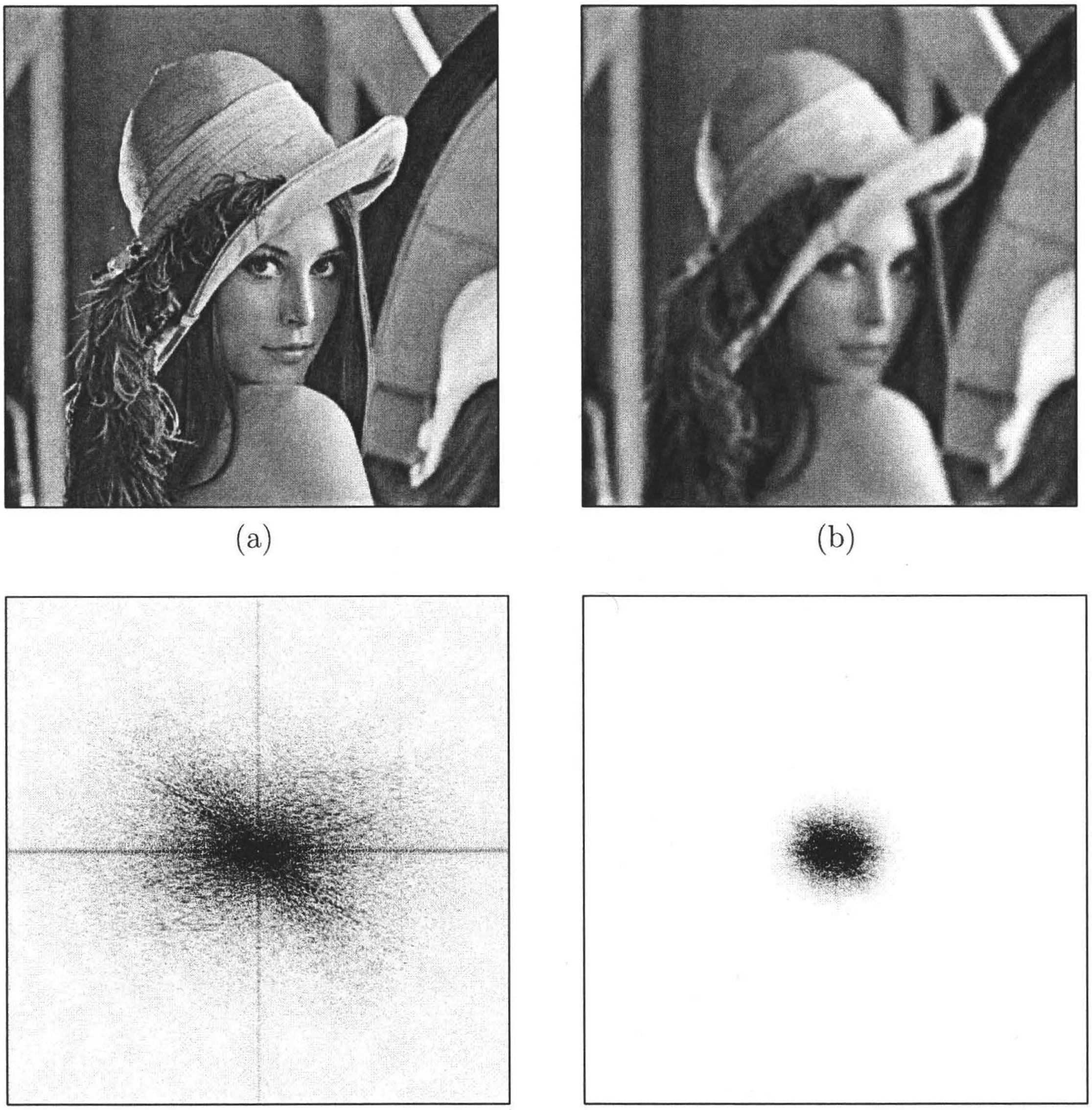

(a) (b)

(c) (d)

FIGURE 2.2: The effect of imaging optics on a transmit image. (a) Transmit image, (b) Receive image, (c) Spatial frequency spectrum of the transmit image, (d) Spatial frequency spectrum of the receive image. In the figure, the channel OTF is approximated by a 2D Gaussian shape.

Assuming that the receive image is parallel to the transmit one, the PSF is well approximated by a 2D truncated Gaussian shape [62]. Empirical measurements performed in [52] and [55] to estimate the PSF suggest that this approximation is reasonable. Figure 2.3 shows the resampled estimate of the PSF and the OTF measured

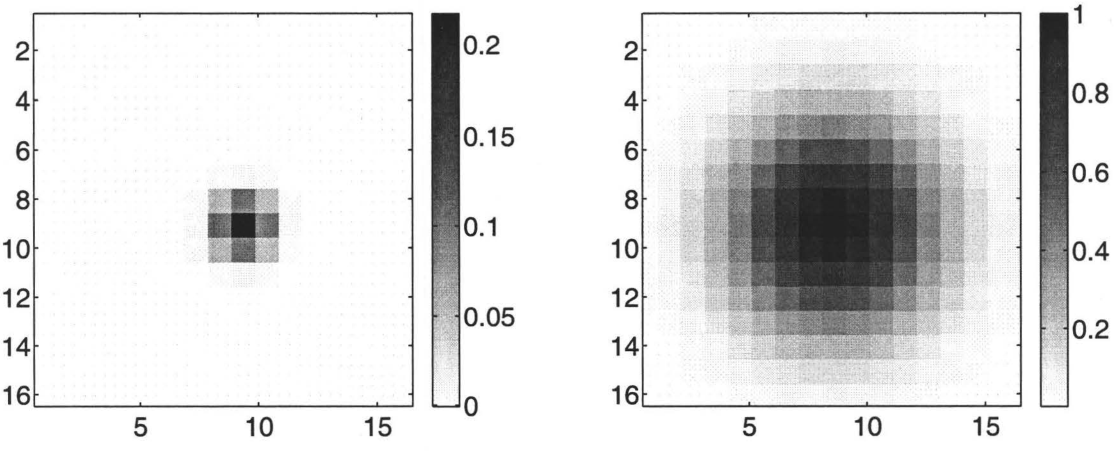

(a) (b)

FIGURE 2.3: An illustration of, (a) the sampled point spread function model, (b) the sampled optical transfer function model.

in Section 2.4.

2.2.3 Noise Characteristics

The wireless optical MIMO channel suffer from many sources of noise. The most dominant of which are thermal noise, shot noise [63], and fixed pattern noise.

Thermal noise is present in all electronic systems. It is caused by the random, and independent motion of electrons inside a resistive medium, due to thermal excitation [63]. In electronic systems, thermal noise causes voltage fluctuations which are usually modeled as being additive and Gaussian with zero mean.

Shot noise is a type of noise caused by the random arrival time of photons [63]. In an optical system, photons arrive randomly at the photodetector, thus creating fluctuations in the electrical current. For example, if transmit intensity is constant, the emitted photon rate is not uniform. A good model for this behavior is the Poisson distribution. As the intensity of the optical signal increases, the number of emitted photons is increased. Under such conditions, the distribution of shot noise is approximated as being Gaussian with a large positive mean. The positive mean reflects the non-negativity of the optical intensity signal.

Fixed pattern noise (FPN) is a 2D spatial noise resulting from device mismatches in the pixels of an imaging sensor [61, Ch. 6, Sec. 9], variations in amplifier gains, and mismatches between the analog to digital circuitry used [64]. This type of noise is most visible with low illumination conditions, as is the case for high frame rate wireless optical MIMO communication links. Due to the deterministic nature of this noise, it is possible to compensate for it at the receive side. Therefore, this type of noise is not considered in the channel model presented in Section 2.2.4.

2.2.4 Channel Model

Studying the communication aspect of the wireless optical MIMO channel requires the development of a mathematical model. This model should reflect all physical phenomena that affect communications on the link. Moreover, the model should take into account spatial misalignment, magnification and rotation. To derive a mathematical model for the channel, the following assumptions were made:

(a) Each receive pixel images multiple transmit pixels. This assumption arise as a direct result of the channel PSF, and the mismatch in pixel sizes between the transmitter and the receiver. The channel PSF and the mismatched pixel sizes causes the intensity of each transmit pixel to diffuse into its neighboring pixels at the receiver.

(b) The receive image is an orthographic projection of the transmit one, i.e. the receiver plane is parallel to the transmitter plane. For short-range wireless optical MIMO links, this assumption is reasonable since it is possible to align both sides of the link as to satisfy this condition.

(c) Thermal noise due to the receiver electronics is the dominant source of noise. This assumption is valid for wireless optical MIMO links operating at high frame rates. In a wireless optical MIMO communication system, thermal noise (*signal independent noise*) and shot noise (*signal dependent noise*) contribute to the noise at the receiver. As the number of frames transmitted per second is increased, the exposure time of each frame is reduced. The reduction in the exposure time causes less photons to arrive at each photodiode. Consequently, the power of shot noise is reduced in comparison with the power thermal noise.

Using the previously stated assumptions, the wireless optical MIMO channel can be modeled in discrete spatial domain, $[n_1, n_2]$ as follows,

$$x_R[n_1, n_2] = x_T[\mathcal{T}\{x, y\}_{\substack{x=n_1D_r \\ y=n_2D_r}}] \otimes h[\mathcal{T}\{x, y\}_{\substack{x=n_1D_r \\ y=n_2D_r}}] + \psi[n_1, n_2] \tag{2.1}$$

$$x_T[\mathcal{T}\{x, y\}_{\substack{x=n_1D_r \\ y=n_2D_r}}] \geq 0 \tag{2.2}$$

where, x_R and x_T are the received and transmitted intensity images respectively, h is the channel PSF, and ψ is the thermal noise. The transformation $\mathcal{T}\{.\}$, signifies the remapping of the coordinates caused by spatial misalignment, magnification and rotation. The spatial sampling rate (pixel spacing) at the receiver is D_r in both spatial dimensions, and $\otimes$ is the two-dimensional discrete convolution. From (2.1), the received image is equivalent to the sampled transformed transmit image, convolved with the sampled version of the transformed channel impulse response, plus thermal noise. The condition in (2.2) reflects the non-negativity constraint on the transmit signal intensity.

2.3 Spatial Discrete Multi-tone Modulation

In wireless optical MIMO systems, there are two techniques to multiplex data into transmit frames. For the first technique data are multiplexed spatially [65–67]. For the second technique data are multiplexed in spatial frequency domain [30, 68]. In a communication system, the choice of a multiplexing technique greatly affects system performance. Previous work done in this area [30, 68], showed that spatial frequency multiplexing is a robust technique to counter the effects of spatial misalignment. Therefore, this technique is the method of choice for multiplexing data into transmit frames for a wireless optical MIMO communication system.

Multiplexing data in spatial frequency requires the use of spatial discrete multi-tone modulation (SDMT). Spatial discrete multi-tone modulation is an extension of discrete multi-tone modulation (DMT) to 2D space [52]. This modulation technique is based on frequency division multiplexing, where the spatial frequency spectrum is divided into a number of discrete bins [69, Ch. 6, sec. 13][70]. Each bin is considered to be a sub-channel working in parallel with other sub-channels to transmit data across the link. In this section, the application of SDMT modulation to the wireless optical MIMO channel is discussed. A general system overview for an SDMT transmitter is presented. An expression for channel capacity is derived for a wireless optical MIMO channel employing such a modulation scheme. A detailed system design and practical implementation issues are then discussed.

2.3.1 SDMT System Overview

In SDMT systems, data to be transmitted are divided into parallel streams for each available sub-channel. The number of bits to allocate depends on the SNR in each sub-channel. Digital modulation techniques are applied to modulate data in each spatial frequency channel. In spatial domain, transmit images are generated by taking the 2D

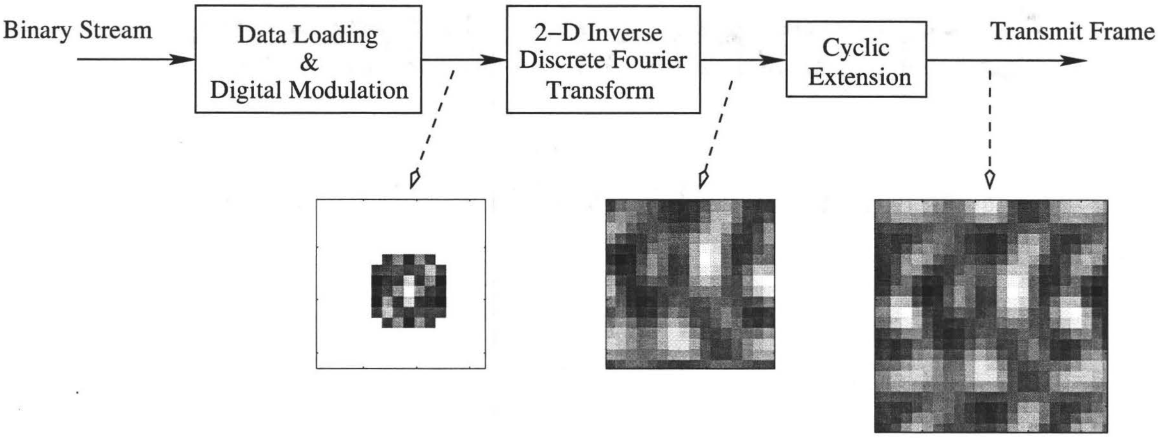

FIGURE 2.4: A block diagram of a SDMT transmitter. The generated SDMT modulated frame is of size 16×16 pixels, and the width of the added cyclic extension is 3 pixels on each side.

inverse discrete Fourier transform of the data loaded in the discrete spatial frequency. A cyclic extension is appended to each generated image before transmission as in Section 2.3.2.3. Figure 2.4 shows a block diagram of an SDMT transmitter. To recover transmit information at receive side, the cyclic extension is stripped from the receive images. The 2D discrete Fourier transform is computed. Data is recovered by demodulating the symbols in each spatial frequency bin.

2.3.2 System Design

Dividing data into parallel streams, requires knowledge about the number of bits that can be loaded in each sub-channel. This knowledge comes as a direct result of choosing a digital signaling scheme to achieve a desired probability of error. In this work, QAM modulation is chosen because of its high achievable bits per channel use [71, Ch. 4, sec. 2].

2.3.2.1 M-ary Quadrature Amplitude Modulation

Quadrature amplitude modulation is a digital modulation technique that modulates the amplitude of two orthogonal basis functions. Often, sinusoids are chosen as basis functions for easy implementation. The concept of QAM can be extended to 2D space by considering basis functions that are orthogonal in 2D space. Due to the use of SDMT modulation in this work, the following basis was chosen,

$$\Phi[n_1, n_2] = \exp\left(i2\pi\left(\frac{n_1k_1}{N_1} + \frac{n_2k_2}{N_2}\right)\right) \tag{2.3}$$

From (2.3), notice that the chosen basis constitute a 2D complex exponential term with discrete spatial frequency $[k_1, k_2]$. Moreover, the basis chosen is identical to that of the inverse discrete Fourier transform. Consequently, QAM modulation can be simply applied by using the inverse discrete Fourier transform [72]. As an example, let the loaded symbol in frequency bin $[k_1, k_2]$ be denoted by $X_T[k_1, k_2]$. Then the modulated transmit signal in spatial domain can be expressed as follows,

$$x_T[n_1, n_2] = \frac{1}{N_1N_2}\sum_{k_1=0}^{N_1-1}\sum_{k_2=0}^{N_2-1} X_T[k_1, k_2]\exp\left(i2\pi\left(\frac{n_1k_1}{N_1} + \frac{n_2k_2}{N_2}\right)\right) \tag{2.4}$$

From (2.4), notice that each complex symbol $X_T[k_1, k_2]$ modulates a 2D complex exponential basis. A 2D transmit signal $x_T[n_1, n_2]$ is generated by summing those modulated waveforms.

As with many digital modulation schemes, a QAM symbol $X_T[k_1, k_2]$ is generated by mapping a number of binary bits into a complex symbol. Typically, these symbols are denoted by points in a constellation diagram, as shown in Figure 2.5. The number of points in each constellation, and the separation distance d are chosen to satisfy a given probability of error, and an average energy constraint, or capacity.

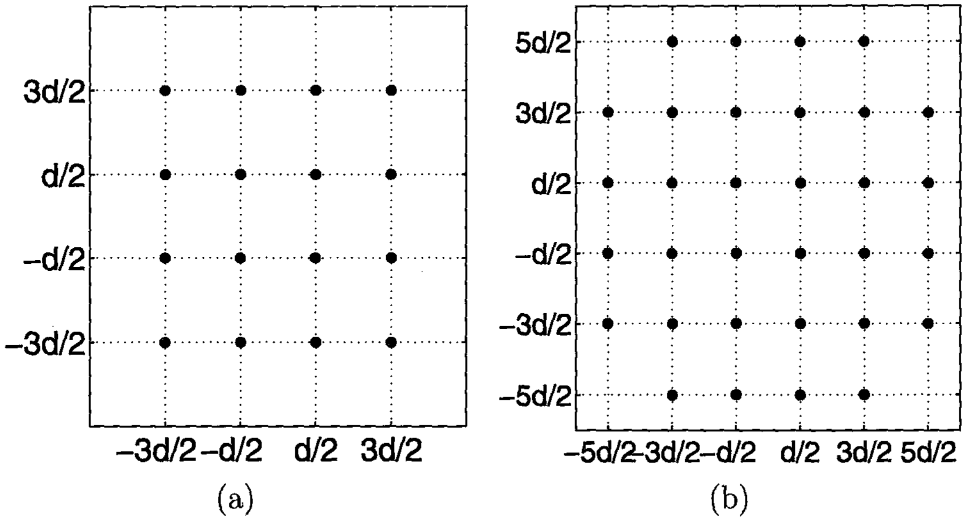

FIGURE 2.5: An illustration of, (a)16-QAM constellation, (b) 32-QAM constellation.

In SDMT modulation, each spatial frequency bin $[k_1, k_2]$ has an M-ary QAM constellation. The constellation size is determined by the signal to noise ratio (SNR) and a required probability of error. In this work, the signal in each bin must satisfy an average power constraint to maximize the channel capacity. More details on how to obtain the average power in each bin is presented in Section 2.3.3. This power constraint affects the probability of error and the size of the constellation in each bin. To choose a QAM constellation for each spatial frequency bin, the SNR in each bin is used to compute the probability of error for different constellation sizes. The constellation size with a probability of error equal or less than the desired value is chosen.

Since the SNR is different in each spatial frequency bin, a different constellation size is chosen for each bin. Figure 2.6 shows the size of the QAM constellations used for continuous-tone SDMT modulation. For the figure, the channel OTF is assumed to be a 2D Gaussian shaped with variance of $\sigma_H^2 = 3.4$ in each dimension, and the channel noise power in each frequency bin is 10. The QAM constellations where chosen to satisfy an average power constraint, and a probability of error $\leq 10^{-4}$ in

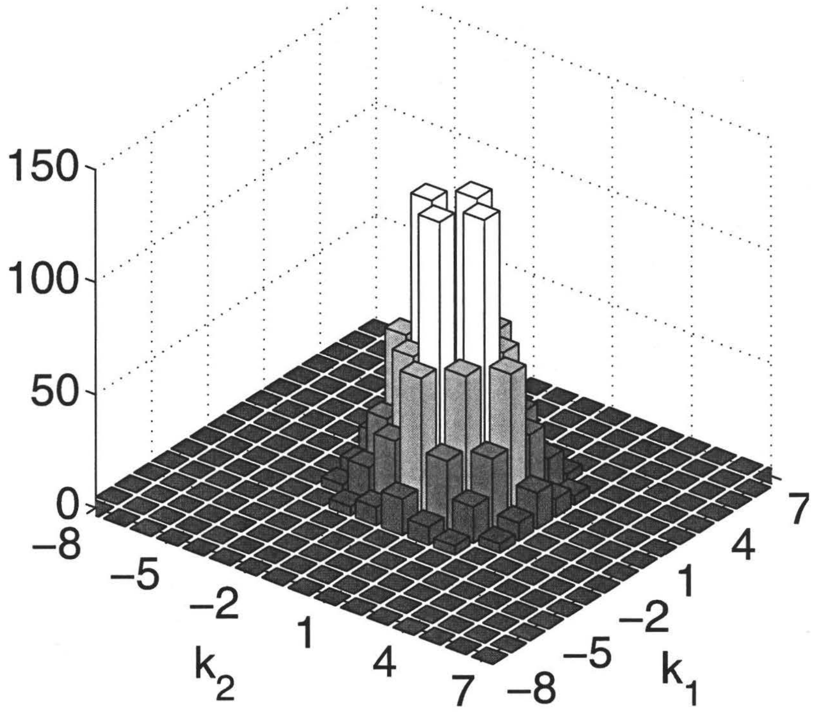

FIGURE 2.6: The size of a QAM constellation changes for each spatial frequency bin to achieve a probability of error of 10^{-4} and an average electrical power per channel given by water pouring 2.3.3.

each spatial frequency bin. The average power constraint is given by water pouring as in 2.3.3.

2.3.2.2 Data Loading and Transmit Frame Generation

In the wireless optical MIMO channel considered, information is conveyed by modulating the intensity of a light-source. As a result, transmit frames must be real and non-negative. Since the 2D discrete inverse Fourier transform is used to generate transmit frames from the loaded data in spatial frequency, Hermitian symmetry must be satisfied to ensure transmit frames are real. Mathematically, Hermitian symmetry is expressed by,

$$X_T[N_1 - k_1, N_2 - k_2] = X_T^*[k_1, k_2] \tag{2.5}$$

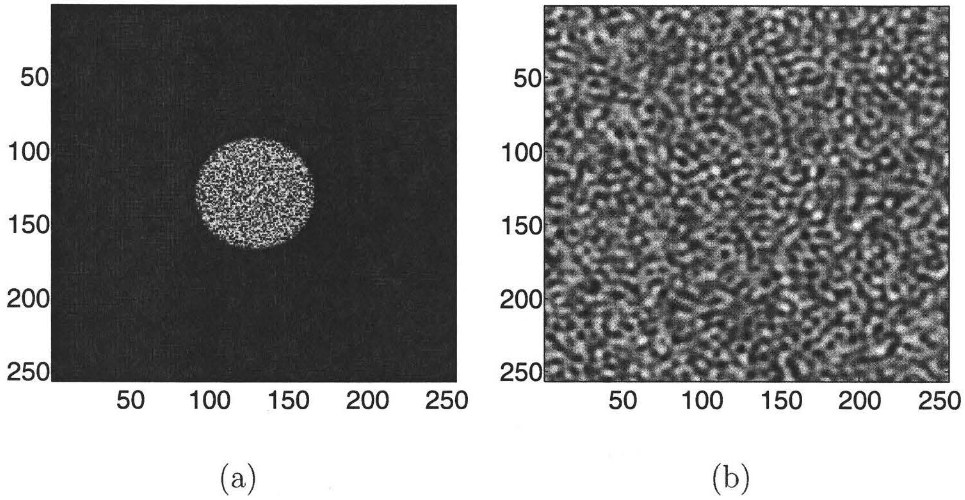

(a) (b)

FIGURE 2.7: An illustration of, (a) The data loaded into 2D complex spatial frequency bins, (b) The transmit frame is generated by taking the 2D inverse Fourier transform of loaded data.

where X_T is the data frame, $[k_1, k_2]$ are the discrete spatial frequency coordinates, N_1 and N_2 are the number of frequency bins in each frequency dimension. Notice that by imposing Hermitian symmetry, the capacity per frame is halved. Figure 2.7 shows the loaded data in spatial frequency domain, and the corresponding generated transmit image. Data is loaded in each bin by mapping the binary data word into constellation symbol.

2.3.2.3 Cyclic extension

Due to the discrete and finite nature of transmit and receive elements, the discrete Fourier transform (DFT) and its inverse (IDFT) are used to realize SDMT modulation in practice. The use of the DFT imposes conditions on transmit signal in space and spatial frequency. The first condition requires the signal to be discrete in space and in spatial frequency. The second condition imposes periodicity on the signal in space, and its spectrum in spatial frequency. In general, if a system satisfies the periodicity condition, it can be described as follows,

$$R[k_1, k_2] = X[k_1, k_2]H[k_1, k_2] + \Psi[k_1, k_2] \tag{2.6}$$

where R is the receive frame, X is the transmit frame, H is the channel OTF and Ψ is the noise in spatial frequency domain. From (2.6), the receive frames can be equalized by a multiplication with a complex constant. From a practical perspective, the first condition is always satisfied due to the discrete nature of devices used. But, the second condition is not satisfied due to the finite size of such devices. By violating the periodicity condition, inter-channel interference arise between the discrete spatial frequency channels. Thereby increasing the complexity of equalization algorithms at the receive side.

To overcome channel crosstalk, a cyclic extension is appended around the transmit images [30, 68]. The purpose of the cyclic extension is to make transmit images appear periodic to the channel [73]. Thereby, satisfying the periodicity condition. As a result, receive frames can be expressed by (2.6). Thus, reducing the complexity of equalization to a multiplication by a constant.

Due to the finite width of the channel PSF, it is sufficient to add a cyclic extension of width equal to half the width of the PSF. Appending a cyclic extension to a transmit image encapsulates the image in a frame. This frame is formed by periodically extending the signal in 2D space. Figure 2.8 shows a cyclic extension applied to an image. Note that the red line was added to indicate the boundary of the cyclic extension to the reader, this line would not appear in actual transmitted frames.

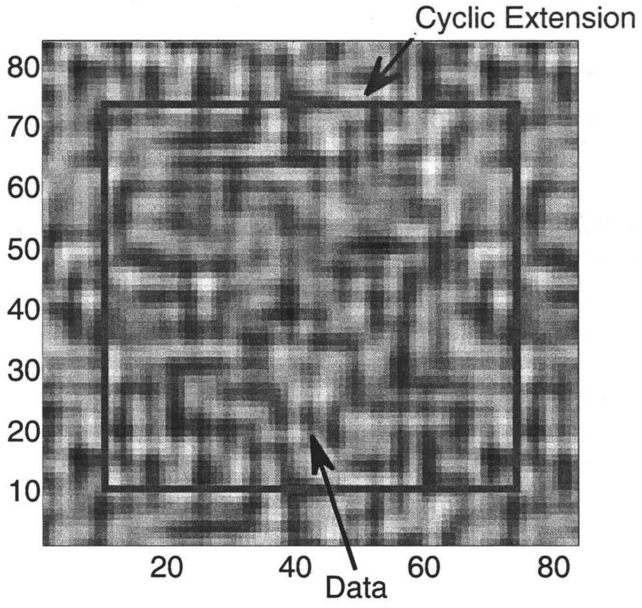

FIGURE 2.8: Transmitted image generated by appending a cyclic extension to the IDFT of the SDMT frame.

2.3.3 Channel Capacity

In general, evaluating the channel capacity for a wireless optical MIMO channel is not an easy task. In this work, assumptions were made to formulate a closed form expression for the channel capacity. For the first assumption, the number of transmit and receive elements are the same. Note that this condition is not a necessary one, it is only used to simplify the derivation of the channel capacity. For the second assumption, it is assumed that the channel is transformation free, i.e. magnification is unity, and rotation is zero. This assumption is valid since spatial transforms remap data in space, consequently, the information is preserved. For the third assumption, it is assumed that the channel noise is dominated by thermal noise, which is modeled as being additive and Gaussian as in Section 2.2.3. Noise in optical MIMO systems consist of thermal noise and shot noise. As the frame rate is increased, the exposure time is decreased, resulting in the power of shot noise to decreased. The reduction in shot noise power is due to low number of photons arriving at the imaging sensor during the shorter exposure time. Therefore, one can say that as the frame rate is increase, thermal noise dominates shot noise.

Using these assumptions, equation (2.1) can be rewritten to express the received frames in spatial frequency domain $[k_1, k_2]$ as follows,

$$X_R[k_1, k_2] = X_T[k_1, k_2]H[k_1, k_2] + \Psi[k_1, k_2]; \tag{2.7}$$

where X_R is the DFT of the receive frame x_R, X_T is the DFT of the transmit frame x_T, H is the channel OTF, and Ψ is the DFT of receivers thermal noise. At receive side, receive frames are equalized by a multiplication with the channel inverse to get,

$$\frac{X_R[k_1, k_2]}{H[k_1, k_2]} = X_T[k_1, k_2] + \tilde{\Psi}[k_1, k_2] \tag{2.8}$$

where, $\tilde{\Psi}$ is equal to

$$\tilde{\Psi}[k_1, k_2] = \frac{\Psi[k_1, k_2]}{H[k_1, k_2]} \tag{2.9}$$

From (2.7), notice that the SDMT system in spatial frequency domain can be seen as a collection of parallel Gaussian channels. Therefore, the channel capacity can be estimated by [31],

$$C \approx \frac{1}{2} \sum_{k_1=0}^{N_1-1} \sum_{k_2=0}^{N_2-1} \log \left(1 + \frac{\Phi_x[k_1, k_2]}{\Phi_{\tilde{\psi}}[k_1, k_2]} \right) \tag{2.10}$$

where C is the aggregate channel capacity, N_1 and N_2 correspond to the number of spatial frequency bins in each spatial dimension, $\Phi_x[k_1, k_2]$ and $\Phi_{\tilde{\psi}}[k_1, k_2]$ are the allocated power and the noise power in spatial frequency bin $[k_1, k_2]$ respectively. Note that the capacity in (2.10) is merely an estimate due to the non-negative amplitude constraint imposed on the transmit intensity signal.

To derive the channel capacity, it was assumed that the channel is composed of a number of parallel Gaussian channels. This assumption implies that the intensity distribution of the generated SDMT transmit frame, is approximated by a Gaussian with variance equal to the average electrical power [74, Ch. 3, sec. 3]. Due to the Gaussian distribution of the transmit frame intensity, the intensity can have positive and negative values, thus, violating the non-negativity constraint imposed by the optical intensity channel. To satisfy the non-negativity with high probability, a constant bias is added to the image such that the probability of negative intensity is very low. Due to this method, the capacity in (2.10) is an estimate of the actual constrained channel capacity. For more details, refer to Chapter 3.

Now that an expression for the capacity is estimated, it is important to find the power allocation, Φ_x, that maximizes this expression. From optimization theory, the optimum power allocation that maximizes channel capacity is found by applying the *Water Pouring* algorithm [75]. In one dimensional case, the water pouring algorithm can be expressed mathematically as follows [2, Ch. 5, sec. 5],

$$\sum_{n=0}^{N-1} \max\{0, 1/\nu^* - \alpha_n\} = \sigma_x^2 N \tag{2.11}$$

where σ_x^2 is the average electrical power per bin, N is the total number of available bin. The equation above states that the sum of power allocated in all bins, is equals to the total power available. Figure 2.9 represents an illustration of the water filling algorithm in (2.11). From Figure 2.9, notice that more power is allocated to the channels with low noise power, while, less power is allocated to channels with high noise power. Notice also that for some channels no power was allocated due to the high noise power. The concept of water pouring can be extended to 2D case. Figure 2.10 shows power allocated by the water pouring algorithm for a 2D wireless optical MIMO channel. Notice that no power was Allocated to DC, since no information is transmitted in that bin. Any information transmitted in DC bin will introduce bias to the generated SDMT frame. The added bias will result in the violation of the amplitude constraints. Notice also that no power was allocated to the high frequency spectrum. This is due to the presence of high effective noise power $\Phi_{\tilde{\psi}}$[31].

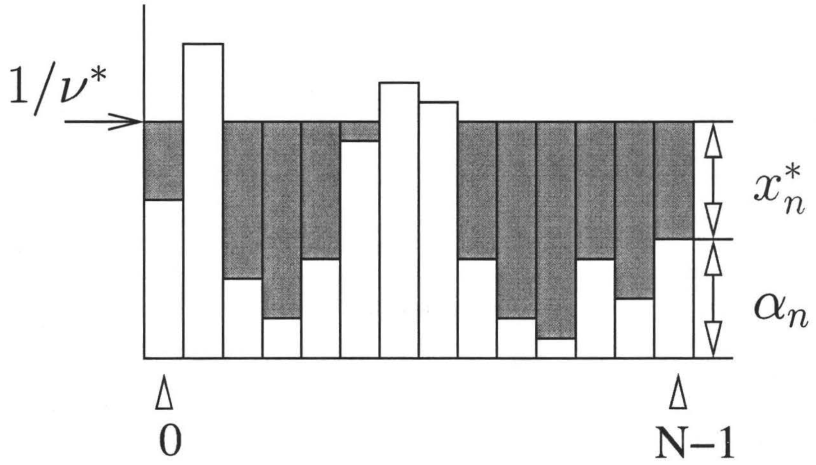

FIGURE 2.9: An illustration of water pouring algorithm over a channel with N discrete spatial frequency bins. The dark shaded region represents the optical power allocation in each frequency bin. The white shaded region represents the noise power in each frequency bin [2, Ch. 5, sec. 5].

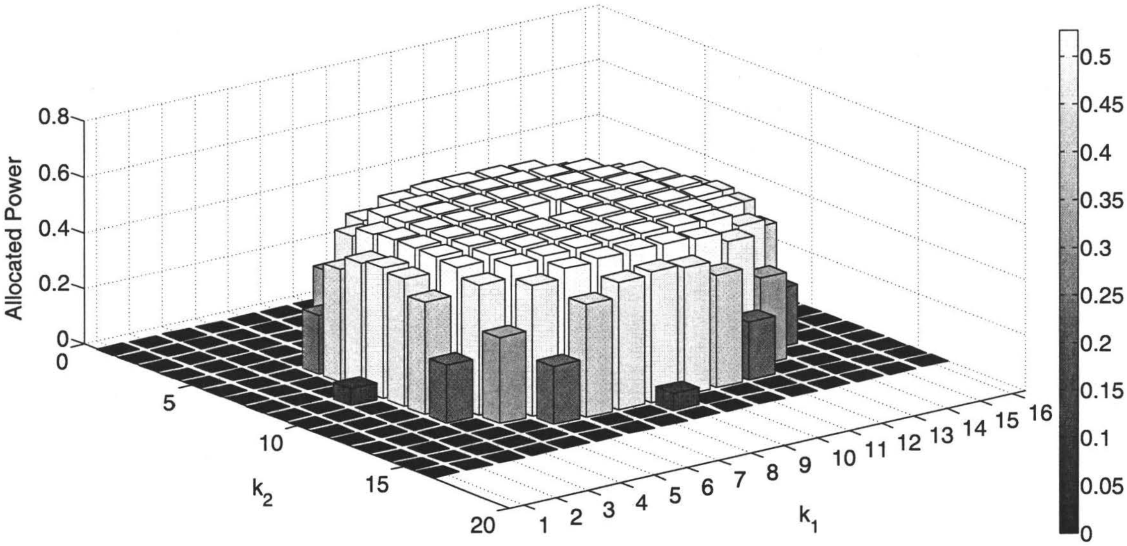

FIGURE 2.10: An illustration of the power allocated in 2D spatial frequency.

2.3.4 Implementation issues

In SDMT, frames in space are computed by applying the inverse Fourier transform on data frames. Resulting transmit frames are continuous gray-scale images, i.e. the amplitude of each pixel can have any real value. Current digital transmit devices can only output discrete amplitude intensity levels. Thus, rendering SDMT systems complex for practical implementation. Moreover, since the distribution of amplitudes of the SDMT signal is approximated by Gaussian noise [74, Ch. 3, sec. 3], a large bias must be added to the image to satisfy the non-negativity condition with high probability. To solve these issues, multilevel halftoning is introduces in Chapter 3.

2.4 Channel Measurements

To get a realistic channel parameters for the simulation, a prototype wireless optical MIMO communication link was built. For the link, the transmitter is based on a commercial DLP projector [76, LT30] which projects its image onto a flat wall. The circuitry of the projector is replaced with a controller board for the DLP which allows freedom to transmit any sequence of stored images [53]. This configuration allows for frame rates of up to 10 kfps and a maximum resolution of 1024 × 768 pixels. The illumination source of the projector has been replaced with a metal halide machine vision illuminator. The illuminator was coupled to the projector optics using a 1/2" fiber optic light guide as shown in Figure 2.11.

The receiver is a high speed mega-pixel CMOS digital camera [77, MC1310] which captures the image projected on the wall. The camera is connected to a frame grabber [78, Odyssey XCL] using the full camera Link configuration which is capable of transferring data at a maximum rate of 660 Mbytes/sec. Digital recording

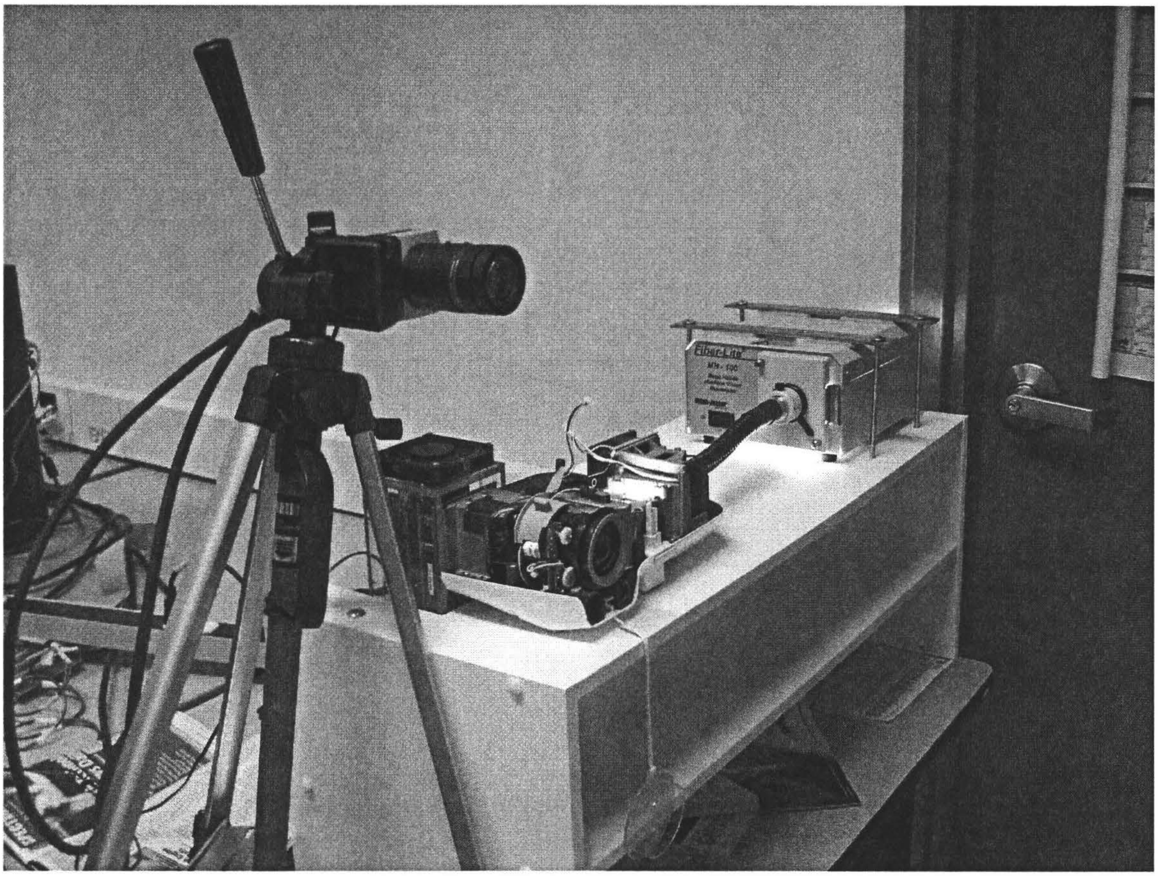

FIGURE 2.11: A wireless optical MIMO link prototype setup.

software [79, Streampix] is used to capture and store the received frames. Temporal synchronization is achieved by using a signal generator card [80, NI6601] that generates trigger pulses that drive both the transmitter and the receiver. When a trigger pulse is received by the projector, an image is projected onto the wall. After few micro-seconds delay, the camera starts integrating the spatial intensity image. The integration time of the camera is controlled by a programmable shutter, with exposure time less than the illumination period of the frame.

The separation distance between the camera, and the projected image is set to 1.1 m. The camera was positioned to ensure that its optical axis aligns with that of the image in order to minimize the projective distortion. The focal length of the projector was adjusted to get unity magnification (i.e. image size in pixels is the

		N				
		64	128	256	512	750
Frames per second	200	9.9439	10.081	9.8231	9.7359	11.45
	400	39.437	39.655	37.465	32.177	36.384
	601	82.152	80.613	78.801	71.788	74.78
	801	67.507	67.55	71.942	100.64	115.54
	1001	129.83	130.23	136.42	144.72	162.29
	1204	149.85	151.06	157.28	181.51	219.39
	3039	4372.9	1879.7	1250.2	1133.8	1209.4
	5025	6993.5	3343.7	2452.1	2407.4	3009.2
	7142	3920.5	3659.1	3590.9	4056.4	5421.8
	10638	9961.2	8837.7	8173.1	9315.8	12938

TABLE 2.1: A table showing the measured noise variance σ_{ψ}^2 in spatial domain, for different frame sizes, $N \times N$, and frame rates.

same at both transmitter and the receiver). To mitigate hardware limitations and generate consistent measurements , the operating frame rate was fixed to 100fps, and the programmable shutter is used to adjust the exposure time such that the effective frame rate is given by the inverse of the exposure time. As the exposure time changes, the sensor gain is manually adjusted such that the histogram of the received image occupies the full dynamic range (0 to 255) of the sensor.

Channel noise measurements were performed by transmitting and receiving sequences of dark and illuminated frames. The channel noise consists of fixed pattern noise, due to variations over the sensor array, and signal independent noise. For each frame rate, the fixed pattern noise is estimated by sending 1000 dark frames and averaging over the received frames. The signal independent noise is estimated by averaging over 1000 dark frames and 1000 illuminated frames. By assuming that the noises of neighboring pixels are independent, the complex noise in discrete frequency domain is white. The measured noise variance in discrete frequency is given in Table 2.1.

In previous work [52], the channel response was measured by transmitting a sequence of pulses in spatial domain. At the receiver, the channel impulse response was measured and averaged over many instances. The channel spatial frequency response is computed by taking the 2D Fourier transform of the averaged impulse response. Although this approach is theoretically feasible, it is difficult to implement in practice. The difficulty arises due to spatial misalignment and background illumination. Slight misalignment causes transmit pulse energy to dissipate over many pixels. Combining that with background illumination renders transmit pulses undetectable at receiver.

In this work, a new technique is used for measuring the spatial frequency response. For this technique, a pseudorandom number generator with a predefined seed value was used to generate a sequence of 1000 binary frames at both ends of the link. The use of the same seed value resulted in the generated sequence being identical at both ends of the link. The frames are then transmitted across the channel. Using the model in (2.1), the receive frames can be expressed as,

$$X_R[k_1, k_2] = X_T[k_1, k_2] H[k_1, k_2] + \Psi[k_1, k_2]; \tag{2.12}$$

By dividing the spatial frequency spectrum of the receive frame by the corresponding transmitted one, the following equation is obtained,

$$\frac{X_R[k_1, k_2]}{X_T[k_1, k_2]} = H[k_1, k_2] + \frac{\Psi[k_1, k_2]}{X_T[k_1, k_2]} \tag{2.13}$$

Since the channel thermal noise has zero mean Section 2.2.3, and the channel is assumed to be time invariant, the OTF can be approximated by averaging over many frames,

$$\frac{1}{Z} \sum_{z=0}^{Z-1} \frac{X_R[k_1, k_2]}{X_T[k_1, k_2]} \approx H[k_1, k_2] \tag{2.14}$$

where, Z is the number of frames. Notice that the approximation in (2.14) is replaced with equality in the expected value. For a practical system, the number of frames, and the noise variance σ_Ψ^2 will affect the accuracy of the results. For systems with low noise variance, a good OTF approximation can be obtained with a small number of frames. For example, if the noise variance is zero, then the noise is deterministic, therefore, only one frame is needed to compute the OTF. As the noise variance is increased, more frames are needed to obtain a good approximation.

Since the PSF of the channel is modeled to have a Gaussian shape, the corresponding OTF is real and Gaussian. Figure 2.12 shows the measured OTF for a frame size of 128 × 128 pixels. From Figure 2.12 (a), notice that the measured OTF is well approximated by a 2D Gaussian shape. From Figure 2.12 (b), notice that the measured OTF has a non-zero linear phase shift. The phase shift is caused by spatial misalignment between the transmitter and receiver. For more details on spatial misalignment refer to Chapter 4.

2.5 Training Session Overview

In the previous section, methods to measure the channel optical transfer function, spatial frequency noise, and fixed pattern noise were discussed. In this work, it is assumed that the transmitter and the receiver have some knowledge of the channel. To achieve this in practice, a low bit-rate feedback channel must exist between both sides of the link. Figure 2.13 shows an overview of the required channel measurements for both sides of the link. For the transmitter side, information about the spatial frequency noise and the channel OTF are required. Due to the whiteness of the spatial frequency noise as shown Section 2.4, only the average value of the noise power need to be transmitted across the feedback link. As for the OTF, information about its absolute value are needed at the transmitter. In the previous section, it was shown that the OTF is well approximated by a two-dimensional Gaussian shape. Therefore, to minimize the amount of information sent across the feedback channel, it is only required to transmit information about the variance of the 2D Gaussian shape.

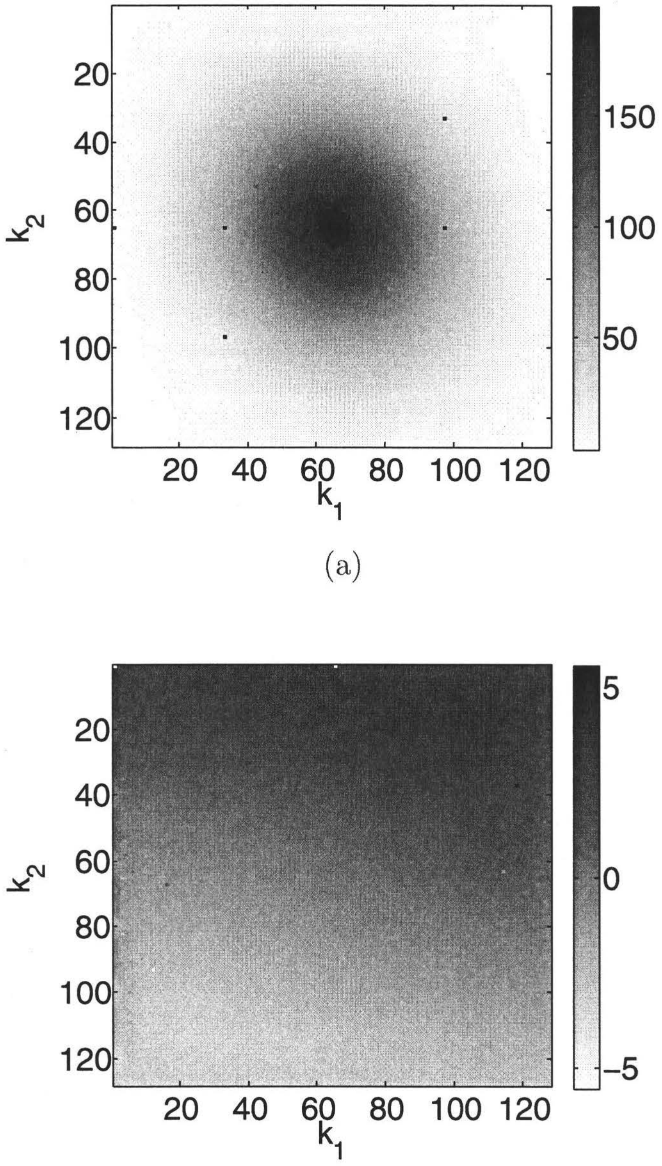

(a)

(b)

FIGURE 2.12: Measured OTF in a prototype wireless optical MIMO system, (a) Absolute value of the measured OTF, (b) Phase of the measured OTF (degrees).

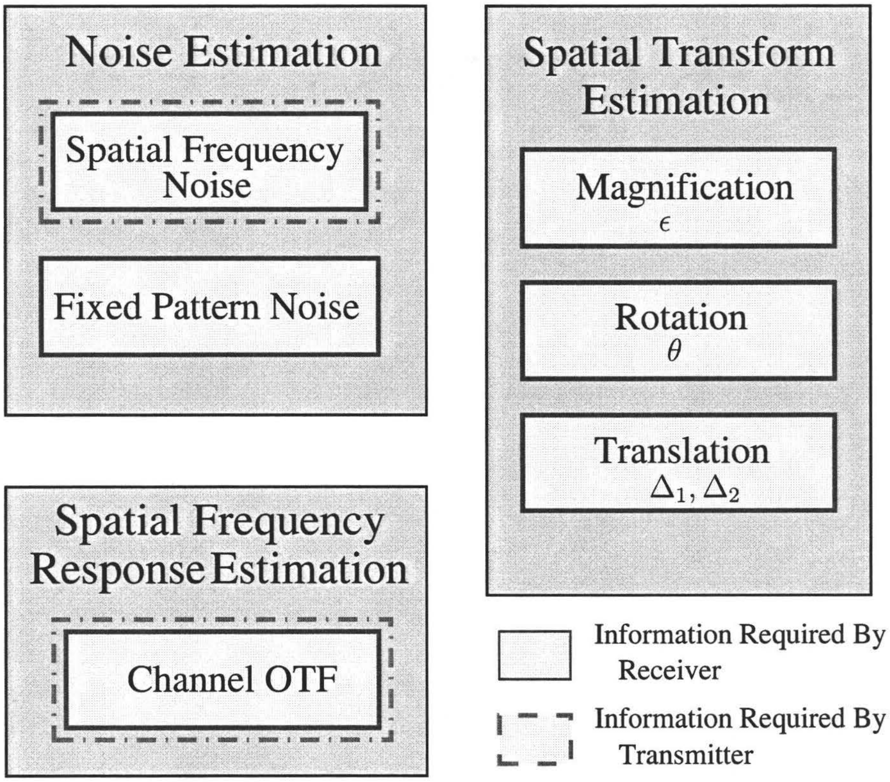

FIGURE 2.13: A block diagram representing the measurements required by the transmitter and the receiver.

From Figure 2.13, the measured optical transfer function, fixed pattern noise, spatial frequency noise, and spatial transforms are needed at the receiver side. These measurements are used to equalize and detect the received data.

2.6 Conclusion

In this Chapter, the wireless optical MIMO channel was studied and measured. Two topologies that achieve line-of-sight between the transmit image and the receiver where studied. The channel was modeled as a spatially invariant low-pass filter characterized by a point spread function. A channel model encompassing the effects of spatial transforms on transmit SDMT frames was derived. An overview of spatial discrete multi-tone modulation is presented. The channel capacity is estimated for a wireless optical MIMO channel using SDMT modulation. A prototype wireless optical MIMO communication system is presented. The prototype system is used to measure the channel parameters. The measured channel parameters are used in the simulations done in Chapter 3 and Chapter 4.

Chapter 3

Multilevel Error Diffusion and Noise Shaping

3.1 Introduction

In Chapter 2, the theory behind SDMT modulation was introduced. Although this technique mitigates the effects of spatial misalignment and simplifies the equalization process at the receiver, its practical implementation has proven challenging. The difficulty in implementation is due to the infinite amplitude resolution of transmit images, and to the non-negativity constraint. To simplify the implementation of such systems, binary halftoned SDMT was introduced [31]. In binary halftoned SDMT, digital halftoning techniques are used to quantize the amplitudes of the continuous-tone image into a binary set. Moreover, the non-negativity constraint on transmit images is easily met by adding a constant bias. The reduction in complexity brought by binary halftoning comes at the cost of adding quantization noise. Consequently, the achieved channel capacity decreases.

This chapter presents two techniques to reduce the effect of quantization noise on the channel capacity. The first method is *multilevel halftoning*, and the second method is *higher order noise shaping.* An overview of digital halftoning is given, and a model for the channel capacity of the multilevel halftoned SDMT system is derived. The application of multilevel halftoning to the wireless optical MIMO channel is discussed, and a linear model is derived. Simulation results for the channel capacity of the multilevel SDMT system are presented. The implementation of multilevel halftoning in wireless optical MIMO channels is discussed. The effect of first and second order noise shaping on the channel capacity are studied. Optimization techniques are applied to maximize the channel capacity with respect to first and second order noise shaping filters.

3.2 Background

3.2.1 Digital Halftoning

Digital halftoning is a process commonly used in image processing, its purpose is to transform a continuous-tone image into a discrete one. In digital halftoning, a discrete image with limited amplitude resolution is generated, the discrete image is perceptually similar to the continuous one [81]. There exist many halftoning algorithms. The most commonly used halftoning algorithm is *error diffusion halftoning* [82]. Error diffusion halftoning is a generalization of $\Delta\Sigma$ modulation to 2D space [82, 83], and it works by diffusing the residual quantization noise from each pixel, and distributing it among the neighboring un-quantized pixels. A block diagram of the error diffusion halftoning system is shown in Figure 3.1. From the figure, the amplitude of each pixel in the continuous-tone image, $x[n_1, n_2]$, is quantized into a discrete

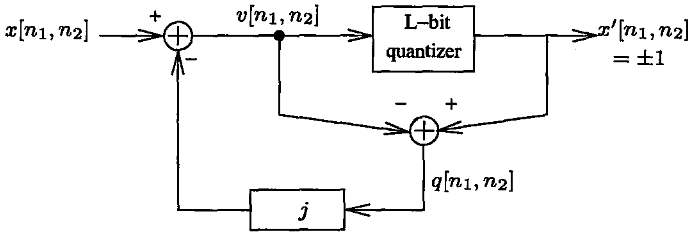

FIGURE 3.1: A block diagram of an error diffusion filter. The input signal x is quantized using an L-level quantizer, the resulting quantization error q is distributed among neighboring pixels according to the filter j.

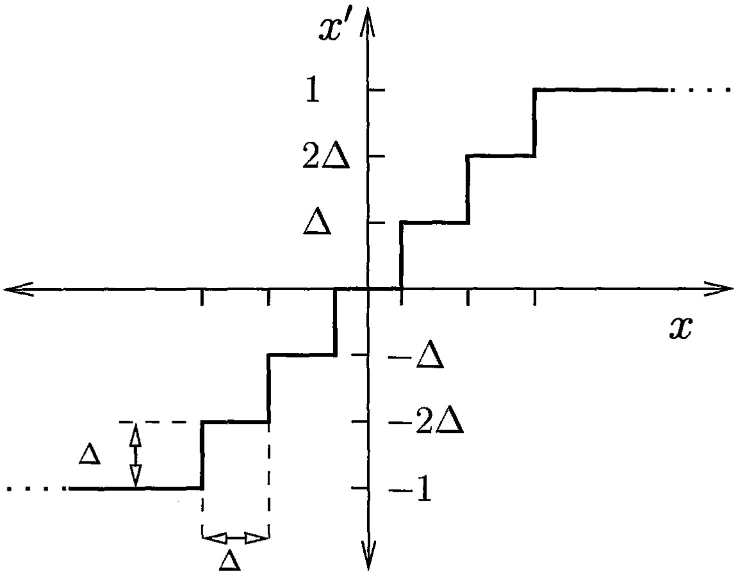

FIGURE 3.2: An illustration of a 7-level quantizer. The range of amplitudes of the input signal, x, is divided into intervals of width Δ. Each interval is mapped into a discrete output level signal, x'. If the input signal is out of range, the quantizer output saturates to ± 1.

amplitude level signal, $x'[n_1, n_2]$. The quantization process is performed using an L-level quantizer. Figure 3.2 shows the mapping for a 7-level quantizer. Notice that the continuous range of amplitudes of the input signal, $x[n_1, n_2]$, is divided into intervals of equal width. The output signal, $x'[n_1, n_2]$, is generated by mapping each interval to a discrete level output. The difference between the quantizer input and output is referred to as quantization error. From Figure 3.1, notice that the resulting quantization error, $q[n_1, n_2]$, is distributed among neighboring pixels according to an error

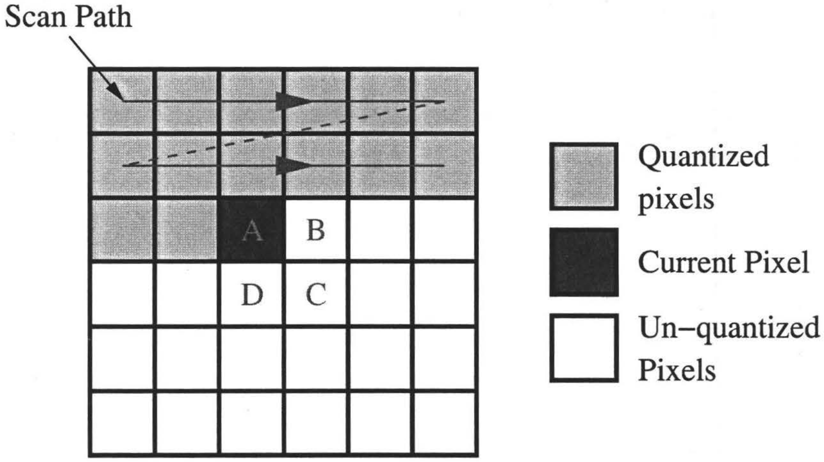

FIGURE 3.3: Raster scan is used to halftone images. Quantization noise from current pixel (A) is distributed among the neighboring pixels (B), (C) and (D) according to an error diffusion filter j. Since the quantization noise is only distributed among un-quantized pixels, the systems is termed causal with respect to the scan direction.

diffusion filter j. This process is repeated in a raster scan fashion from the top left to the bottom right corners of the image as in Figure 3.3. In this work, the number of quantization levels identifies the number of halftoning levels. For example, if a system has a 2-level quantizer, the output image is referred to as a binary-halftoned image. For systems with L-level quantization levels, where $L > 2$, the output is termed a *multilevel halftoned* image.

To give an intuition behind the design of the error diffusion filter j, the error diffusion system shown in Figure 3.1 can be expressed in discrete frequency domain as follows,

$$X'[k_1, k_2] = X[k_1, k_2] + Q[k_1, k_2] \underbrace{(1 - J[k_1, k_2])}_{\text{High pass}} \tag{3.1}$$

where X, X', Q and J are the discrete Fourier transforms of the input signal x, the output signal x', the quantization noise q and the error diffusion filter j respectively. From the equation, notice that the spatial frequency response of the quantized image is equivalent to the frequency response of the continuous image, plus some shaped quantization noise. From Section 2.3.1, it is known that the input signal is a low-pass signal. Consequently, the noise shaping term, $(1 - J[k_1, k_2])$, must have a high-pass characteristic to push the quantization noise away from the spectrum of the input data. For this to be true, the spatial frequency response of the error diffusion filter, $J[k_1, k_2]$, must have a low-pass spatial frequency response. In this system, adding more degrees of freedom to the error diffusion filter, j, can help change the characteristics of its low-pass spatial frequency response. In this work, the addition of more degrees of freedom is referred to as higher order noise shaping.

3.2.1.1 Error Diffusion Halftoning: An Example

In this section, a short example is given to illustrate the workings of error diffusion halftoning. In this example, the continuous-tone image is represented as a matrix in Figure 3.4(a). For this example, binary-level error diffusion is used, i.e. the continuous-tone image is halftoned in to a binary-level frame with output levels +1 or -1. The error diffusion filter used in this example is given as follows,

$$j = \begin{bmatrix} 0 & 0.9 \\ 0.9 & -0.8 \end{bmatrix}$$

To halftone the continuous-tone image in Figure 3.4(a), the first pixel (1A) is quantized and the resulting quantization error is then distributed or *diffused* to the neighboring pixels shown in gray. Hence the name, error diffusion halftoning. Since the value of the pixel (1A) is -0.5, the pixel is quantized to -1. This quantization process results in quantization error equal to difference between the output level and the input level as shown in Figure 3.1. In this example, the quantization error resulting from quantizing the pixel (1A) is equal to -0.5. From Figure 3.1, notice that the

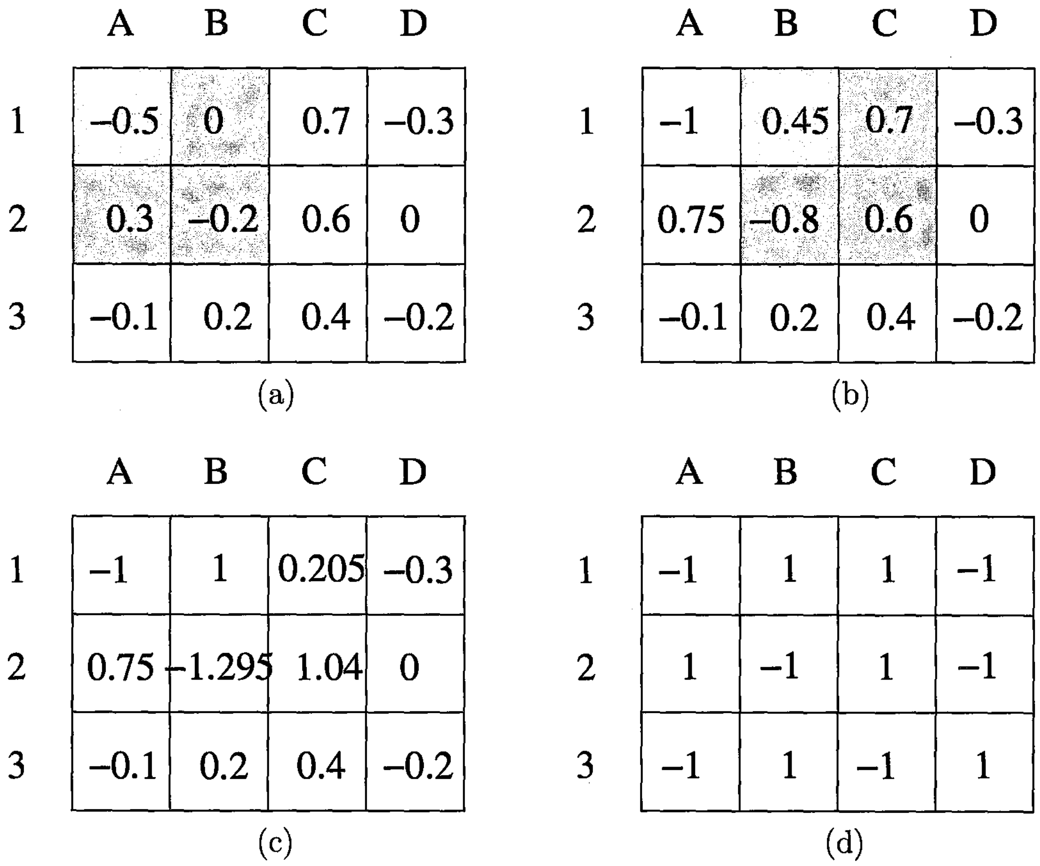

	A	B	C	D
1	−0.5	0	0.7	−0.3
2	0.3	−0.2	0.6	0
3	−0.1	0.2	0.4	−0.2

(a)

	A	B	C	D
1	−1	0.45	0.7	−0.3
2	0.75	−0.8	0.6	0
3	−0.1	0.2	0.4	−0.2

(b)

	A	B	C	D
1	−1	1	0.205	−0.3
2	0.75	−1.295	1.04	0
3	−0.1	0.2	0.4	−0.2

(c)

	A	B	C	D
1	−1	1	1	−1
2	1	−1	1	−1
3	−1	1	−1	1

(d)

FIGURE 3.4: This figure illustrates the progression of error diffusion halftoning with (a) the continuous-tone image, (b) the image after pixel 1A is quantized, (c) the image after pixel 1B is quantized and (d) the final output of the error diffusion system.

quantization error is multiplied by the error diffusion filter j as shown below,

$$q * j = -0.5 * \begin{bmatrix} 0 & 0.9 \\ 0.9 & -0.8 \end{bmatrix} = \begin{bmatrix} 0 & -0.45 \\ -0.45 & 0.4 \end{bmatrix} \tag{3.2}$$

After multiplying the quantization error by the error diffusion filter, the result is subtracted from the neighboring pixels as shown below,

$$\begin{bmatrix} 1A & 1B \\ 2A & 2B \end{bmatrix} - \begin{bmatrix} 0 & -0.45 \\ -0.45 & 0.4 \end{bmatrix} = \begin{bmatrix} -1 & 0.45 \\ 0.75 & -0.8 \end{bmatrix} \tag{3.3}$$

Using this technique, the resulting image after quantizing the first pixel (1A) is shown Figure 3.4(b). To quantize pixel (1B), a similar process is carried out on the image shown in Figure 3.4(b). Since the intensity of the pixel (1B) is 0.45, the output intensity level is +1, and the quantization error is equal to 0.55. The resulting quantization error is multiplied by the error diffusion filter and the result is subtracted from the neighboring pixels shown in gray, mainly, (1B) (1C) (2B) and (2C). The resulting image after quantizing the intensity of pixel (2B) is shown in Figure 3.4(c). Figure 3.4(d) shows the final halftoned image after quantizing the intensities of all the pixels in the image.

3.2.1.2 Linearity and Stability of the Error Diffusion Filter

The error diffusion system in Figure 3.1 is highly non-linear. Non-linearity is caused by quantizing the signal into discrete levels. The analysis of such a non-linear system is difficult. Therefore, a linear model is needed to simplify the analysis. To linearize the quantizer, it is common to assume that the quantizer error q is white and signal independent with variance σ_q^2 [84–86]. To satisfy these assumptions, the power of the quantizer input σ_v^2 must be bounded. To bound σ_v^2, the electrical power of the of the SDMT signal, σ_x^2, must also be bounded. If σ_x^2 is too large, the quantizer will saturate to either, +1 when the input signal v is greater that $1+\Delta$, or -1 if v is less than $-1-\Delta$. When the quantizer output signal saturates, the quantization error will follow the sign of the input signal. Consequently, the independence assumption is no longer valid.

Moreover, the signal saturation could cause instability in the system due to the large quantization noise power fed back to the input. Although the stability of the error diffusion system has been studied religiously in previous literature [87–89], these criteria cannot be applied directly due to the Gaussian distributed nature of the input signal. To study the stability of the error diffusion system for a Gaussian distributed

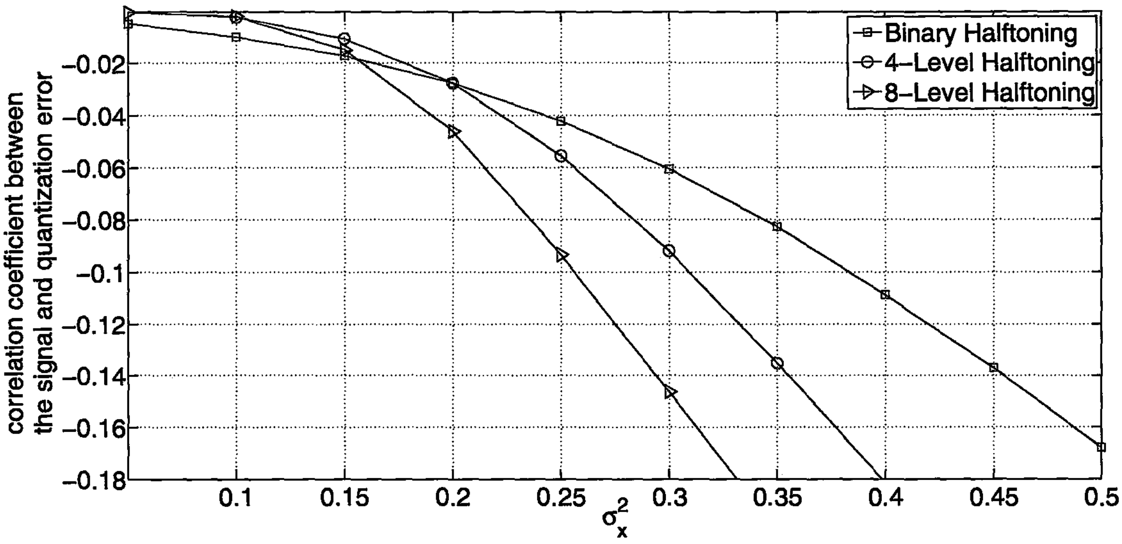

FIGURE 3.5: The correlation coefficient between the input signal and the quantization error versus the variance of the input signal σ_x^2 for different halftoning levels.

input signal, a numerical simulation was performed. For the simulation, a sequence of random continuous-tone SDMT modulated frames were generated. The resulting frames where halftoned using the error diffusion system illustrated in Figure 3.1, with an error diffusion filter,

$$\jmath = \begin{bmatrix} 0 & 0.9 \\ 0.9 & -0.8 \end{bmatrix},$$

and different halftoning levels. To study the effect of the average electrical signal power, σ_x^2, on the stability of the halftoning system, the correlation coefficient between the quantization error and the input signal was computed as a function of the signal power. The correlation coefficient can be defined as,

$$\operatorname{corr}\{q, x\} = \frac{\mathbb{E}\,[qx]}{\sigma_x \sigma_q} \tag{3.4}$$

The results of this simulation are plotted in Figure 3.5. From the figure, it can be seen that the quantization error is negatively correlated with input signal, this behavior can be explained by the negative feedback loop in the error diffusion system. Notice also that correlation coefficient changes with the number of halftoning levels. This behavior is attributed to the definition of saturation, i.e., the signal saturates the quantizer if the input signal is greater that $1 + \Delta$, or less that $-1 - \Delta$. As the number of halftoning levels is increased, Δ is reduced. Consequently, the input signal range over which the quantizer will not saturate is reduced. Hence, the quantizer will saturate at lower values for σ_x^2 when multilevel halftoning is used. The saturation results in an increase in the correlation coefficient between the resulting quantization error and the input signal. Figure 3.5 also shows that as the signal power increases, the magnitude of the correlation coefficient between the quantization error and the signal increases. As the magnitude of the correlation coefficient increases, the more likely the system will become unstable. This instability is due to the constructive interactions between the quantization error and the input signal, thus, driving the quantizer to saturate. From the numerical simulation, an acceptable and conservative value of σ_x^2 was found to be equal to 0.2. This value of σ_x^2 guarantees a correlation coefficient of 3% for binary and 4-level halftoned systems. In a future work, a more rigorous study of σ_x^2 on the stability of the system should be performed.

Once a linear model is obtained, the power spectral density of the closed loop quantization noise $\tilde{q}$ can be written as [31],

$$\Phi_{\tilde{q}} = N_1 N_2 \sigma_q^2 |1 - J[k_1, k_2]|^2 \tag{3.5}$$

where $\tilde{q} = x' - x$ is the difference between the continuous-tone and the halftoned images, N_1 and N_2 are the image dimensions, and J is the 2D DFT of the error diffusion filter j. Notice that the power spectral density of the quantizer error, $N_1 N_2 \sigma_q^2$, is being shaped by the term $|1 - J[k_1, k_2]|^2$.

Typically, the error diffusion filter j is designed to increase the perceptual quality of a halftoned image. From a communication perspective, it is desired to maximize the aggregate channel capacity rather than the image quality. To maximize the capacity, the error diffusion filter is designed to shape the quantization noise to the high frequency region of the spectrum [31, 55]. By shaping the quantization noise to the high frequency spectrum, it is attenuated by the spatial low-pass frequency response of the channel OTF. As a result, the received image is the continuous-tone data image with some residual quantization noise. Figure 3.6 illustrates the effects of the channel on a binary-level halftoned image. In Figure 3.6(c), notice that by halftoning the image, quantization noise is added to the high frequency spectrum of the image. As the image passes though the channel, its high frequency content is attenuated by the spatial low-pass frequency response of the channel OTF. The spatial frequency response of the received image is shown in Figure 3.6(d).

3.2.2 Halftoned SDMT Modulation

A block diagram of the halftoned SDMT transmitter is shown in Figure 3.7. A transmit SDMT modulated frame, x_T, is formed by halftoning the continuous-tone SDMT frame, x, into a multilevel frame, x', using the error diffusion filter in Figure 3.1. The amplitudes of the halftoned image are bounded between -1 and 1 due to the quantizer response shown in Figure 3.2. To preserve periodicity, a cyclic extension is appended to the halftoned image as in Section 2.3.2.3. To ensure non-negativity, a DC bias of +1 is added. Finally, the image is transmitted by a multiplication with a constant P_t as to satisfy the average amplitude constraints. At the receiver side, the normalized received image in discrete spatial frequency domain $[k_1, k_2]$ can be expressed by,

$$\frac{X_R[k_1,k_2]}{P_t H[k_1,k_2]} = X[k_1,k_2] + N_1 N_2 \delta[k_1,k_2] + \tilde{Q}[k_1,k_2] + \tilde{\Psi}[k_1,k_2] \tag{3.6}$$

where X_R is the 2D DFT of the received frame x_R, X is the 2D DFT of the continuous-tone SDMT frame x, $\tilde{Q}[k_1,k_2] = Q[k_1,k_2]\,(1 - J[k_1,k_2])$ is the 2D DFT of the closed

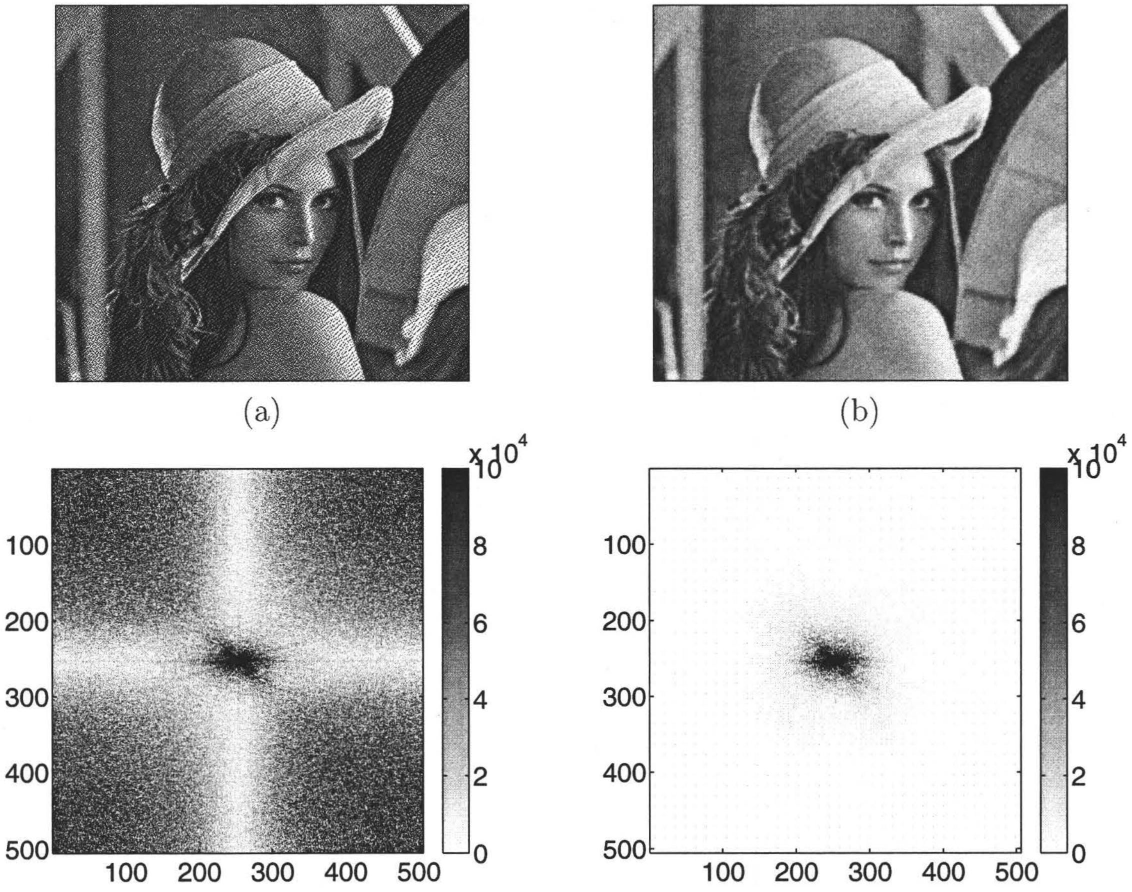

(c) (d)

FIGURE 3.6: An illustration of the channel effects on a halftoned image. (a) A halftoned image at transmit side, (b) The image at the receive side, (c) the spatial frequency spectrum of the image at the transmitter, (d) the spatial frequency spectrum of the image at the receiver.

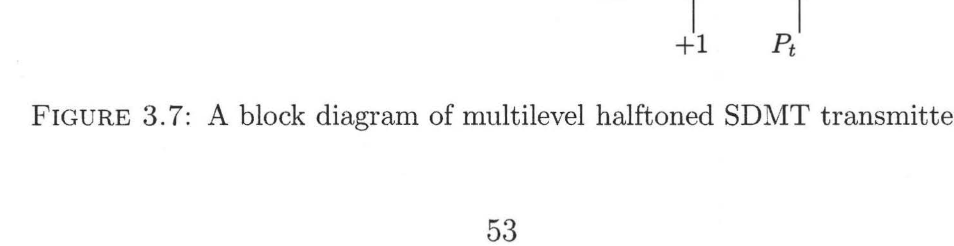

FIGURE 3.7: A block diagram of multilevel halftoned SDMT transmitter.

loop quantization noise $\tilde{q}$, and $\tilde{\Psi}[k_1, k_2] = \Psi[k_1, k_2]/(P_t H[k_1, k_2])$ is the effective channel Gaussian noise. From (3.6), the received frame is equivalent to a biased continuous-tone SDMT frame, contaminated by quantization noise and channel noise. Moreover, the equation implies that the wireless optical MIMO channel can be modeled as a number of independent Gaussian channels. As a result, the linear model in (3.5) can be used to estimate the aggregate channel capacity [31],

$$C \approx \frac{1}{2} \sum_{k_1=0}^{N_1-1} \sum_{k_2=0}^{N_2-1} \log \left(1 + \frac{\Phi_x[k_1, k_2]}{\Phi_{\tilde{q}}[k_1, k_2] + \Phi_{\tilde{\psi}}[k_1, k_2]} \right), \tag{3.7}$$

where $\Phi_x[k_1, k_2]$ is the electrical power allocated to frequency bin $[k_1, k_2]$, $\Phi_{\tilde{q}}[k_1, k_2]$ and $\Phi_{\tilde{\psi}}[k_1, k_2]$ are the PSDs of quantization noise and equivalent channel noise respectively, N_1 and N_2 are the number of discrete frequency bins. Notice that the capacity in (3.7) is only valid under the assumption of signal-independent, and white quantizer error. The larger the total input electrical signal power, the more likely this assumption is to fail.

Given the average electrical power per channel, σ_x^2, the channel capacity in (3.7) is maximized by pouring the total available electrical power $N_1 N_2 \sigma_x^2$ over the total noise surface $\Phi_{\tilde{q}} + \Phi_{\tilde{\psi}}$. From (3.7), there are two possible regions of operation :

- The optical power limited region: where the total noise power is dominated by the channel noise, i.e. $\Phi_{\tilde{q}} \ll \Phi_{\tilde{\psi}}$. For this region, the allocated power is shown in Figure 3.8. In this region, the capacity is limited by the amount of power available in the system, and the channel noise. As a result, this mode of operation constitute an upper bound on the channel capacity for a given channel noise.

- The quantization noise limited region: where the total noise power is dominated by quantization noise, i.e. $\Phi_{\tilde{q}} \gg \Phi_{\tilde{\psi}}$. For this region, the allocated power is shown in Figure 3.9. In this region of operation, the capacity is limited by

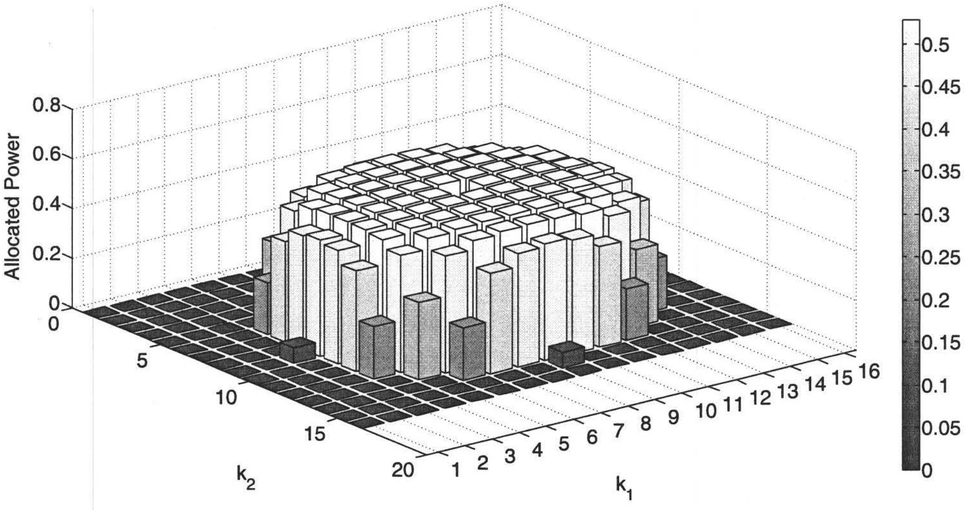

FIGURE 3.8: The optimal power allocation, Φ_x, for an optical power limited system. The total available power is poured using the water pouring algorithm over the noise surface $\Phi_{\tilde{q}} + \Phi_{\tilde{\psi}}$, when $\Phi_{\tilde{q}} \ll \Phi_{\tilde{\psi}}$.

the added quantization noise. As a result, gains in channel capacity can be achieved by reducing the added quantization noise power for a given channel noise. Notice that as the power of quantization noise is reduced, the system moves from a quantization noise limited to an optical power limited region of operation.

To maximize channel capacity in (3.7), the PSD of quantization noise, $\Phi_{\tilde{q}}$, needs to be minimized. From (3.5), there are two methods to minimize $\Phi_{\tilde{q}}$. The first method is to reduce the quantization noise power σ_q^2, this is achieved using multilevel halftoning. The second method is to use higher order noise shaping to give more degrees of freedom to shape the quantization noise away from the transmit data. From the discussion presented in this section, the ultimate goal is to design the transmitter to reduce the effect of quantization noise on the channel capacity. Thus, moving from a quantization noise limited to an optical power limited region of operation.

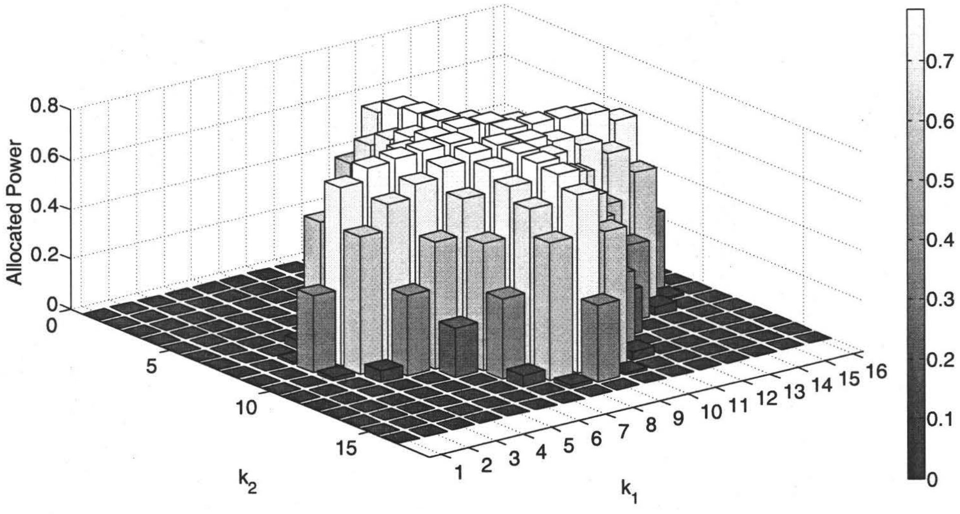

FIGURE 3.9: The optimal power allocation, Φ_x, for a quantization noise limited system. The total available power is poured using the water pouring algorithm over the noise surface $\Phi_{\tilde{q}} + \Phi_{\tilde{\psi}}$, when $\Phi_{\tilde{q}} \gg \Phi_{\tilde{\psi}}$.

3.3 Multilevel Error Diffusion

Multilevel error diffusion is a generalization of binary-level error diffusion to multiple levels. In imaging systems, increasing the number of halftoning levels results in increasing the perceptual quality of the halftoned image as shown in Figure 3.10. The increase in the perceptual quality of the image is attributed to a reduction in the power of quantization noise, σ_q^2. Therefore, as the number of halftoning levels is increased, the power of quantization noise is reduced. In Figure 3.11, the spatial frequency spectrums of the halftoned images are shown. From Figure 3.11(a), notice that information about image features are located in the low-band spectrum. In Figures 3.11(b), (c) and (d), notice that increasing the number of halftoning levels reduces the amount of quantization noise present. Moreover, notice that the added quantization noise is shaped towards the high frequency band of the halftoned images spectrum.

Multilevel halftoning can also be applied in wireless optical MIMO SDMT

(a) (b)

(c) (d)

FIGURE 3.10: An illustration of the effects of multilevel halftoning on images, (a) Continuous-tone image, (b) Binary halftoned image, (c) 4-level halftoned image, (d) 8-level halftoned image. Notice that as the number of halftoning levels is increased, the perceptual quality of the image is enhanced. The increase in perceptual quality is due to the lower quantization noise power.

systems to achieve a reduction in quantization noise power. From (3.5), it can be seen that for a given frame size and an error diffusion filter, the power spectral density of the quantization noise, $\Phi_{\tilde{q}}$, is directly proportional to the quantization noise power σ_q^2. Since σ_q^2 decreases with increasing number halftoning levels, increasing the number of halftoning levels results in reducing the PSD of the quantization noise, $\Phi_{\tilde{q}}$. Referring back to (3.7), it can be deduced that as the number of halftoning levels is increased, the PSD of quantization noise is reduced with respect to the PSD of the

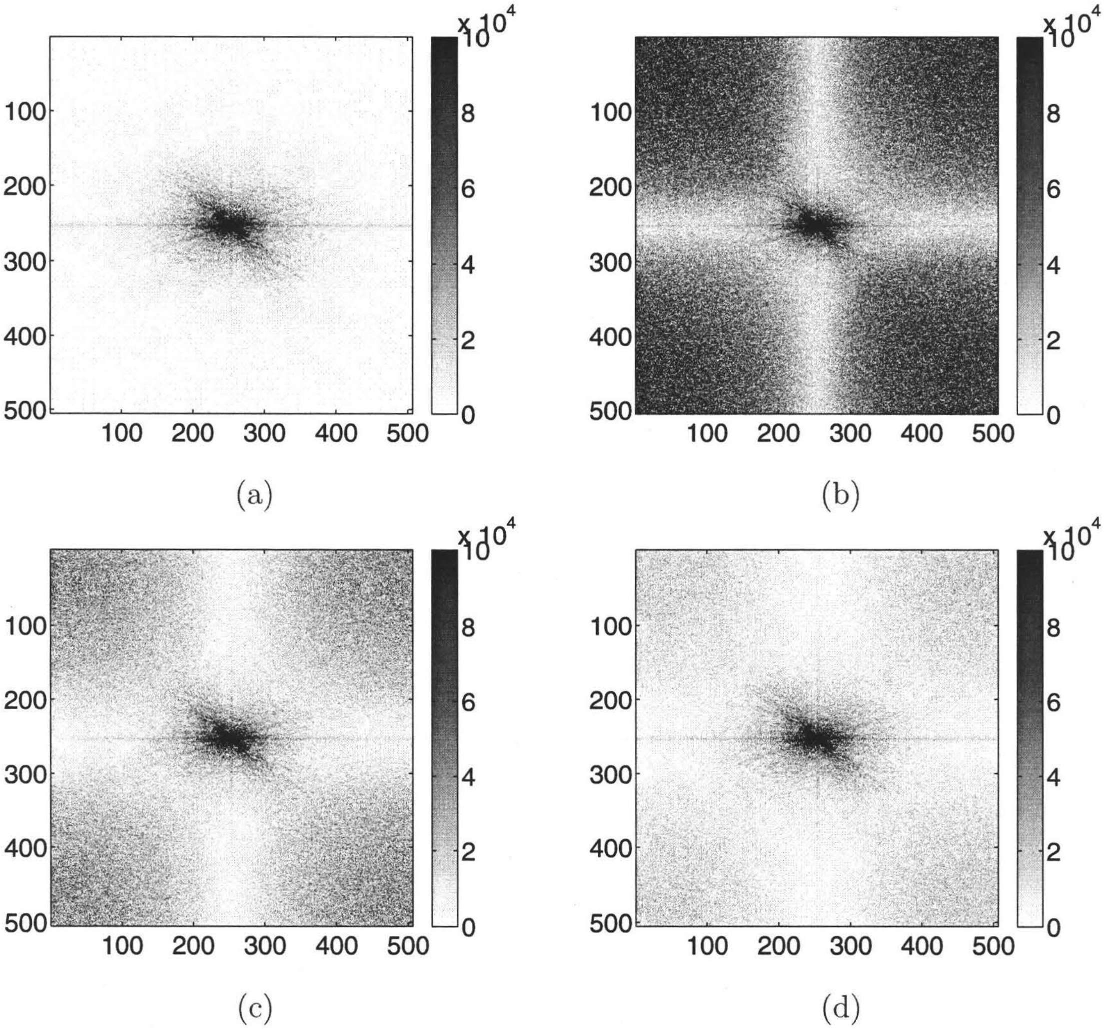

(a) (b) (c) (d)

FIGURE 3.11: The spatial frequency spectrum of the halftoned images in Figure 3.10, (a) Continuous tone, (b) Binary halftoned, (c) 4-level halftoned, (d) 8-level halftoned. Notice that as the number of halftoning levels is increased, the quantization noise power in the spatial frequency spectrum is reduced.

channel noise. Thereby, shifting the operating point of the communication link from a quantization noise limited to an optical power limited. From the discussion presented in Section 3.2.2, it can be shown that as the system moves from a quantization noise limited to an optical power limited region of operations, gains in channel capacity are achieved.

3.3.1 Linear Quantizer Model

Halftoning is achieved by passing the signal through a quantizer. The quantizer is assumed to be uniform, with steps equally spaced between -1 and 1 as in Figure 3.2. Figure 3.1 shows a multilevel error diffusion system. To derive a linear model for this system, it is assumed that the quantization noise is white and signal independent. Under these assumptions, the variance σ_v^2 of the quantizer input can written as [31],

$$\sigma_v^2 = \sigma_x^2 + \sigma_q^2 \xi_j \tag{3.8}$$

where ξ_j is the energy of the filter. In this section, assume that the filter energy is given. In Section 3.4, a more detailed look at the filter is considered.

In SDMT signaling, the distribution of amplitudes of an SDMT frame is approximated by a Gaussian distribution with variance equal to its average power σ_x^2 [74, Ch.3, sec.3]. Therefore, to preserve the linearity assumption and to prevent the quantizer from saturation, σ_x^2 must be bounded [31]. From the linearity assumption and the Gaussian statistics of the SDMT frame, the quantizer input v is Gaussian distributed as well. Therefore, the quantizer noise variance can be approximated by,

$$\begin{aligned}
\sigma_q^2 &= \int_{-\infty}^{-\Delta(L/2-1)} (-1-v)^2 f_v(v)dv \\
&\quad + \sum_{l=1}^{L-2} \int_{\Delta(l-L/2)}^{\Delta(l-L/2+1)} (-1+l\Delta-v)^2 f_v(v)dv \\
&\quad + \int_{\Delta(L/2-1)}^{\infty} (1-v)^2 f_v(v)dv \qquad (3.9) \\
&= 1+\sigma_v^2+\sum_{l=0}^{L-2}\left[\left(\Delta^2(2l+1)-2\Delta\right) Q\left(\frac{\Delta}{\sigma_v}(l-L/2+1)\right)\right. \\
&\quad \left. -\frac{2\sigma_v\Delta}{\sqrt{2\pi}}\exp\left(-\frac{\Delta^2}{2\sigma_v^2}(l-L/2+1)^2\right)\right] \qquad (3.10)
\end{aligned}$$

where $L \in \mathbb{Z}^+$ and $L \geq 2$ is the number of quantization levels, $\Delta = 2/(L-1)$ is the step size, $f_v(v)$ is a zero-mean Gaussian probability density function, and $\mathcal{Q}(.)$ is the cumulative distribution function for a normal distribution. To estimate σ_q^2, the value of σ_v^2 in (3.8) is substituted in (3.10). The resulting equation is solved using Newton's root finding algorithm to get an estimate of the quantizer noise power.

Figure 3.12 plots the linear model estimation of σ_q^2, and the simulated quantization noise variance versus the number quantization levels. For both plots, the average electrical power, σ_x^2, is equal to 0.2. The simulated quantization noise variance was obtained by simulating a one-dimensional SDMT signal. The SDMT signal was then halftoned using $\Delta\Sigma$ modulation, and the variance of the resulting quantization noise was computed and averaged over many occurrences. From figure, notice that the model increases in accuracy as the number of quantization levels is increased. Notice also that the quantization noise power does not go to zero as the number of levels is increased. This is due to clipping introduced by the quantizer since its input must be bounded between -1 and 1. Moreover, notice that the quantization noise derived from the linear model is underestimated for all quantization levels, except when $L = 2$. As a result, the channel capacity computed using the linear model is overestimated.

3.3.2 Simulation Results

To get an estimate for the channel capacity, (3.8) and (3.10) are used to find σ_q^2, the value of σ_q^2 is substituted in (3.5) to compute the PSD of quantization noise, the PSD of quantization noise is used to compute the channel capacity using (3.7). The estimated channel capacity was simulated for binary [31, 55], multilevel, and continuous-tone halftoned SDMT systems. The channel capacity was simulated using measured channel OTF and noise variances from [55] and Table 2.1 with $\sigma_x^2 = 0.2$. In Figure 3.13, the capacity in kbits per frame is plotted versus the frame rate for

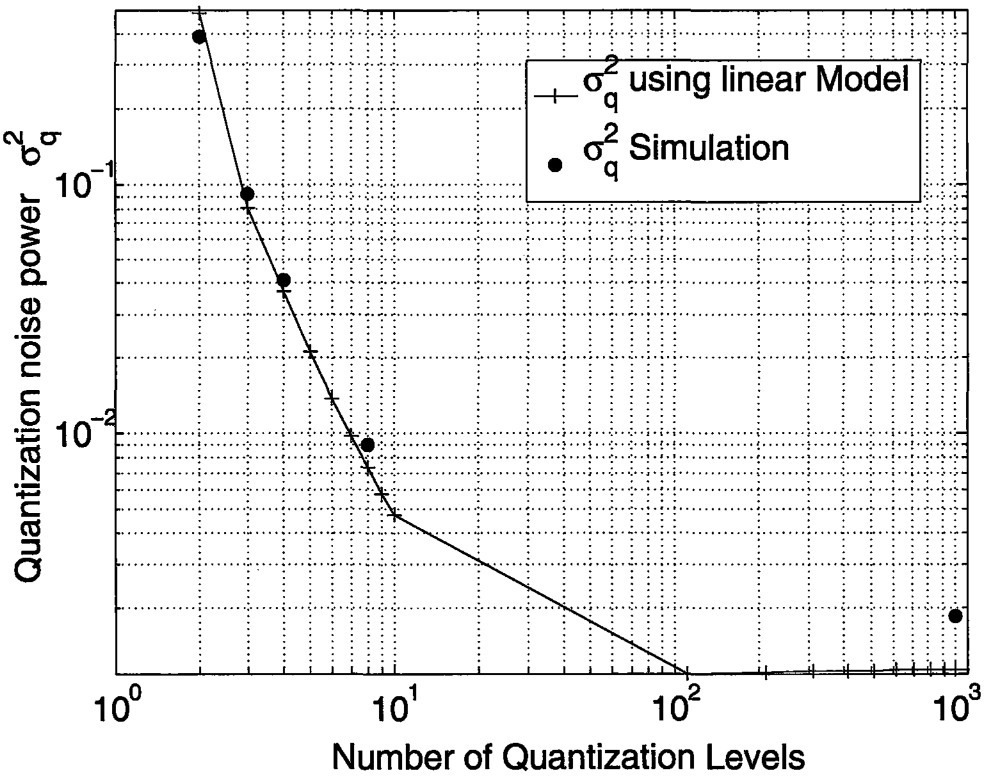

FIGURE 3.12: Simulated v.s. linear model predictions for the quantization noise variance, σ_q^2, as the number of quantization levels is changed. For both plots, the average electrical power $\sigma_x^2 = 0.2$.

different halftoning levels and frame sizes. Notice that for a system operating in quantization noise limited region, the channel capacity is significantly increased as the number of halftoning levels is increased. Also, one can see that the capacity per frame is inversely proportional to the frame rate. As the frame rate is increased, the capacity per frame is decreases. This decrease is due to the increase in channel noise as shown in the measurements in Table 2.1. From a practical perspective, most links will be operating in the quantization noise limited region due to the low frame rates supported by the receiver. As a result, significant gains in channel capacity can be attained using multilevel halftoning. For systems operating in the optical power limited region, it is best to use binary halftoning since it approaches the channel t

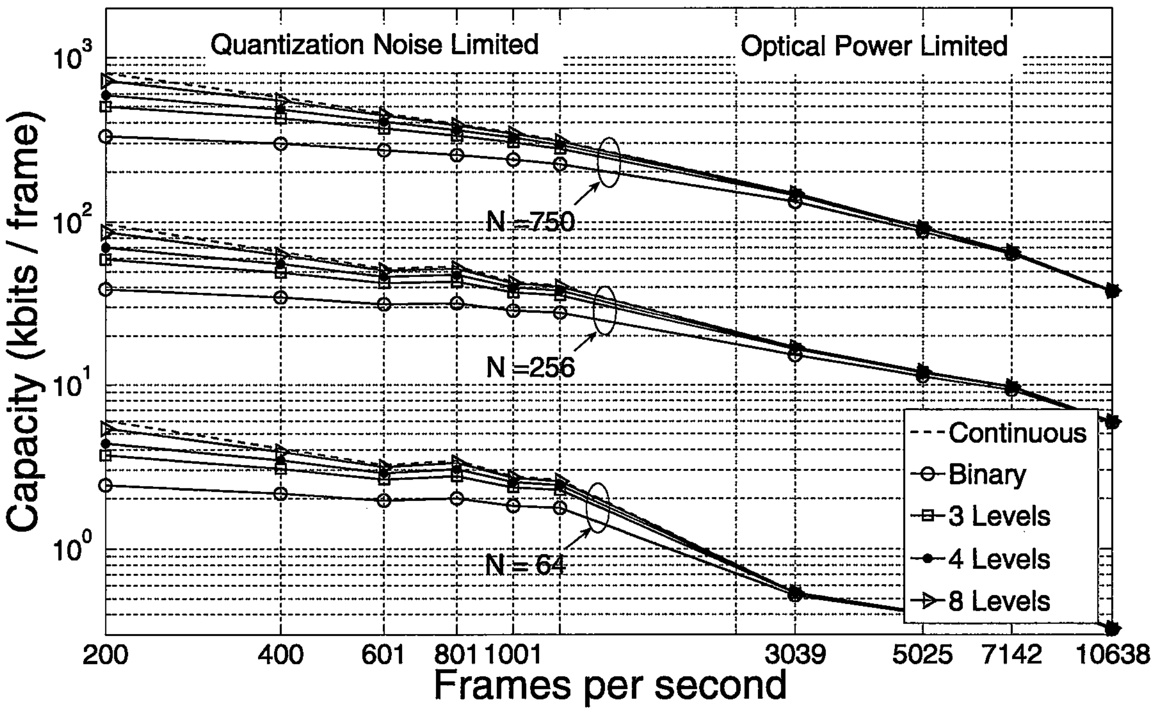

FIGURE 3.13: Capacity estimates of a wireless optical MIMO system measured in Kbits/frame, for different frame sizes and halftoning levels.

capacity without the increase in transmitter complexity.

Figure 3.14 shows the capacity in megabits per second versus the frame rate for different halftoning levels and frame sizes. Although the capacity per frame decreases as the frame rate increases, there is a net gain in the channel capacity in terms of Mbps. This is due to the capacity drop being offset by the increase in the number of frames per second transmitted, thus leading to a net increase in capacity in Mbps. From the figure, notice also that the channel capacity in Mbps is maximized when the frame rate is 7142fps. As the frame rate is increased beyond this value, the channel capacity is decreased. The decrease in the channel capacity is due to the non-whiteness of the measured noise as seen in Table 2.1. This may be due to circuit issues inside the camera while operating at its maximum frame rate.

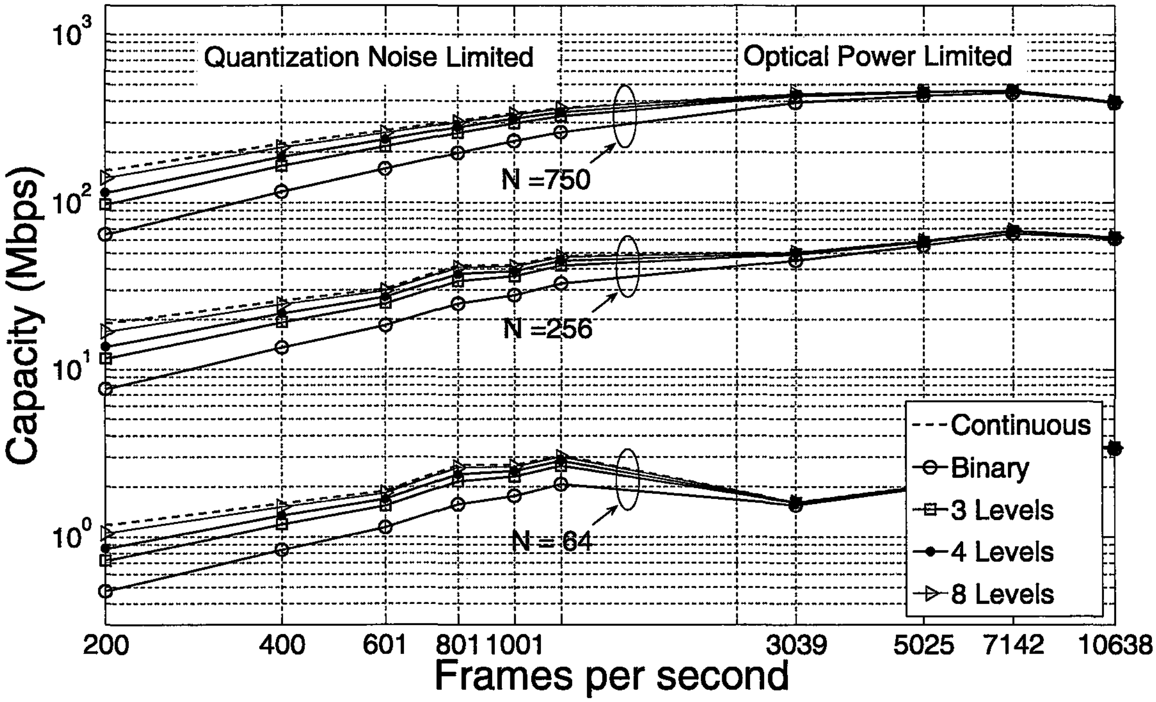

FIGURE 3.14: Capacity estimates of a wireless optical MIMO system measured in Mbits/s, for different frame sizes and halftoning levels.

3.3.3 Practical Implementation

In practice, multilevel halftoning can be achieved directly using a multilevel spatial light modulator. Such modulators are built using LCD technology. Theoretically, the direct implementation of multilevel halftoning using a multilevel transmitter, can achieve gains in channel capacity over binary transmission as shown in Figures 3.13 and 3.14. Although gains in capacity are attained, multilevel transmitters have a slow frame rate. Moreover, they suffer from gamma distortion [52, Chapter 8], that can affect the overall performance of the system.

Multilevel halftoning can also be implemented indirectly using a binary SLM. Using this implementation, the frame rate is traded with amplitude resolution. The indirect implementation requires the use of coding along with binary transmission. In this method, coding is used to map the multilevel image into a sequence of binary

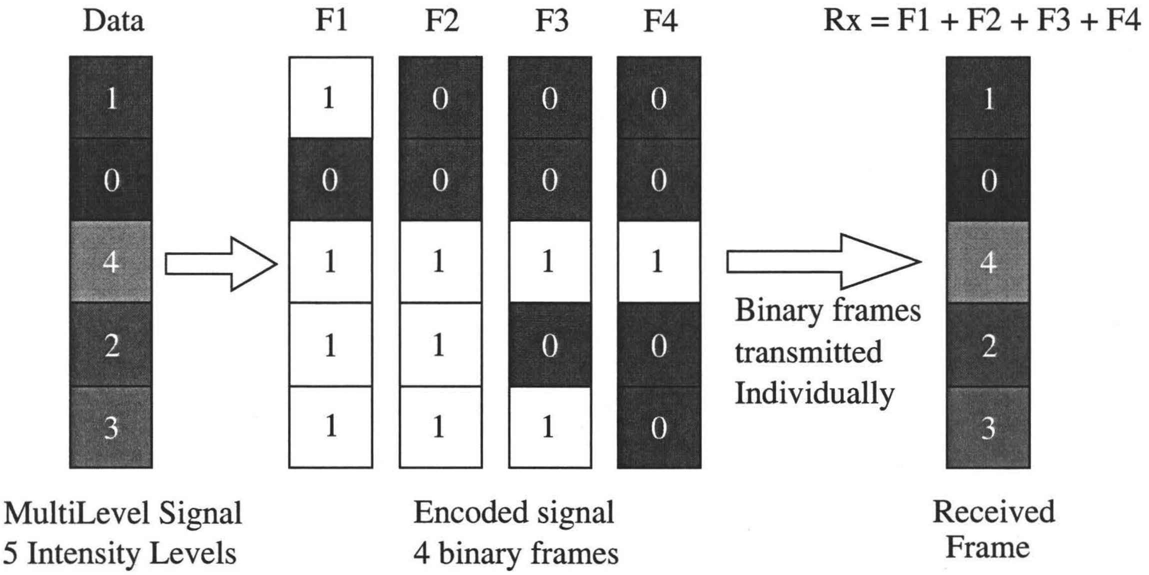

FIGURE 3.15: Thermometer code applied to a 5-level intensity signal.

frames. These binary frames are transmitted across the channel. At receive side, the sequence of binary frames is used to reconstruct the multilevel signal. One possible coding technique is termed *thermometer coding.* In a thermometer code an L level quantized signal is coded into $L - 1$ binary frames. This method is illustrated in Figure 3.15.

In Figure 3.15, a 5-level intensity data image is encoded into four binary intensity level frames. These binary frames are transmitted across the channel. At receive side, the photodetector array integrates the transmitted binary frames in time. The period of integration is set by the exposure time. In a binary system, where data images are binary, the exposure time is equal to the frame rate. But in multilevel systems, the exposure time must be $L-1$ times longer than the transmit frame rate. This is done to insure that the sampled signal is the sum of all binary frames in the encoded sequence. Consequently, the received image is the original multilevel image.

Figure 3.16 shows the capacity in kbits/frame for multilevel halftoned systems

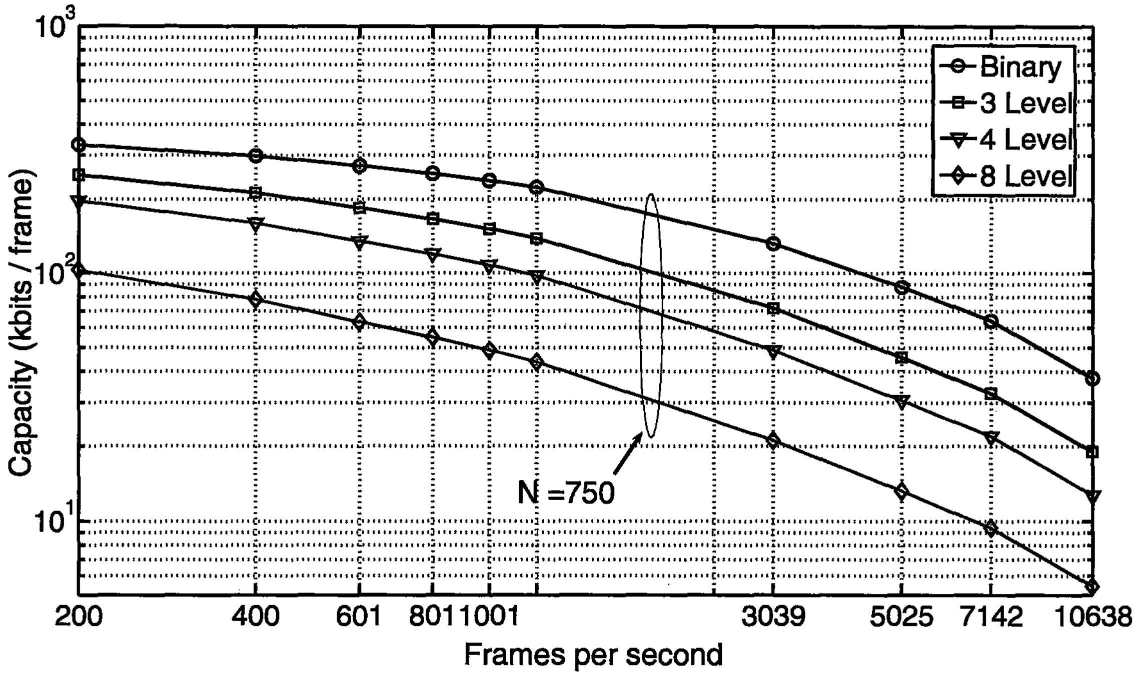

FIGURE 3.16: Capacity in kbits/frame versus the frame rate for multilevel halftoning systems implemented using a binary transmitter with thermometer coding.

implemented using binary transmitter and thermometer coding. The plots were obtained by dividing the rates in Figure 3.13 by the number of binary frames needed to transmit the information. From the figure, notice that the channel capacity of a multilevel halftoned system implemented using a binary transmitter is lower than a binary-level halftoned one. For example, the capacity of a 4-level system operating at 200 frames per second is about 600 kbits per frame as in Figure 3.13. The capacity of a binary-level system at the same frame rate is about 320 kbits per frame. A 4-level system requires 3 binary frames to be transmitted for each multilevel frame. Hence, the capacity per binary frame transmitted is 600/3 $\approx$ 200 kbits per frame as shown in Figure 3.16, which is less that the capacity of a binary halftoned frame. Therefore, one can say that for a binary SLM, no gains in capacity can be achieved by using multilevel halftoning, if there are no restrictions on receiver frame rate. In practice, since receive senosors are far slower than binary SLMs, multilevel halftoning can be applied using binary transmitters to achieve gains in capacity.

3.4 Optimal Design for Noise Shaping Filters

From (3.5), noise shaping is realized by the term $|1 - J[k_1, k_2]|^2$. In this section, the channel capacity is maximized with respect to the filter parameters, for the first and second order error diffusion filters j.

3.4.1 Error Diffusion Filter

In this work, to simplify the optimization problem, the error diffusion filters are assumed to be causal and symmetric. In this Chapter, causality is defined relative to a scan path. For a given scan path, an error diffusion filter is causal if the quantization noise from the current pixel is distributed among the un-quantized pixels as shown in Figure 3.3.

A symmetric noise shaping filter is defined filter that satisfies $j = j^T$. This condition was adopted by analogy to the circular symmetry of the channel OTF in the spatial frequency domain. For example, causal, symmetric, first order noise shaping filter has the form,

$$j = \begin{bmatrix} 0 & a \\ a & b \end{bmatrix} \tag{3.11}$$

Notice that causality is satisfied since quantization error from current pixel (A) is distributed among the un-quantized pixels (B) (C) and (D) according to preset ratios defined by j, as shown in Figure 3.3. To design the optimal error diffusion filters, sequential quadratic programming is used to maximize the aggregate channel capacity with respect to the filter parameters.

Mathematically, second order noise shaping is achieved by squaring the noise shaping term [86] as follows,

$$\begin{aligned}(1 - J[k_1, k_2])^2 &= 1 + J[k_1, k_2]^2 - 2J[k_1, k_2] \\ &= 1 - \tilde{J}[k_1, k_2] \qquad (3.12)\end{aligned}$$

where $\tilde{J} = 2J - J^2$, and it represents the spatial frequency response of the second order noise shaping filter. In spatial domain (3.12) can be written as,

$$\begin{aligned}\tilde{J} &\overset{\text{DFT}}{\longleftrightarrow} \tilde{j} \\ 2J - J^2 &\overset{\text{DFT}}{\longleftrightarrow} 2j - j * j \qquad (3.13)\end{aligned}$$

where $\tilde{J}$ and J are the 2D discrete Fourier transforms of $\tilde{j}$ and j respectively, and $*$ is the 2D convolution. Note that a second order noise shaping filter $\tilde{j}$ is realized by convolving a first order filter j with itself, resulting in a 3×3 topology,

$$\tilde{j} = \begin{bmatrix} 0 & a & b \\ a & d & c \\ b & c & e \end{bmatrix} \qquad (3.14)$$

In the derivation process, a notion of the filter energy is needed. For the purpose of this work, the filter energy ξ_j is defined as,

$$\xi_j = ||j||_F^2 \qquad (3.15)$$

where $||j||_F$ is the Frobenius norm of the error diffusion filter j. In [31], an upper bound on the filter energy, ξ_j, was obtained and is given as follows,

$$\xi_j \leq \frac{\pi}{\pi - 2} \qquad (3.16)$$

A more detailed look about the derivation of this bound is presented in Section 3.4.2.2.

From Section 2.3.3, it was shown that for a continuous-tone SDMT system, it is desired to send no information in the DC bin to save optical power. Having a null at DC implies that the continuous-tone data image in spatial domain has a zero mean. To save optical power in halftoned-SDMT systems, the halftoned images must have a zero mean. Since the halftoned image can be modeled as a zero-mean continuous-tone data image with added shaped quantization noise, the shaped quantization noise must have a zero mean for the resulting halftoned image to have a zero mean. To ensure that the shaped quantization noise has a zero mean, the error diffusion filter $\jmath$ is chosen to have unity DC gain. Having unity DC gain implies that the noise shaping term, $(1 - J[k_1, k_2])$, is null at DC. As a result, the halftoned image generated by adding the zero mean continuous-tone image with the zero mean shaped quantization noise will have a zero mean. To ensure that the error diffusion filter, $\jmath$, has unity gain at DC, the following condition must be satisfied,

$$\mathbf{1}^T \jmath \mathbf{1} = 1 \tag{3.17}$$

where $\mathbf{1} = [1\ 1 \ldots 1]^T$ is a vector of ones, the size of which is determined by the size of the error diffusion filter $\jmath$.

3.4.2 Optimization Problem

To design an optimal filter, the problem of maximizing the capacity must be casted in an optimization framework. This step is necessary as to apply known optimization methods to obtain a possible design and check uniqueness. In this section, the initial optimization problem and its constraints are presented. The optimization problem is reformulated and studied in terms of convexity. A design technique is then chosen and applied to obtain optimal filter parameters. Mathematically, maximizing the channel capacity can be expressed by the following argument,

$$\max_{\Phi_x, J} \quad \frac{1}{2}\sum_{k_1=0}^{N_1-1}\sum_{k_2=0}^{N_2-1}\log\left(1+\frac{\Phi_x[k_1,k_2]}{N_1N_2\sigma_q^2|1-J[k_1,k_2]|^2+\frac{N_1N_2}{|\rho H[k_1,k_2]|^2}}\right) \tag{3.18}$$

subject to,

$$\Phi_x \geq 0 \tag{3.19}$$

$$\frac{1}{N_1N_2}\sum \Phi_x[k_1,k_2] = \sigma_x^2 N_1 N_2 \tag{3.20}$$

$$||\jmath||_F^2 \leq \frac{\pi}{\pi-2} \tag{3.21}$$

$$\mathbf{1}^T \jmath \mathbf{1} = 1 \tag{3.22}$$

where $\rho = P_t H_0/\sigma_\psi$, with H_0 denotes the DC gain of the channel, and σ_ψ is the standard deviation of the channel noise. The condition in (3.19) requires that all the elements of the matrix Φ_x to be positive. This condition is reflects the non-negativty of the power allocated in each bin, and it is implicit in the optimization problem. Notice that the optimization problem in its current form can not be solved using available optimization tools. As a result, further problem reformulation is needed. To reformulate the problem, the constraints and the objective function are simplified, and their convexity is studied.

3.4.2.1 Power Constraint Reformulation

The first constraint in (3.20) of the optimization problem signifies the finite electrical power available to transmit data. The power limitation arise from conditions to maintain system stability and the validity of the linear model [31]. From (3.20), it can be seen that the total power of the system must not exceed the average electrical power per channel σ_x^2 multiplied by the number of channels. This condition can be rewritten as,

$$\begin{aligned} \frac{1}{N_1 N_2} \sum \Phi_x[k_1, k_2] &= \sigma_x^2 N_1 N_2 \\ \sum \Phi_x[k_1, k_2] &= \sigma_x^2 \left(N_1 N_2\right)^2 \end{aligned} \tag{3.23}$$

Note that Φ_x is a matrix with variable entries corresponding to the electrical power allocated per channel. The reformulated constraint in (3.23) represents the sum of variables. Therefore, it is classified as a linear equality constraint and is convex.

3.4.2.2 Filter Energy Constraint Reformulation

The second constraint in (3.21) represents a bound on the error diffusion filter energy. This condition is to ensure the validity of the linear model with the assumptions made. The linear model for the binary halftoned system can be expressed as [31],

$$\sigma_v^2 = \sigma_x^2 + \sigma_q^2 \xi_j \tag{3.24}$$

where σ_v^2 is the variance of the quantizer input signal, σ_x^2 is the average electrical power, and ξ_j is the energy of the filter as defined in (3.15). The quantization noise power σ_q^2 for the binary system is equal to [31],

$$\sigma_q^2 = 1 + \sigma_v^2 - \frac{4\sigma_v}{\sqrt{2\pi}} \tag{3.25}$$

Using equations (3.24) and (3.25), the upper bound (3.21) on the filter energy ξ_j was derived in [31].

Using (3.15) the energy constraint for the first order filter is reformulated as,

$$\begin{aligned}
\|j\|_F^2 &\leq \frac{\pi}{\pi-2} \\
2a^2+b^2 &\leq \frac{\pi}{\pi-2} \\
\begin{bmatrix} a & b \end{bmatrix} \begin{bmatrix} 2 & 0 \\ 0 & 1 \end{bmatrix} \begin{bmatrix} a \\ b \end{bmatrix} &\leq \frac{\pi}{\pi-2} \\
y^T G y &\leq \frac{\pi}{\pi-2} \qquad (3.26)
\end{aligned}$$

where y is the optimization variable. A similar argument is applied for the second order error diffusion filter to obtain a constraint, with the following values for G and y

$$\begin{aligned}
y^T &= \begin{bmatrix} a & b & c & d & e \end{bmatrix} \\
G &= \begin{bmatrix} 2 & 0 & 0 & 0 & 0 \\ 0 & 2 & 0 & 0 & 0 \\ 0 & 0 & 2 & 0 & 0 \\ 0 & 0 & 0 & 1 & 0 \\ 0 & 0 & 0 & 0 & 1 \end{bmatrix}
\end{aligned}$$

Since the matrix G in both cases is positive semi-definite the constraint in (3.26) is a convex quadratic constraint with respect to the optimization variable y.

3.4.2.3 Unity DC Gain Constraint Reformulation

The third constraint in (3.22) represents a condition to satisfy unity DC gain. To simplify the optimization problem, this constraint is relaxed to expand the feasible region set. For the case of first order error diffusion, the relaxed constraint is given by,

$$\begin{aligned} \mathbf{1}^T j \mathbf{1} &\leq 1 \\ 2a + b &\leq 1 \\ \begin{bmatrix} 2 & 1 \end{bmatrix} \begin{bmatrix} a \\ b \end{bmatrix} &\leq 1 \\ \beta^T y &\leq 1 \end{aligned} \tag{3.27}$$

Similarly, the constraint for a second order filter is obtained and is equal to (3.27), with the following values for β and y

$$\begin{aligned} \beta^T &= \begin{bmatrix} 2 & 2 & 2 & 1 & 1 \end{bmatrix} \\ y^T &= \begin{bmatrix} a & b & c & d & e \end{bmatrix} \end{aligned}$$

Note that the reformulated inequality constraint in (3.27) is affine, and hence convex.

3.4.2.4 Objective Function Reformulation

From the objective function in (3.18), it can be seen that the capacity depends on the absolute value of the DFT of the filter j. In its current format, this equation is hard to analyze since it is not differentiable. Therefore, it is required to rewrite this term as a function of the optimization variable y. For a given filter j, the DFT is defined as follows,

$$J[k_1, k_2] = \sum_{n_1=0}^{N_1-1} \sum_{n_2=0}^{N_2-1} j[n_1, n_2] \exp\left(-i2\pi \left(\frac{n_1 k_1}{N_1} + \frac{n_2 k_2}{N_2}\right)\right) \tag{3.28}$$

By substituting (3.28) in $|1 - J[k_1, k_2]|^2$, an expression for the noise shaping term with respect to the filter parameters is obtained. The simplified expression is given as follows,

$$|1 - J[k_1, k_2]|^2 = \left(1 - a\cos\frac{2\pi k_2}{N_2} - a\cos\frac{2\pi k_1}{N_1} - b\cos 2\pi\left(\frac{k_1}{N_1} + \frac{k_2}{N_2}\right)\right)^2 + \left(a\sin\frac{2\pi k_2}{N_2} + a\sin\frac{2\pi k_1}{N_1} + b\sin 2\pi\left(\frac{k_1}{N_1} + \frac{k_2}{N_2}\right)\right)^2 \quad (3.29)$$

From (3.29), notice that the noise shaping term is a quadratic function of the filter elements. To simplify the equation further, trigonometric identities are used to factor (3.29) as a quadratic equation in terms of the filter coefficient vector y, as follows,

$$|1 - J[k_1, k_2]|^2 = y^T A[k_1, k_2] y + t^T[k_1, k_2] y + 1 \quad (3.30)$$

where,

$$\begin{aligned} y^T &= [\; a \quad b \;] \\ A[k_1, k_2] &= \begin{bmatrix} 2 + 2\cos\frac{2\pi k_1}{N_1}\cos\frac{2\pi k_2}{N_2} + 2\sin\frac{2\pi k_1}{N_1}\sin\frac{2\pi k_2}{N_2} & \cos\frac{2\pi k_1}{N_1} + \cos\frac{2\pi k_2}{N_2} \\ \cos\frac{2\pi k_1}{N_1} + \cos\frac{2\pi k_2}{N_2} & 1 \end{bmatrix} \\ t^T[k_1, k_2] &= \begin{bmatrix} -2\cos\frac{2\pi k_1}{N_1} - 2\cos\frac{2\pi k_2}{N_2} & -2\cos 2\pi\left(\frac{k_1}{N_1} + \frac{k_2}{N_2}\right) \end{bmatrix} \end{aligned}$$

To study the convexity of the noise shaping term in (3.30), it is necessary to look at the matrix $A[k_1, k_2]$. If $A[k_1, k_2]$ is positive semi-definite for all frequencies, then the left hand side of (3.30) is convex with respect to the optimization vector y. To prove that a matrix is positive semi-definite, it is necessary to prove that the determinant of the matrix is always positive. Mathematically this condition can be written as,

$$\det A[k_1, k_2] \geq 0 \qquad , \forall [k_1, k_2]$$

Assuming $\theta_1 = 2\pi k_1/N_1$ and $\theta_2 = 2\pi k_2/N_2$, the above condition simplifies to,

$$\det \begin{bmatrix} 2 + 2\cos\theta_1 \cos\theta_2 + 2\sin\theta_1 \sin\theta_2 & \cos\theta_1 + \cos\theta_2 \\ \cos\theta_1 + \cos\theta_2 & 1 \end{bmatrix} \geq 0$$
$$4\cos^2\left(\frac{\theta_1 - \theta_2}{2}\right)\sin^2\left(\frac{\theta_1 + \theta_2}{2}\right) \geq 0 \qquad (3.31)$$

Notice that the determinant of $A[k_1, k_2]$ in (3.31) is positive for all spatial frequencies $[k_1, k_2]$. Since $A[k_1, k_2]$ is positive semi-definite, one can conclude that the noise shaping function (3.30) is convex with respect to the optimization vector.

3.4.2.5 Reformulated Optimization Problem

Combining results from (3.23), (3.26), (3.27) and(3.30), the optimization problem in (3.18) can be written as,

$$\min_{\Phi_x, y} \quad -\frac{1}{2}\sum_{k_1=0}^{N_1-1}\sum_{k_2=0}^{N_2-1} \log\left(1 + \Phi_x[k_1, k_2] \middle/ \left[\frac{N_1 N_2}{|\rho H[k_1, k_2]|^2} + N_1 N_2 \sigma_q^2 \left(y^T A[k_1, k_2] y + t^T[k_1, k_2] y + 1\right)\right]\right) \qquad (3.32)$$

subject to,

$$\sum \Phi_x[k_1, k_2] = \sigma_x^2 \left(N_1 N_2\right)^2$$
$$y^T G y \leq \frac{\pi}{\pi - 2}$$
$$\beta^T y \leq 1$$

Note that maximizing a function is the same as minimizing the negative of that function, hence, the change in sign of the objective function. Notice that the energy

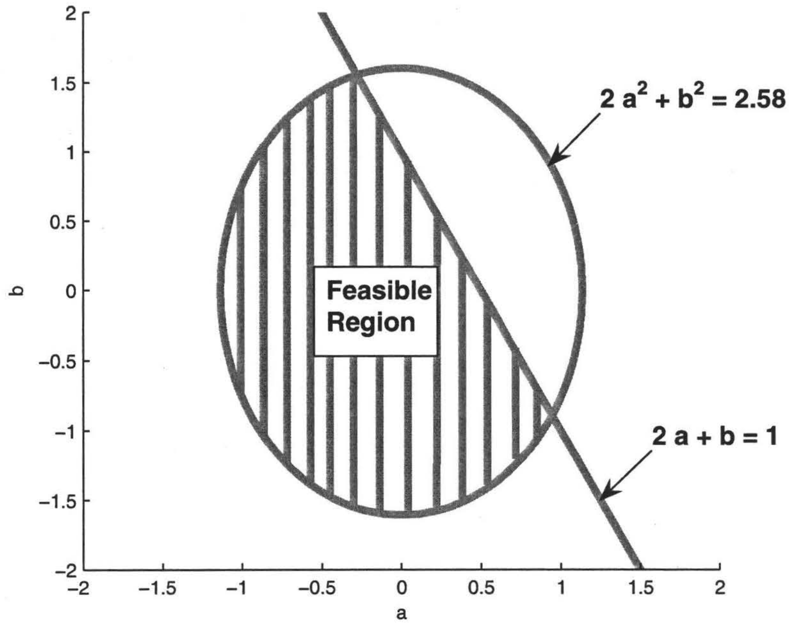

FIGURE 3.17: The feasible region for a 2×2 filter topology.

constraint in (3.26), and the relaxed unity DC gain condition in (3.27), define a feasible set for the filter coefficients. Graphically, the feasible set for a 2×2 filter topology is shown in Figure 3.17.

In order to choose an optimization technique suitable for the design process, it is necessary to study the convexity of the objective function. Two methods are considered to solve the problem, the first method (*joint problem*) involves joint optimization over the power matrix Φ_x as well as filter coefficient vector y, the second method (*disjoint problem*) considers the disjoint optimization of the variables. Disjoint optimization splits the problem of optimizing the capacity into two steps. In the first step, the power matrix Φ_x is optimized for a given y. The second step, involves optimizing the filter coefficient vector y for a given Φ_x. Both steps are repeated iteratively until solutions converge.

3.4.2.6 Convexity of the Joint Problem

In the joint optimization problem, the objective function in (3.32) is minimized with respect to Φ_x and y simultaneously. As in the case for all functions, the objective function can be convex or non-convex. In an attempt to study the convexity of the objective function, it is first decomposed into the sum of N_1N_2 terms. If each of the terms is convex, then their sum is convex [2], otherwise, nothing can be said about the convexity of their sum. From (3.32), a general formulation of the terms is given by,

$$f(y, \Phi_x[k_1, k_2]) = -\frac{1}{2}\log\left(1 + \Phi_x[k_1, k_2] \Bigg/ \left[\frac{N_1N_2}{|\rho H[k_1, k_2]|^2} + N_1N_2\sigma_q^2\left(y^T A[k_1, k_2]y + t^T[k_1, k_2]y + 1\right)\right]\right) \tag{3.33}$$

In an attempt to study the convexity of (3.33), the composition rule was used. The composition rule states that if $f(x) = h(g(x))$, then $f(x)$ is convex if h is convex and non-increasing and $g(x)$ is concave [2]. From (3.33), notice that $-\log$ is convex and non-increasing. Therefore, if the argument of the log is concave, then (3.33) is convex. The argument of the log is given by the following,

$$g(y, \Phi_x[k_1, k_2]) = 1 + \Phi_x[k_1, k_2] \Bigg/ \left[\frac{N_1N_2}{|\rho H[k_1, k_2]|^2} + N_1N_2\sigma_q^2\left(y^T A[k_1, k_2]y + t^T[k_1, k_2]y + 1\right)\right] \tag{3.34}$$

To study the concavity of (3.34), its Hessian matrix is computed. If the Hessian matrix is negative semi-definite then $g(y, \Phi_x[k_1, k_2])$ is concave. Some of the Hessian matrix coefficients were computed in terms of the vector of filter coefficients y, these terms are given below,

$$\begin{aligned}
\frac{\partial^2 g}{\partial \Phi_x^2[k_1,k_2]} &= 0 \\
\nabla_y \left(\frac{\partial g}{\partial \Phi_x[k_1,k_2]} \right) &= -2N_1N_2\sigma_q^2 \Big[A[k_1,k_2]y + t[k_1,k_2] \Big] \Big/ \Bigg[\frac{N_1N_2}{|\rho H[k_1,k_2]|^2} + \\
&\qquad N_1N_2\sigma_q^2 \left(y^T A[k_1,k_2]y + t^T[k_1,k_2]y + 1 \right) \Bigg]^2 \\
\frac{\partial}{\partial \Phi_x[k_1,k_2]} (\nabla_y g) &= \nabla_y \left(\frac{\partial g}{\partial \Phi_x[k_1,k_2]} \right)
\end{aligned}$$

Notice that one of the diagonal elements of the Hessian matrix is zero while the corresponding row and column are not. Therefore, it is concluded that the Hessian matrix is not negative semi-definite. A proof of this result is shown in Appendix A. Following from the non-negative semi-definiteness of the Hessian matrix, $g(y, \Phi_x[k_1,k_2])$ is determined to be non-concave. Consequently, the composition rule resulted in no conclusive proof of whether, $f(y, \Phi_x[k_1,k_2])$, is convex. As a result, it can not be used to determine the convexity of the objective function. Since the convexity of the objective function in (3.32) is not straight forward to determine, the optimization problem is treated as a non-convex optimization problem for both filter configurations.

3.4.2.7 Convexity of the Disjoint Problem

In the disjoint problem, the optimization problem is split into two sub-problems. The first problem is to optimize the capacity with respect to Φ_x given a value for y. The second problem optimizes the capacity with respect to y given Φ_x. Mathematically, the two problems can be expressed by,

- **Problem 1**: Given y

$$\min_{\Phi_x} \quad \frac{-1}{2}\sum_{k_1=0}^{N_1-1}\sum_{k_2=0}^{N_2-1}\log\left(1+\Phi_x[k_1,k_2]\Big/\left[\frac{N_1N_2}{|\rho H[k_1,k_2]|^2}+\right.\right.$$
$$\left.\left. N_1N_2\sigma_q^2\left(y^TA[k_1,k_2]y+t^T[k_1,k_2]y+1\right)\right]\right) \tag{3.35}$$

subject to,

$$\sum \Phi_x[k_1,k_2]=\sigma_x^2\left(N_1N_2\right)^2$$

- **Problem 2**: Given Φ_x,

$$\min_{y} \quad \frac{-1}{2}\sum_{k_1=0}^{N_1-1}\sum_{k_2=0}^{N_2-1}\log\left(1+\Phi_x[k_1,k_2]\Big/\left[\frac{N_1N_2}{|\rho H[k_1,k_2]|^2}+\right.\right.$$
$$\left.\left. N_1N_2\sigma_q^2\left(y^TA[k_1,k_2]y+t^T[k_1,k_2]y+1\right)\right]\right) \tag{3.36}$$

subject to,

$$y^TGy \le \frac{\pi}{\pi-2}$$
$$\beta^Ty \le 1$$

The problem in (3.35) is a convex optimization problem, since the objective function is the weighted sum of the power matrix variables $\Phi_x[k_1,k_2]$. The solution to this problem is given by the water filling algorithm [2, pages 245-246].

In an attempt to study the convexity of the problem in (3.36), the composition rule was used as in Section 3.4.2.6. The first step was to expand the aggregate capacity expression into the sum of the capacity of the individual channels. Composition rule is then applied to the capacity of each individual channel. As mentioned previously, if the argument of the log is concave, then, the aggregate capacity is convex. For the log argument to be concave, its Hessian must be negative semi-definite, that is,

$$\nabla_y^2\left(1+\Phi_x[k_1,k_2]\Big/\left[\frac{N_1N_2}{|\rho H[k_1,k_2]|^2}+ N_1N_2\sigma_q^2\left(y^TA[k_1,k_2]y+t^T[k_1,k_2]y+1\right)\right]\right)\preceq 0 \qquad (3.37)$$

Since the power of each channel $\Phi_x[k_1,k_2]$ is assumed to be given, the Hessian matrix depends solely on the filter coefficient vector y. To show that the Hessian matrix is negative semi-definite, its eigenvalues are computed. For a matrix to be negative semi-difinite its eigenvalues must be non-positive. The eigenvalues of the Hessian of the log argument are computed. These values are found for a fixed frame size with different channel bandwidths. In Figures 3.18, 3.19, 3.20 and 3.21 eigenvalues for the expression in (3.37) are plotted as a function of spatial frequency for a given Φ_x, y, and a channel OTF. For the simulation, the channel OTF is Gaussian shaped with variance equal to σ_H^2 in both dimensions. The average electrical power per channel is equal to $\sigma_x^2 = 0.1$. The filter coefficient $y^T = [0.4, 0.3]$.

Figure 3.18 shows the eigenvalues of the expression in (3.37) for a frame of size 64 × 64 pixels with a channel OTF with variance $\sigma_H^2 = 10$ in both dimensions. The range of eigenvalues shown is, $-0.1 \leq \lambda_1 \leq 2.3611$ and $-1.214 \leq \lambda_2 \leq 0.0098$. Figure 3.19 shows the eigenvalues of the expression in (3.37) for a frame of size 64 × 64 pixels with a channel OTF with variance $\sigma_H^2 = 200$ in both dimensions. The range of eigenvalues shown is, $-3.7231 \leq \lambda_1 \leq 6.9190$ and $-3.1046 \leq \lambda_2 \leq 10.1563$. Figure 3.20 shows the eigenvalues of the expression in (3.37) for a frame of size 64×64 pixels with a channel OTF with variance $\sigma_H^2 = 400$ in both dimensions. The range of eigenvalues shown is, $-412.3328 \leq \lambda_1 \leq 286.6533$ and $-247.9542 \leq \lambda_2 \leq 225.9271$. Figure 3.21 shows the eigenvalues of the expression in (3.37) for a frame of size 64 × 64 pixels with a channel OTF with variance $\sigma_H^2 = 800$ in both dimensions. The

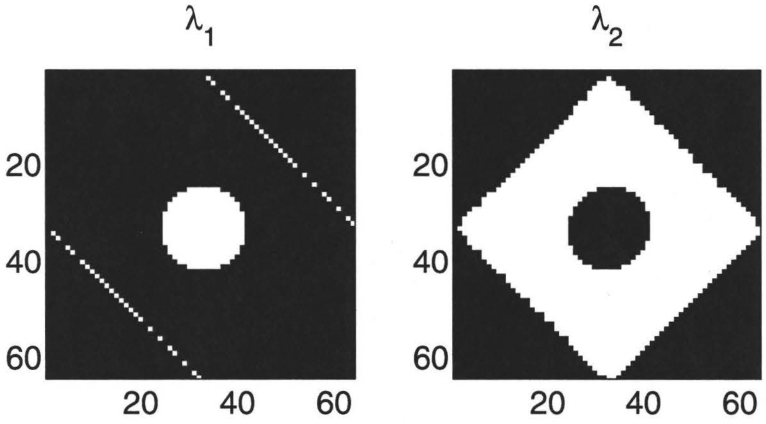

FIGURE 3.18: The two eigenvalues of the Hessian matrix for a frame of size 64 × 64 pixels. The OTF has a Gaussian shape with $\sigma_H^2 = 10$ in both dimensions. The black shaded region shown negative eigenvalues, while the white region shows the positive ones.

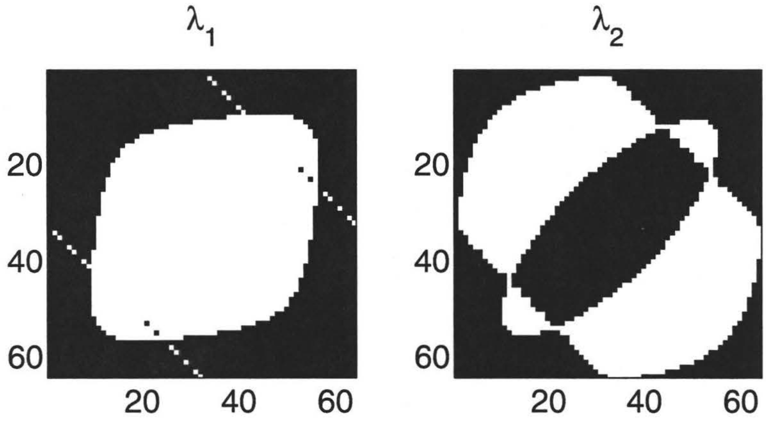

FIGURE 3.19: The two eigenvalues of the Hessian matrix for a frame of size 64 × 64 pixels. The OTF has a Gaussian shape with $\sigma_H^2 = 200$ in both dimensions. The black shaded region shown negative eigenvalues, while the white region shows the positive ones.

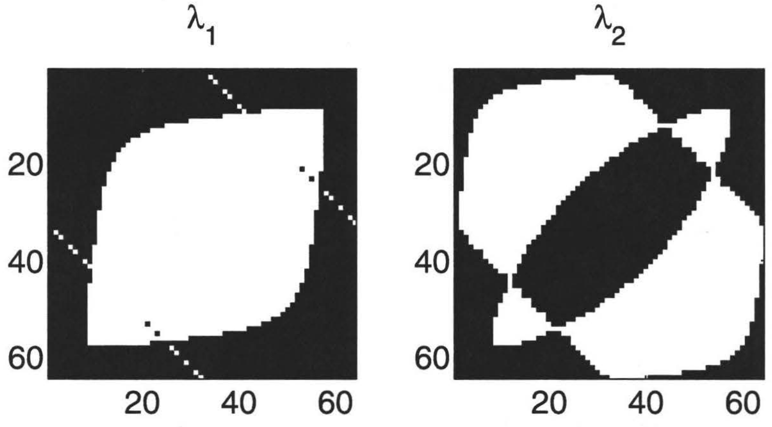

FIGURE 3.20: The two eigenvalues of the Hessian matrix for a frame of size 64 × 64 pixels. The OTF has a Gaussian shape with $\sigma_H^2 = 400$ in both dimensions. The black shaded region shown negative eigenvalues, while the white region shows the positive ones.

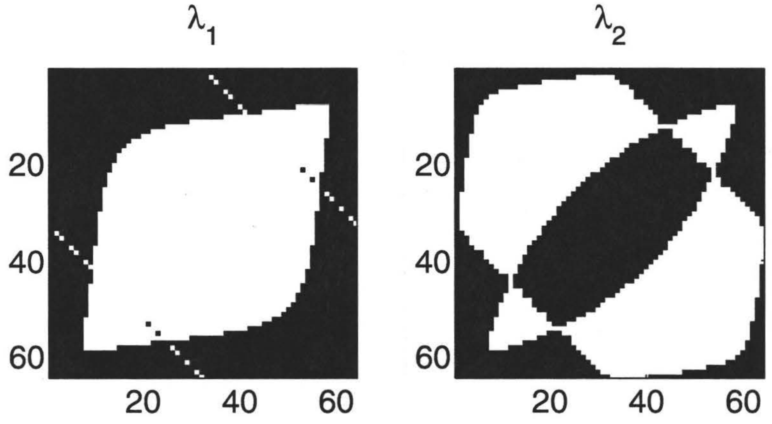

FIGURE 3.21: The two eigenvalues of the Hessian matrix for a frame of size 64 × 64 pixels. The OTF has a Gaussian shape with $\sigma_H^2 = 800$ in both dimensions. The black shaded region shown negative eigenvalues, while the white region shows the positive ones.

range of eigenvalues shown is, $-11354 \leq \lambda_1 \leq 3421$ and $-6437.2 \leq \lambda_2 \leq 2419.1$. From the figures above, notice that the range of eigenvalues changes with the OTF bandwidth. As the bandwidth is decreased (σ_H^2 is decreased), the first eigenvalue λ_1 tends to positive values, while the second eigenvalue λ_2 tends to negative ones. Looking at the eigenvalues, one can say that the Hessian of the log argument in (3.36) is not negative semi-difinite. Consequently, the argument of the log is not concave, hence, the composition rule failed to determine the convexity of the problem. Since the convexity of the objective function is not straight forward to determine, the optimization problem is considered to be a non-convex optimization problem.

In an attempt to determine the non-convexity of the objective function with respect to the filter parameters, the aggregate channel capacity was computed numerically for some points in the feasible region for the first order noise shaping filter. The feasible region is defined by the constraints in (3.36). Figure 3.22 shows the aggregate capacity as a function of the filter parameters for a given OTF bandwidth. In the simulation, the frame size is equal to 64×64 pixels, with an average electrical power $\sigma_x^2 = 0.1$. The channel noise variance is $\sigma_\psi^2 = 10$, and the channel OTF is Gaussian shaped with variance equal to σ_H^2 and is equal in both dimensions.

From Figure 3.22(a), notice that when the channel OTF has a large bandwidth, there are two filter configurations that maximize the aggregate capacity in (3.36). As the bandwidth of the channel is reduced, one of the filter configurations becomes non-optimal and eventually diminishes as in Figure 3.22(d). When the channel has a large bandwidth, its spatial frequency response is almost flat over all spatial frequencies $[k_1, k_2]$. As a result, the noise shaping term, $|1 - J[k_1, k_2]|^2$, shapes the quantization noise either to the edges or to the center of the frame, as shown in Figure 3.23. In such a channel, the aggregate capacity is approximately equal for both filter configurations. As the channel bandwidth is reduced, the channel capacity is maximized when the quantization noise is shaped to the high frequency spectrum of the channel. From

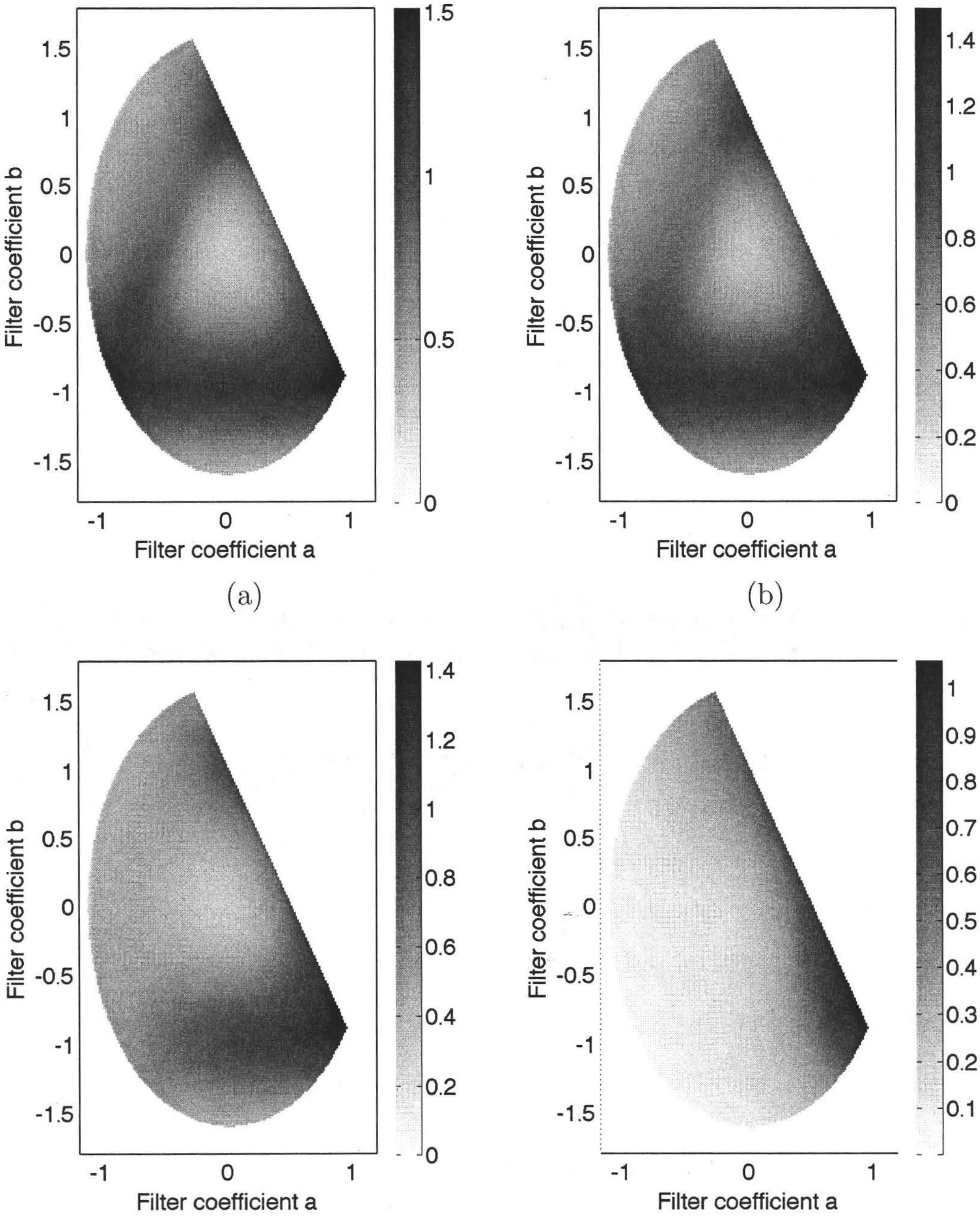

(a) (b) (c) (d)

FIGURE 3.22: The aggregate channel capacity in kbits/frame as a function of the filter parameters for a 2×2 filter topology, for a frame of size 64×64 pixels and a measured channel noise variance of $\sigma_{\psi}^2 = 10$, and an average electrical power $\sigma_x^2 = 0.1$. The channel has a 2D Gaussian shape with a variance σ_H^2 equal in both dimension, (a) $\sigma_H^2 = 800$, (b) $\sigma_H^2 = 400$, (c) $\sigma_H^2 = 200$, (d) $\sigma_H^2 = 50$.

this discussion, it can be deduced that the disjoint problem in (3.36) is in fact a non-convex optimization problem.

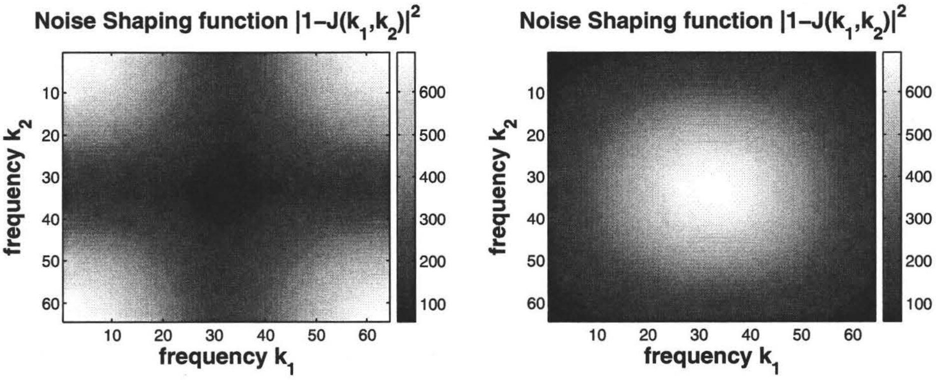

a= 0.9, b= -0.8 a= -0.9, b= -0.8

FIGURE 3.23: The spatial frequency response of the noise shaping term, $|1 - J[k_1, k_2]|^2$, with first order noise shaping. The two filters configurations maximize the channel capacity when the channel OTF has a high bandwidth.

3.4.3 Optimization Algorithm and Results

From previous discussion, it was shown that the joint and disjoint problems are non-convex. Therefore, to solve these problems, sequential quadratic programming is applied. Using such a technique does not guarantee finding a globally optimal solution. To increase the likelihood of obtaining a global optimum the algorithm was computed from many starting points chosen at random from the feasible region.

3.4.3.1 Penalty Function

Since the capacity expression is not defined for filter coefficients outside the feasible region defined by the energy constraint and DC gain constraint, a penalty function is added to push the solution point inside the feasible region. This step is required since the Matlab function, **fmincon**, evaluates the capacity then checks for point

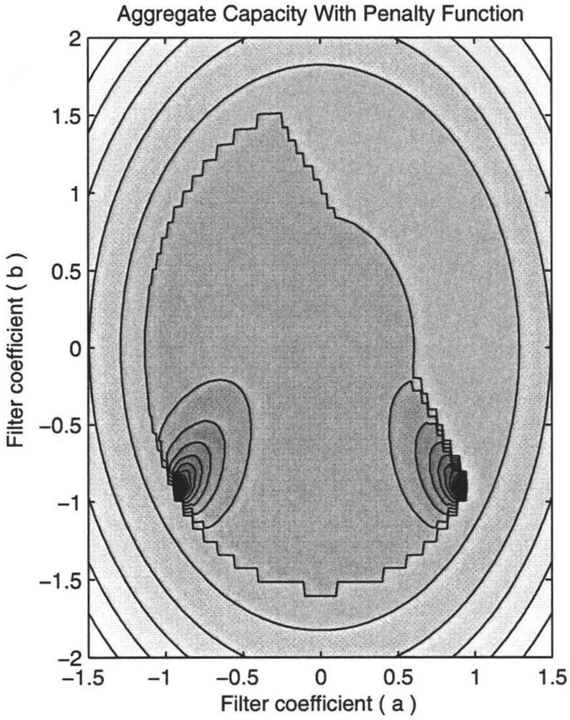

FIGURE 3.24: The aggregate capacity with a penalty function for a 2 × 2 filter topology.

feasibility. The penalty function was defined in such a way as be active if and only if the optimization vector y is infeasible. The penalty function chosen has the following expression,

$$P = \left(y^T G y\right)^4 \tag{3.38}$$

This penalty function represents a hyper bowl that is centered at the origin. Note that this penalty function is not added to the objective function in (3.35) since the objective function in (3.35) is not defined for values of y outside the feasible region. If the optimization vector y was projected to the infeasible region, the slope of the penalty function will project the vector back inside the feasible region were the aggregate capacity is defined. A contour plot of the modified objective function is shown in Figure 3.24.

3.4.3.2 Optimization Problem Starting Point

A good choice for the starting point of an optimization problem is vital for achieving a good solution. This is especially the case for non-convex optimization problems. For the joint problem, a possible starting point would be to choose the power matrix Φ_x to optimize the channel capacity when no quantization noise is present. Other choices for Φ_x might be the optimum power distribution over the channel for each initial filter coefficient vector y.

For the 2×2 filter topology, starting points where selected based on the aggregate capacity figures presented in Section 3.4.2.7. Moreover, 20 points where chosen as to created an equally spaced grid points in the feasible region.

For the 3×3 filter topology, finding good starting points is more challenging since the optimization vector lies in the 5-dimensional space (i.e. y has 5 variables). Some of the starting points were chosen to be local optimal values for the 2×2 filter topology. Moreover, 125 equally spaced starting points where chosen inside the feasible region.

3.4.3.3 Optimization Results

The optimization problem was solved using the constrained nonlinear optimization toolbox in MATLAB [90]. The optimization algorithm was computed for the joint (3.35) and the disjoint (3.36) problems. In the case of joint optimization problem, the lack of the memory resources necessary to solve the system prohibited its numerical implementation. As a result, no results were obtained for the joint optimization problem.

In the case of the disjoint problem, the problem was optimized for different frame sizes and error diffusion filter topologies. To implement the optimization algorithm, three steps where followed:-

Step 1: The power allocation matrix Φ_x was optimized for each increment in y.

Step 2: Given a value for the power allocation matrix Φ_x, the next step in y is evaluated.

Step 3: Steps 1 and 2 are repeated in an iterative fashion. The algorithm is terminated when the change in y is smaller than ϵ, where ϵ is equal to 10^{-4}. The termination of the algorithms signals that a local optimum has been found.

The optimum power allocation in Step 1 was obtained using the water filling algorithm. To obtain a solution, the optimization algorithm ran for different starting points. The local minima were compared for all starting points and channel bandwidths. Filters coefficients where chosen to maximize the frame capacity for all bandwidths. For the first order noise shaping filter, the following optimal filter was obtained,

$$j = \begin{bmatrix} 0 & 0.89 \\ 0.89 & -0.78 \end{bmatrix} \tag{3.39}$$

For the case of second order noise shaping, the following filter was obtained,

$$j = \begin{bmatrix} 0 & 0.94 & -0.18 \\ 0.94 & -0.31 & -0.28 \\ -0.18 & -0.28 & 0.32 \end{bmatrix} \tag{3.40}$$

Note that the filters obtained optimize the aggregate channel capacity for all channel bandwidths. Therefore, they can be implemented in all systems to maximize the capacity. The noise shaping term $|1 - J[k_1, k_2]|^2$ is plotted for both filter configurations. By comparing Figures 3.25 and 3.26 one can see that increasing the filter size results in more degrees of freedom to shape the quantization noise. As a result, one expects an increase in the aggregate channel capacity. From [31] the error diffusion filter was designed using ad-hoc methods. Using simulation, the effects of ad-hoc and optimal designs on the channel capacity where almost similar. For the purpose of simulation, the ad-hoc first order noise shaping filter is used. This filter is equal to,

$$j = \begin{bmatrix} 0 & 0.9 \\ 0.9 & -0.8 \end{bmatrix} \tag{3.41}$$

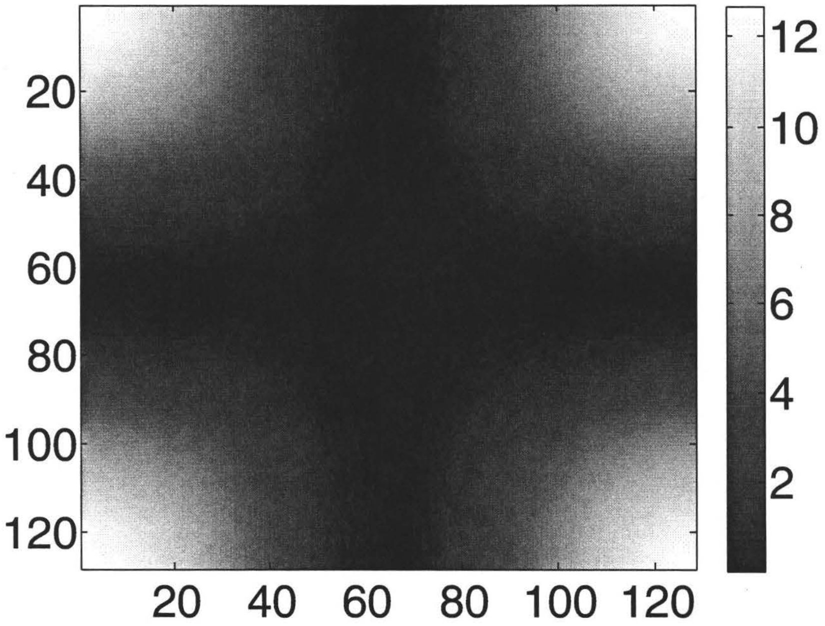

FIGURE 3.25: Noise shaping function $|1 - J[k_1, k_2]|^2$ of the optimal first order noise shaping filter.

3.4.4 Capacity Results and Discussion

The aggregate channel capacity in 3.7 was simulated using the ad-hoc first order and the optimal second order noise shaping filters. For the simulation, experimental channel measurements were used [55], with an average electrical power $\sigma_x^2 = 0.2$.

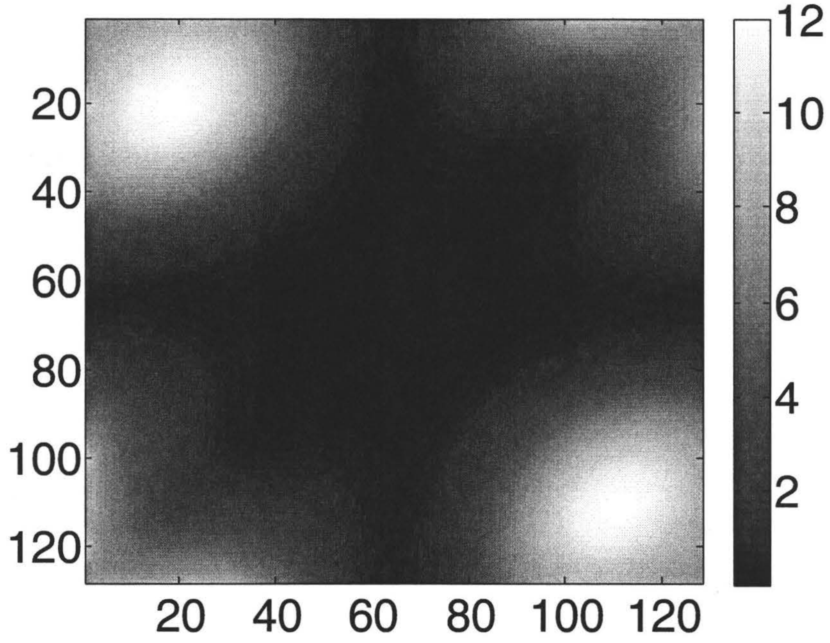

FIGURE 3.26: Noise shaping function $|1 - J[k_1, k_2]|^2$ of the optimal second order noise shaping filter.

The purpose of the simulation is to show the effect of first and second order noise shaping on the capacity of binary and four-level halftoned SDMT systems. Figure 3.27 shows a comparison between first and second order noise shaping for different halftoning levels. Increasing the order of filter yields a modest improvement in the capacity. This increase in capacity depends on the number of halftoning levels. As the number of levels increases, the effect of higher order noise shaping is smaller since less quantization noise is present. That is, the application of higher order noise shaping is limited to systems suffering from high quantization noise power.

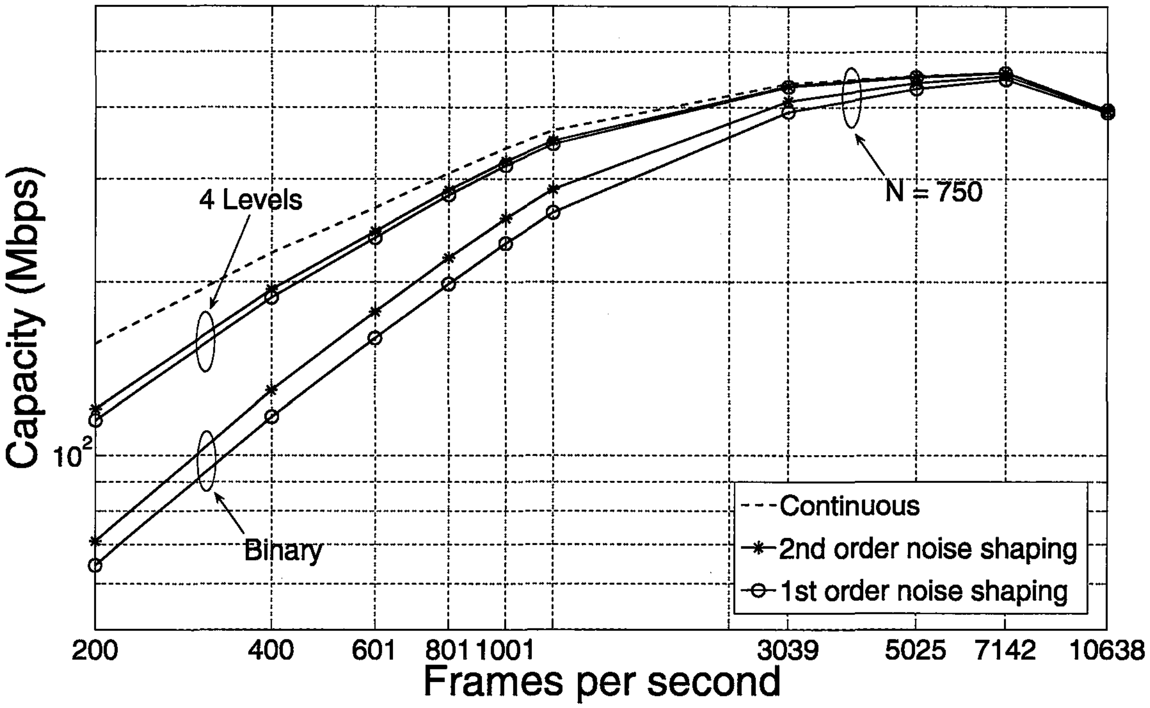

FIGURE 3.27: Comparison between 1^{st} and 2^{nd} order noise shaping for different halftoning levels.

3.5 Conclusion

In this chapter multilevel halftoning and higher order noise shaping are considered for halftoned SDMT systems. Optimal filter design is used to obtain first and second order noise shaping filters that maximize the aggregate channel capacity. From simulation, it was observed that the channel capacity is increased with the number of halftoning levels and the order of the noise shaping filter. Two techniques are proposed for implementing multilevel halftoning. The first techniques uses multilevel SLMs. The second one uses a binary SLM with coding. Based on simulation results, using multilevel halftoning had a greater effect on increasing the channel capacity compared with higher order noise shaping. In the case of higher order noise shaping, gain in capacity was limited to systems with severe quantization noise. Note that the capacities derived are based on theoretical estimates. To achieve these rates in a practical system, coding techniques need to be applied over the channel as in [30].

Chapter 4

Receiver Design for Wireless Optical MIMO Channels with Magnification

4.1 Introduction

In wireless optical MIMO systems, the effects of spatial transformations can severely degrade link performance. These transforms arise from the physical setup of the link, and the optical components used. In some applications, like inter-chip interconnects and holographic data storage, two different techniques have been used to combat the effects of spatial transforms. The first technique rely on machines to align both ends of the link to minimize spatial transforms [50]. The second technique employ signal processing techniques to combat the effects of such transforms on the recovered signal [41–45]. It is important to mention that these two techniques are applicable due to the small magnitude of spatial transforms present in such applications. In a wireless indoor communication application, spatial transformations constitute a major impairment. This is due to the users' imprecise alignment of both ends of the link. Consequently, new design techniques need to be devised to increase the reliability of wireless optical MIMO links in such an application.

In the previous chapter, the wireless optical MIMO transmitter was designed to enhance the channel capacity. Multilevel halftoning and higher order noise shaping were used to simplify the transmitter design, and achieve gains in capacity. In this chapter, the design of the wireless optical MIMO receiver is considered for magnification channels. For the receiver design, it is assumed that the transmitter uses continuous-tone SDMT modulation. A good receiver design is chosen based on minimizing the probability of error of the received data.

Before the receiver design is discussed, an overview of the effects of translation, magnification, and rotation on transmit frames is given. A model encompassing the effects of magnification and rotation is derived. A design framework for the case of magnification is presented. In future work, a similar technique can also be applied for rotation. The design incorporates windowing techniques to equalize the effects of magnification in spatial frequency domain. Two windowing functions are considered, rectangular window and a novel complex window. The application of decision feedback equalization and zero-forcing equalization are considered for detecting the transmit SDMT signal. A heuristic approach for the complex window design is discussed. The chapter concludes with some simulation results.

4.2 Channel Modeling

In wireless optical MIMO channels, the transmit data are often distorted due to spatial transformations. Translation, magnification and rotation are examples of such transformations. In Section 4.2.3, it will be shown that the distortion of the transmit data at the receiver causes spatial frequency inter-channel interference (SF-ICI). Spatial frequency inter-channel interference causes a higher probability of error in detection. In order to develop a greater understanding of the effects of spatial transforms on the SF-ICI, a channel model is needed. In this section, the channel assumptions are stated and justified. A brief discussion regarding the mathematical modeling of spatial transforms is discussed. A model that encompass the effects of spatial transforms on the transmit signal is developed.

4.2.1 Channel Assumptions

The focus of this chapter is to develop detection techniques that can overcome the effects of spatial transforms on the transmit data, thereby, increasing the link reliability by reducing the probability of error in detection. In general, spatial transforms can affect the channel optical transfer function. As a result, it is difficult to evaluate and compare the performance of the proposed detection techniques. In this section, some assumptions are introduced to render the channel response invariant with respect to the spatial transformations studied. Consequently, the different detection techniques are evaluated and compared in a fair manner. For the channel OTF to be transform invariant, the following assumptions are made,

(a) The receive plane is an orthographic projection of the transmit one.

(b) The optics used at both ends of the link are circularly symmetric.

(c) The separation distance between the transmitter and receiver planes is fixed.

(d) The channel noise is dominated by thermal noise, which is modeled as being white, independent and Gaussian.

Figure 4.1 represents an illustration of the assumptions made. To satisfy

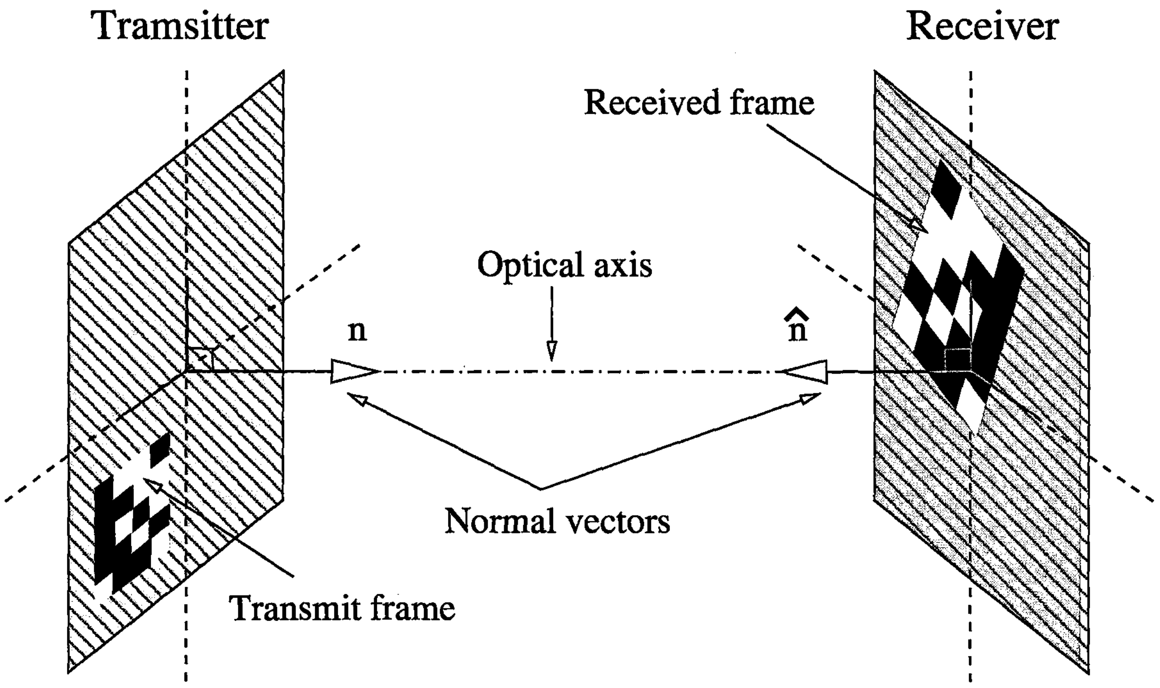

FIGURE 4.1: The system setup for a wireless optical MIMO system.

assumption (a), a normal vector to the receiver plane, $\hat{\mathbf{n}}$, must be equal to the negative of the normal vector of the transmitter plane, $\mathbf{n}$. Mathematically, this condition can be expressed as,

$$\hat{\mathbf{n}} = -\mathbf{n} \tag{4.1}$$

In practice, assumption (a) is satisfied for short range wireless optical MIMO systems, since it is possible to align the transmitter and receiver planes to satisfy the condition in (4.1). Optical interconnects and holographic data storage systems are examples of applications where this assumption is met. Assumption (b), is justified due to the circularly shaped optical components used. A lens is an example of a circularly symmetric optical component. In assumption (c), the separation distance between both ends of the link is fixed. This assumption is always satisfied for the applications considered, since the physical setup of the system is fixed. Assumption (d) states that the channel noise is dominated by electronic thermal noise. This assumption is valid for wireless optical MIMO links operating at high frame rates as discussed in

Section 2.2.4.

From assumption (a), the channel OTF can be modeled as being spatially invariant. Moreover, the channel OTF is circularly symmetric due to the condition imposed in assumption (b). Assumption (c) is most relevant in the case of magnification. In a wireless optical MIMO channel, magnification can be realized in two different methods. In the first method, magnification is realized by keeping the size of the transmit image fixed, and changing the separation distance between both ends of the link. As the distance increases, the projected image at the receiver plane appears smaller. This effect is a direct result of applying geometrical optics theory [61]. In this scenario, the channel OTF is changed due to the physical changes in the link setup. The second method to achieve magnification relies on changing the size of the transmitted images, while keeping the separation distance fixed as in assumption (d). Changes in transmit image size are due to changes in the focal length of transmit optics. Since the OTF is dominated by the response of the receiver optics, changing the focal length of transmit optics while keeping the distance fixed renders the OTF invariant.

Using the stated assumptions, the channel model in (2.1) can be rewritten as,

$$\begin{aligned} x_R[n_1,n_2] &= x_T[\mathcal{T}\{x,y\}_{\substack{x=n_1D_r\\y=n_2D_r}}] \otimes h[n_1,n_2] + \psi[n_1,n_2] && (4.2)\\ x_T[\mathcal{T}\{x,y\}_{\substack{x=n_1D_r\\y=n_2D_r}}] &\geq 0 && (4.3)\end{aligned}$$

where, x_R and x_T are the received and transmitted intensity images respectively, h is the channel PSF, and ψ is the thermal noise. The transformation $\mathcal{T}\{.\}$, signifies the remapping of the coordinates caused by spatial misalignment, magnification and rotation. The two-dimensional discrete convolution is given by $\otimes$, and D_r is the sampling rate at the receiver. From equation (4.2), notice that the channel PSF is transform invariant. The inequality in (4.3) reflects the non-negativity constraint on the transmit signal intensity as in Section 2.2.4. Note that since thermal noise,

$\psi[n_1, n_2]$, is due to the receiver electronics, it is not affected by the magnification and rotation incurred during transmission.

4.2.2 Spatial Transformations

Translation, magnification and rotation are transforms that act on the coordinates of an image to remap their position in space. In this work, the effects of these transforms on the transmit SDMT signal are modeled. To model the effects in spatial frequency domain, it is important to understand the relation between an image and its spectrum as it is transformed. Let (t_1, t_2) denote the coordinates of the continuous spatial domain. Then, the spatial transforms can be modeled as,

$$\begin{bmatrix} \tilde{t}_1 \\ \tilde{t}_2 \end{bmatrix} = \epsilon \begin{bmatrix} \cos\theta & -\sin\theta \\ \sin\theta & \cos\theta \end{bmatrix} \begin{bmatrix} t_1 \\ t_2 \end{bmatrix} + \begin{bmatrix} \Delta_1 \\ \Delta_2 \end{bmatrix} \tag{4.4}$$

where $(\tilde{t}_1, \tilde{t}_2)$ are the remapped image coordinates. The optical magnification is given by ϵ. The angle of rotation is denoted by θ, and $[\Delta_1, \Delta_2]$ denote the translation along the spatial dimensions (t_1, t_2) respectively. Figure 4.2 illustrates the spatial transform in (4.4). To understand the effect of each transform on transmit image, each transform is studied separately.

In the context of wireless optical MIMO channels, translation is often referred to as spatial misalignment. Spatial misalignment is defined as a shift of a transmit image at the receive side. Since images are translated in continuous space, the continuous Fourier transform is used to study the effects of spatial misalignment on the

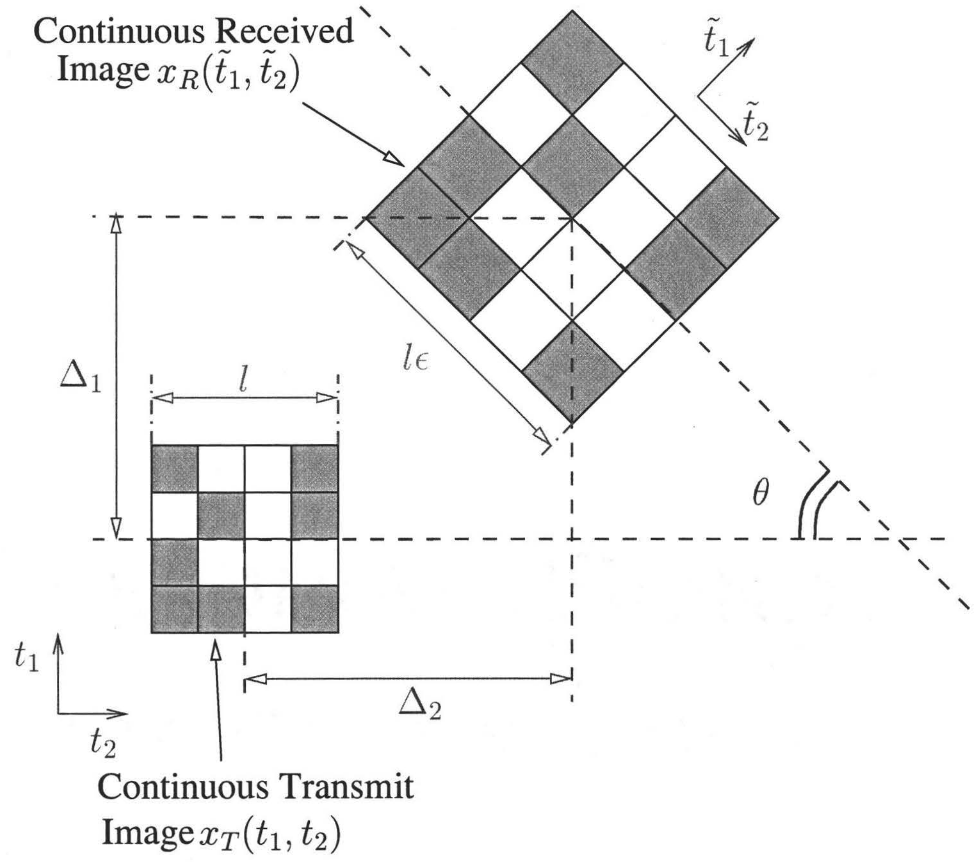

FIGURE 4.2: An illustration of translation, magnification and rotation on spatial images.

image spectrum. Mathematically, spatial misalignment can be described as,

$$\begin{aligned} x_T(t_1, t_2) &\overset{\mathcal{F}}{\rightleftharpoons} X_T(f_1, f_2) \\ &\Downarrow \text{Translation} \\ x_T(t_1 - \Delta_1, t_2 - \Delta_2) &\overset{\mathcal{F}}{\rightleftharpoons} X_T(f_1, f_2) \exp\left(-i2\pi(\Delta_1 f_1 + \Delta_2 f_2)\right) \end{aligned} \tag{4.5}$$

where x_T is the continuous transmit spatial image, and X_T is its spatial frequency spectrum. From (4.5), notice that translating the frame by a fixed amount, $[\Delta_1, \Delta_2]$, causes a linear phase shift in its spatial frequency spectrum. Consequently, the SDMT signal can be easily equalized by a multiplication by a complex exponential. In practice, a measure of the phase shift is incorporated in the channel OTF measurements as discussed in Section 2.4. Since the effects of spatial misalignment is incorporated in the measured OTF, this transform is not considered in the model.

In the case of magnification, increasing the size of the image in space is equivalent to compressing the spatial frequency spectrum. Mathematically this can be expressed as,

$$x(\epsilon t_1, \epsilon t_2) \overset{\mathcal{F}}{\rightleftharpoons} \frac{1}{\epsilon} X\left(\frac{f_1}{\epsilon}, \frac{f_2}{\epsilon}\right) \tag{4.6}$$

As for the spatial rotation of continuous transmit images, a rotation of angle θ in space is equivalent to a rotation of angle $-\theta$ in spatial frequency.

From the discussion above, the effects of magnification and rotation is spatial frequency domain can be mathematically modeled as follows,

$$\begin{bmatrix} \tilde{f}_1 \\ \tilde{f}_2 \end{bmatrix} = \frac{1}{\epsilon} \begin{bmatrix} \cos\theta & \sin\theta \\ -\sin\theta & \cos\theta \end{bmatrix} \begin{bmatrix} f_1 \\ f_2 \end{bmatrix} \tag{4.7}$$

where $(\tilde{f}_1, \tilde{f}_2)$ are the transformed spatial frequency coordinates of the transmit image.

4.2.3 Channel Model

To model the effect of spatial transformations on transmit images, the following assumptions were made. Firstly, the transmitter is a spatial light modulator of size $N_1 \times N_2$ pixels respectively, with pixel spacing equal to D_t in both directions. Secondly, the receiver consists of 2D array of photodetectors of size $M_1 \times M_2$ respectively and a sample spacing equal to D_r in both directions. Thirdly, the spatial frequency spectrum of the transmitter occupies its full Nyquist region of size $1/D_t \times 1/D_t$. Furthermore, the receiver's spatial frequency response is assumed to occupy its full

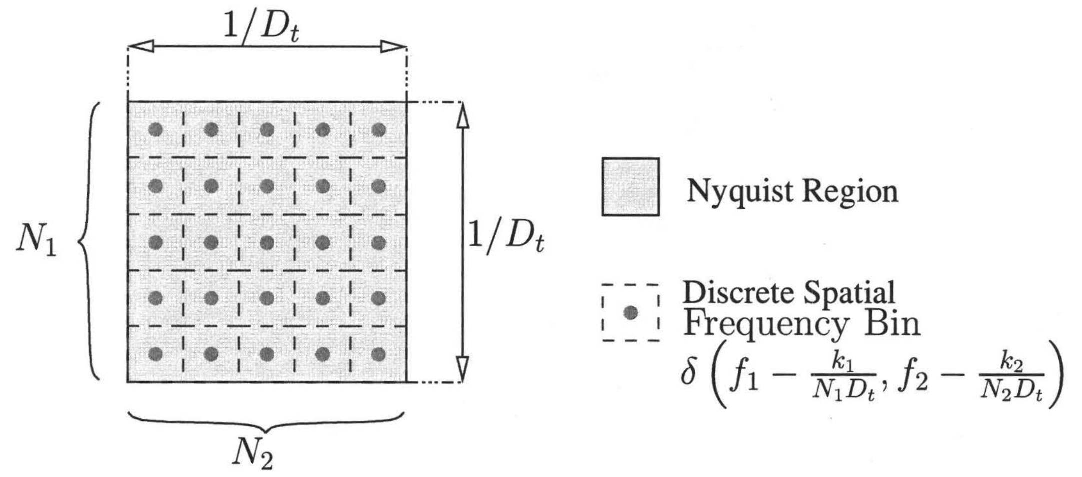

FIGURE 4.3: SDMT modulation divides the Nyquist region of the transmitter into $N_1 \times N_2$ spatial frequency bins. In the model developed, each spatial bin is approximated by a delta function.

Nyquist region of size $1/D_r \times 1/D_r$. The Nyquist region provides a limit on the maximum spatial frequency that can be supported by either side of the link.

From Figure 4.3, notice that in SDMT modulation, the Nyquist region of the transmitter is divided into discrete spatial frequency bins. Each bin corresponds to a single spatial frequency. In each bin, data is loaded in accordance to the channel OTF and noise as in Chapter 2. In continuous frequency domain, the SDMT frequency bins can be represented as shifted delta functions. Let $X_T[k_1, k_2]$ denote the SDMT frame in the discrete spatial frequency coordinates $[k_1, k_2]$. Then, the continuous spectrum of the transmit frame in continuous spatial frequency domain $X_T(f_1, f_2)$ is expressed as,

$$X_T(f_1, f_2) = \frac{1}{N_1 N_2 D_t^2} \sum_{k_1=0}^{N_1-1} \sum_{k_2=0}^{N_2-1} X_T[k_1, k_2] \delta\left(f_1 - \frac{k_1}{N_1 D_t}, f_2 - \frac{k_2}{N_2 D_t}\right) \tag{4.8}$$

Equation (4.8) implies that the transmit image constitute a spatially continuous periodic signal in two-dimensional space. However, due to the rectangular pixel shape of the transmitting device, a transmit image is constant over the pixel extent. In

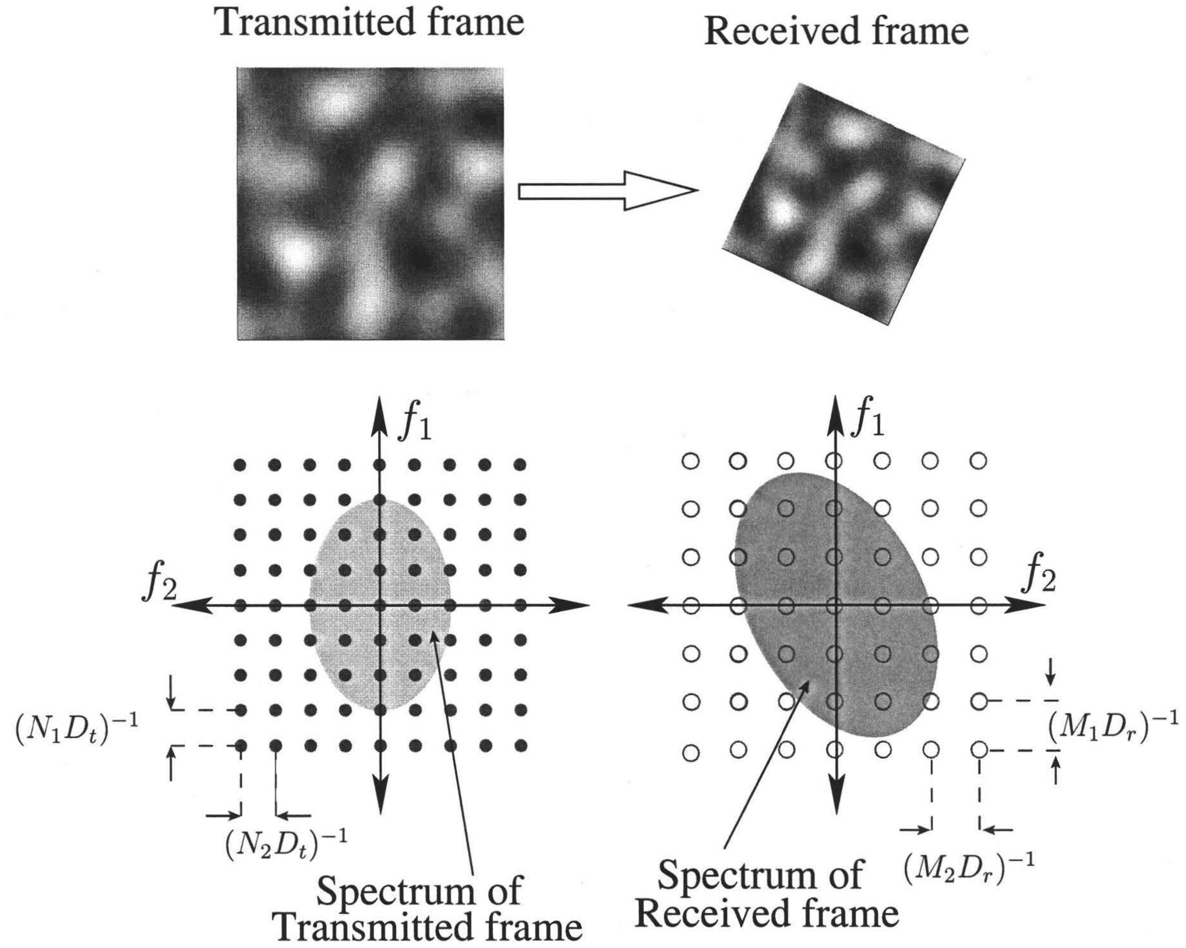

FIGURE 4.4: Transmit images undergo rotation and magnification in space, these transforms correspond the inverse transform in spatial frequency domain.

practice the effect of the pixel shape is coupled with the OTF measurement. As a result, the transmit image can be treated as a continuous waveform in 2D space.

After the spatially continuous transmit image is formed, it is projected onto the photodetector array at the receive side. During the projection process, transmit images undergoes magnification and rotation. Figure 4.4 shows the effects of magnification and rotation on spatial images and their spatial frequency spectrum. From the figure, notice that shrinking the image in space corresponds to expanding its spatial frequency spectrum. Moreover, by rotating the image in space in the clockwise direction, its spatial frequency spectrum is rotated in the counter-clockwise direction by the same amount. To model the effects of spatial transforms at the receive side, (4.7) is applied to the coordinates of the transmit signal in (4.8) as follows,

$$\tilde{X}_T(f_1, f_2) = \frac{1}{N_1 N_2 D_t^2 \epsilon^2} \sum_{k_1=0}^{N_1-1} \sum_{k_2=0}^{N_2-1} X_T[k_1, k_2] \delta\left(f_1 - \nu_1, f_2 - \nu_2\right) \tag{4.9}$$

where ν_1 and ν_2 are equal to

$$\begin{aligned} \nu_1 &= \frac{1}{\epsilon}\left(\frac{k_1 \cos\theta}{N_1 D_t} + \frac{k_2 \sin\theta}{N_2 D_t}\right) && (4.10) \\ \nu_2 &= \frac{1}{\epsilon}\left(-\frac{k_1 \sin\theta}{N_1 D_t} + \frac{k_2 \cos\theta}{N_2 D_t}\right) && (4.11) \end{aligned}$$

and $\tilde{X}_T(f_1, f_2)$ is the spatial frequency spectrum of the transformed spatial frequency spectrum of the transmit image, $X_T(f_1, f_2)$.

At the receive side, it is possible to model the finite extent of the photodetector array by multiplying the transformed signal in the continuous spatial coordinates, $\tilde{x}_T(t_1, t_2)$, by a finite window of size $M_1 D_r \times M_2 D_r$. Since a multiplication in space, corresponds to a convolution in spatial frequency. The spatial frequency spectrum of the received frame can be expressed as,

$$\begin{aligned} X_R(f_1, f_2) &= \tilde{X}_T(f_1, f_2) * W(f_1, f_2) \\ &= \frac{1}{N_1 N_2 D_t^2 \epsilon^2} \sum_{k_1=0}^{N_1-1} \sum_{k_2=0}^{N_2-1} X_T[k_1, k_2] \delta\left(f_1 - \nu_1, f_2 - \nu_2\right) * W(f_1, f_2) \\ &= \frac{1}{N_1 N_2 D_t^2 \epsilon^2} \sum_{k_1=0}^{N_1-1} \sum_{k_2=0}^{N_2-1} X_T[k_1, k_2] W(f_1 - \nu_1, f_2 - \nu_2) && (4.12) \end{aligned}$$

where X_R is the spectrum of the received frame, $*$ is the two-dimensional convolution, and W is the Fourier transform of the finite extent window. After the signal is windowed, it is sampled in spatial domain with a sampling period equal to D_r in both dimensions. To prevent aliasing, it is assumed that the signal is spatially band limited. Moreover, it is assumed that the spectrum of the transformed image is inside the Nyquist region of the receiver. This assumption is true in the case of continuous-tone SDMT modulation, where the signal is limited to the low-band spectrum of the image. Using the above assumptions, the received sampled signal can be written as,

$$X_R[\tilde{k}_1, \tilde{k}_2] = \frac{1}{N_1 N_2 D_t^2 \epsilon^2 M_1 M_2 D_r^2} \sum_{k_1=0}^{N_1-1} \sum_{k_2=0}^{N_2-1} X_T[k_1, k_2] W \left(\frac{\tilde{k}_1}{M_1 D_r} - \nu_1, \frac{\tilde{k}_2}{M_2 D_r} - \nu_2 \right) \tag{4.13}$$

Notice that the received data in, $X_R[\tilde{k}_1, \tilde{k}_2]$, is the weighted sum of all data in the transmit frame, where the weighting factor is given by,

$$\begin{aligned} U[\tilde{k}_1, \tilde{k}_2; k_1, k_2] &= \frac{1}{N_1 N_2 D_t^2 \epsilon^2 M_1 M_2 D_r^2} W \left(\frac{\tilde{k}_1}{M_1 D_r} - \nu_1, \frac{\tilde{k}_2}{M_2 D_r} - \nu_2 \right) \\ &= \frac{1}{N_1 N_2 D_t^2 \epsilon^2 M_1 M_2 D_r^2} W \left(\frac{\tilde{k}_1}{M_1 D_r} - \frac{1}{\epsilon} \left(\frac{k_1 \cos\theta}{N_1 D_t} + \frac{k_2 \sin\theta}{N_2 D_t} \right), \right. \\ &\qquad \left. \frac{\tilde{k}_2}{M_2 D_r} - \frac{1}{\epsilon} \left(-\frac{k_1 \sin\theta}{N_1 D_t} + \frac{k_2 \cos\theta}{N_2 D_t} \right) \right) \end{aligned} \tag{4.14}$$

Using (4.14), equation (4.13) can be rewritten as,

$$X_R[\tilde{k}_1, \tilde{k}_2] = \sum_{k_1=0}^{N_1-1} \sum_{k_2=0}^{N_2-1} X_T[k_1, k_2] U[\tilde{k}_1, \tilde{k}_2; k_1, k_2] \tag{4.15}$$

From (4.15), notice that the receive data in spatial frequency bin $[\tilde{k}_1, \tilde{k}_2]$, is a combination of transmit data in all the discrete spatial frequency bins. This combination function is denoted by U and it is varying in spatial frequency domain. Furthermore, it is a function of the window used, as well as magnification and rotation.

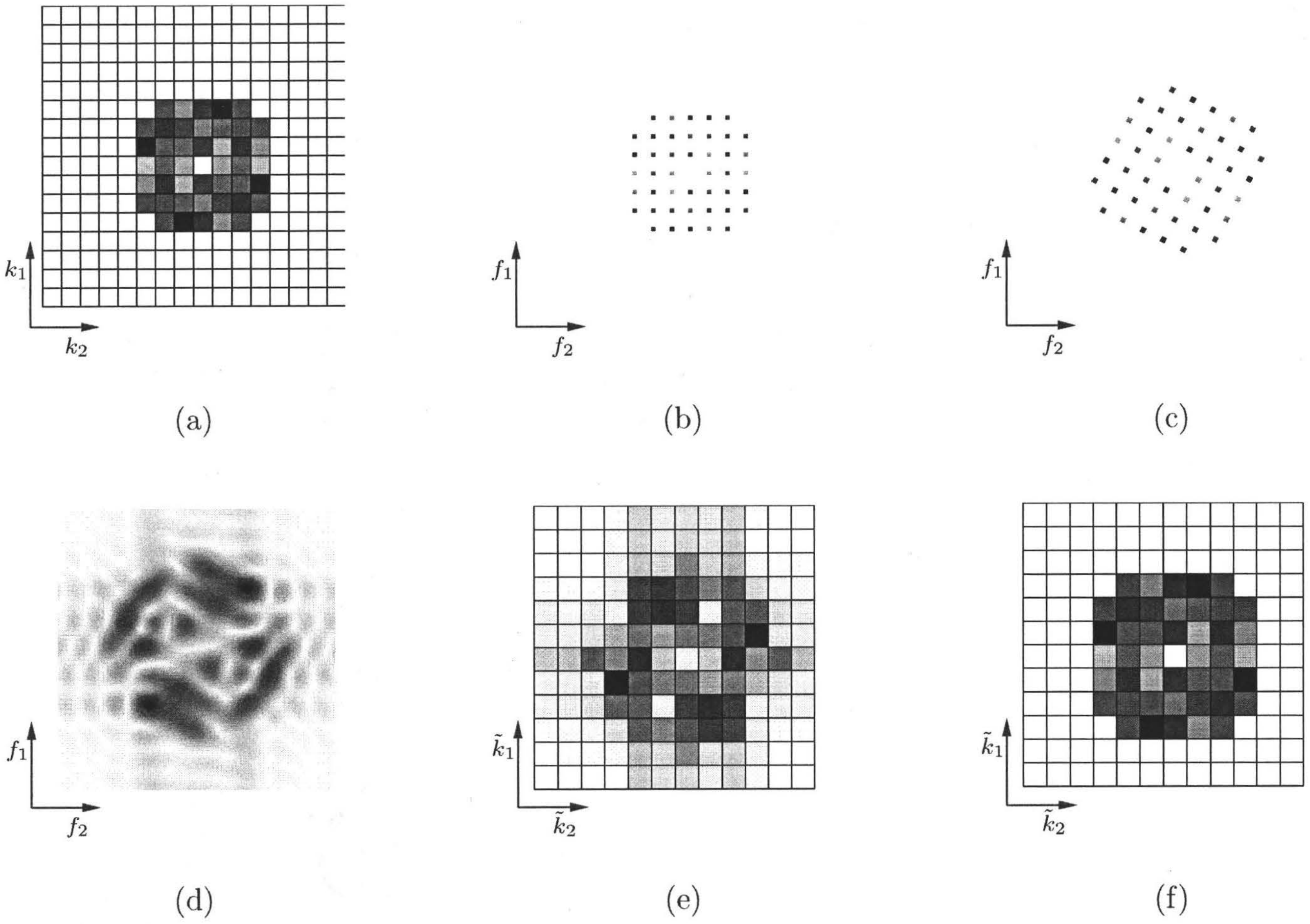

FIGURE 4.5: An illustration of the different stages of a wireless optical MIMO system with magnification and rotation. Figure (a) shows the SDMT modulated data in the discrete spatial frequency bins at the transmitter side, $X_T[k_1, k_2]$, (b) shows the transmit SDMT signal in the continuous spatial frequency domain, $X_T(f_1, f_2)$, (c) shows the magnified and rotated SDMT signal in continuous spatial frequency, $\tilde{X}_T(f_1, f_2)$, (d) illustrates the the spatial frequency spectrum of the windowed transformed signal, $X_R(f_1, f_2)$, (e) illustrates the sampled version of the spatial spectrum of the windowed transformed signal, $X_R[\tilde{k}_1, \tilde{k}_2]$, (f) shows the estimated transmit data at the receive side, $\hat{X}_T[\tilde{k}_1, \tilde{k}_2]$.

Figure 4.5 illustrates the signal at different stages of the wireless optical MIMO system with magnification and rotation. Figure 4.5(a) shows the transmit frame in discrete frequency coordinates, $X_T[k_1, k_2]$. The transmit frame is generated by multiplexing data using continuous-tone SDMT modulation. Since the frame is transmitted in continuous space, the transmit SDMT frame in continuous spatial frequency, $X_T(f_1, f_2)$, can be expressed as a weighted sum of spatial frequency pulses as denoted in (4.8). The resulting signal is as shown in Figure 4.5(b). Relative to the receiver side, transmit images appear magnified and rotated. The spatial frequency spectrum of the transformed transmit frame, $\tilde{X}_T(f_1, f_2)$, is shown in Figure 4.5(c). At the receiver, the spectrum of the magnified transmit image is convolved with the spatial frequency spectrum of the windowing function. The resulting signal, $X_R(f_1, f_2)$, is shown in Figure 4.5(d). The windowed received signal is then sampled as shown in Figure 4.5(e). The sampled signal, $X_R[\tilde{k}_1, \tilde{k}_2]$, is then used to estimate the data in the transmit frame. The estimated frame, $\hat{X}_T[\tilde{k}_1, \tilde{k}_2]$, is shown in Figure 4.5(f).

4.3 Windowing

Windowing is a digital filtering technique commonly used in digital signal processing. In this work, windowing signifies the finite extent of the receiver array. From (4.15), it was shown that the data in each receive spatial frequency bin is a weighted sum of all transmit pixels. Furthermore, the weighing factor was shown to depend on the windowing function used, and the spatial transformation. In this section, an example one-dimensional channel model is considered. This model will illustrate the effect of windowing with magnification on transmit data. Later in the section, the two-dimensional model is considered. In the two-dimensional model, the effects of windowing with magnification and rotation are considered.

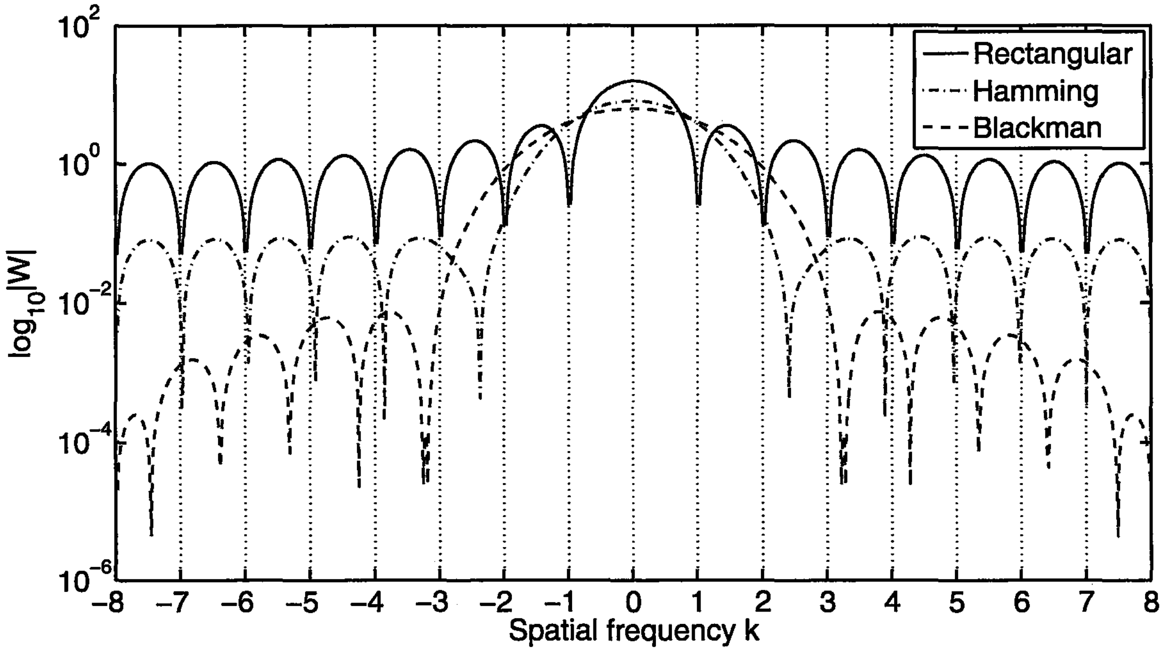

FIGURE 4.6: The frequency response of some commonly used windowing functions, the integer frequencies correspond to the sampled frequencies in spatial frequency domain.

4.3.1 Windowing for One-dimensional Spatial Channels: An Example

Before deriving the magnification model for the one-dimensional spatial channel, the properties of some commonly used windowing functions are studied. It is known that the frequency response of a windowing function is characterized by the width of the main-lobe, and the attenuation of the side-lobes. The main-lobe is defined as the distance between the origin and the first zero crossing on either side of the origin [91, Chapter 7]. Figure 4.6 show the frequency response of some commonly used windows. Notice that there is a trade off between the width of the main-lobe and the attenuation of the side-lobes. The rectangular window has a narrow main-lobe and a low side-lobe attenuation. In contrast, the Blackman window has the wide main-lobe, and a high side-lobe attenuation.

Since multiplying a one-dimensional spatial signal by a window is equivalent to the convolution of their one-dimensional spatial frequency spectrums, windowing a one-dimensional spatial signal causes the smearing of its spatial frequency content. The larger the width of the main-lobe the more smearing there is. From Figure 4.6, notice that the main-lobe of a rectangular window is contained in one spatial frequency sample, as a result the data is not smeared. However, the signal was smeared over many spatial frequency samples for a Blackman window.

To derive a one-dimensional channel model, the transmitter is assumed to be a SLM of size $1 \times N$ pixels with a pixel spacing of D_t. The receiver is a photodiode array of size $1 \times M$ pixels with a sampling interval equal to D_r. Using these assumptions, the received signal can be expressed as follows,

$$X_R[\tilde{k}] = \sum_{k=0}^{N-1} X_T[k]U[\tilde{k};k] \tag{4.16}$$

where

$$U[\tilde{k};k] = \frac{1}{\epsilon NMD_tD_r} W\left(\frac{\tilde{k}}{MD_r} - \frac{k}{\epsilon ND_t}\right) \tag{4.17}$$

In the case of a rectangular window, the factor U is given by,

$$U[\tilde{k};k] = \frac{1}{\epsilon ND_t}\text{sinc}\left(\tilde{k} - k\frac{MD_r}{\epsilon ND_t}\right) \tag{4.18}$$

From (4.16) and (4.18), it can be seen that for an interference free detection, it is required that the following condition is satisfied,

$$U[\tilde{k};k] = \begin{cases} \text{constant} & \tilde{k} = ck, c \in \mathbb{Z}^+ \\ 0 & \text{o.w.} \end{cases} \tag{4.19}$$

The condition above requires the weighing factor to be a spatial nyquist pulse [92]. To satisfy this condition, the following must be true,

$$\frac{MD_r}{\epsilon N D_t} \in \mathbb{Z}^+ \tag{4.20}$$

Notice that in general the condition in (4.20) is not satisfied. As a result, giving rise to spatial frequency inter-channel interference (SF-ICI). To minimize the SF-ICI in (4.18), the value of M is chosen as to approximate one period of the transmit signal, i.e.

$$M = \text{round}\left(\frac{\epsilon N D_t}{D_r}\right)$$

Since M is the approximated signal period, the data in the received frequency bin $\tilde{k}$ is equal to the data in transmit frequency bin k, when $\tilde{k} = k$. This corresponds to setting c in (4.19) to 1. Using this value of M, (4.16) can be rewritten as,

$$X_R[\tilde{k}] = X_T[\tilde{k}]U[\tilde{k};\tilde{k}] + \underbrace{\sum_{\substack{k=0 \\ k\neq\tilde{k}}}^{M-1} X_T[k]U[\tilde{k};k]}_{\text{SF-ICI}} \tag{4.21}$$

In Figure 4.7, the channel response, $U[\tilde{k};k]$, was plotted for a rectangular window as the magnification is changed. From the figure, notice that for a given $\tilde{k}$, the amount of SF-ICI varies with magnification. For unity magnification, the SF-ICI contaminating the signal is zero. However, as the magnification is varied, SF-ICI from all transmit frequency is added to the signal. From this discussion, a rectangular window is the window of choice for systems with unity magnification.

In Figure 4.8, the channel response $U[\tilde{k};k]$ was plotted for a Blackman window as the magnification is varied. Due to the wide main-lobe and the heavily attenuated side-lobes of the window used, the data in received spatial frequency bin $\tilde{k} = 6$ consists of the transmit data at $k = 6$, and its four neighboring bins. The number

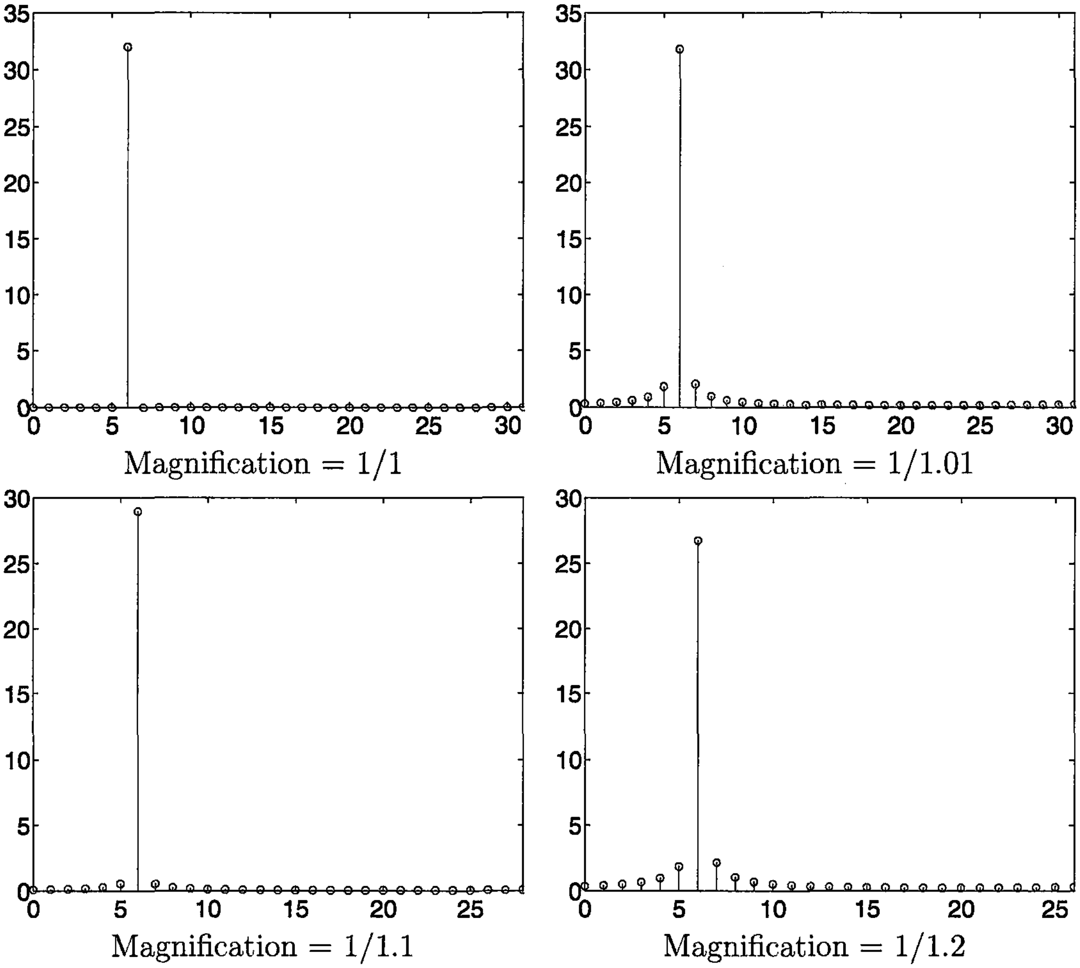

Magnification = 1/1

Magnification = 1/1.01

Magnification = 1/1.1

Magnification = 1/1.2

FIGURE 4.7: A stem plot of the coefficient matrix $|U[\tilde{k};k]|$ for a rectangular window, with $\tilde{k}=6$. Notice that for unity magnification, the received signal at $\tilde{k}=6$ consists only of the transmit data in frequency $k=6$. As the magnification is changed, the received data in $\tilde{k}=6$ is contaminated by the transmit data from all frequency bins, thus, giving rise to SF-ICI.

of neighboring bins remains approximately the same as the magnification is changed, however, the SF-ICI contribution from each spatial frequency bin is changed.

From the discussion above, it was shown that the choice of a windowing function affects the SF-ICI introduced at the receiver. Only for the case of unity magnification is rectangular windowing good, due to its narrow main-lobe. However, for

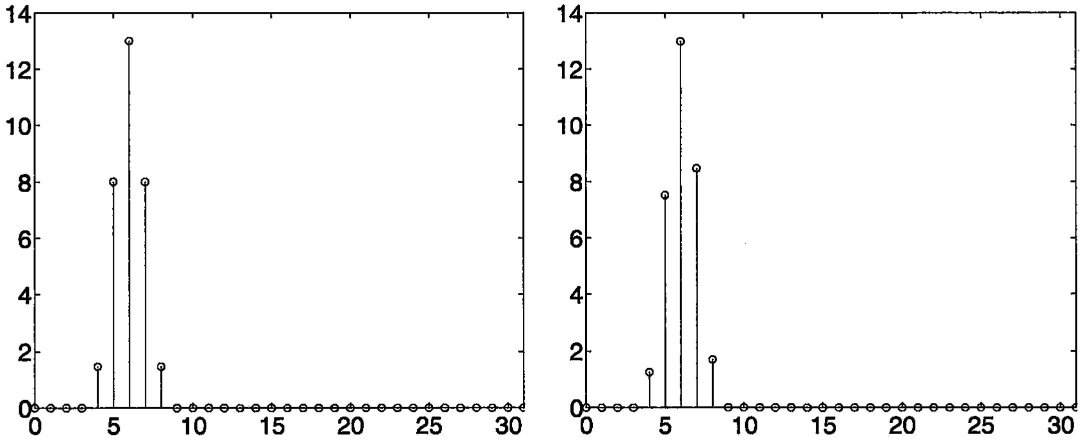

Magnification = 1/1

Magnification = 1/1.01

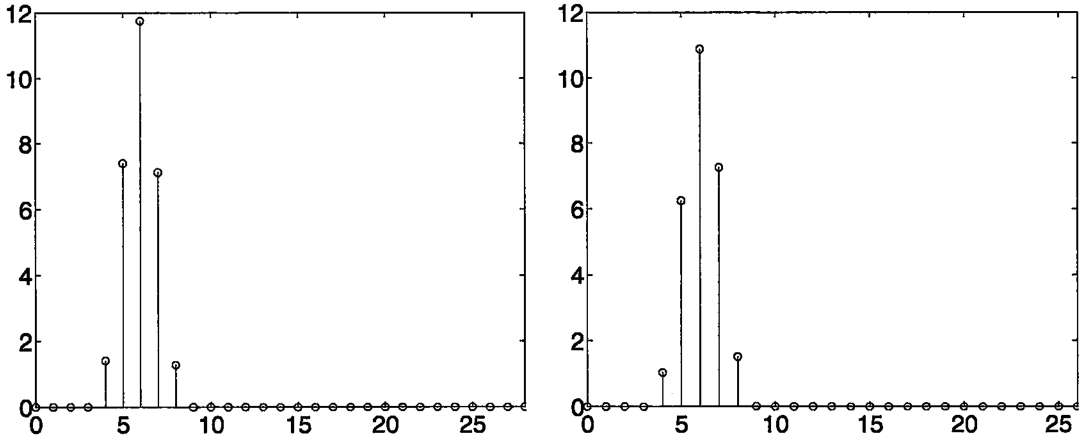

Magnification = 1/1.1

Magnification = 1/1.2

FIGURE 4.8: A stem plot of the coefficient matrix $|U[\tilde{k}; k]|$ for a Blackman window, with $\tilde{k} = 6$. For all magnification values, the received signal in $\tilde{k} = 6$ is a combination of the transmit data in frequency $k = 6$ as well as its four neighboring frequency bins. The extent of the neighboring bins is defined by the width of the main lobe and the attenuation of the side-lobes.

systems that suffer from magnification, the use of a rectangular window can introduce SF-ICI from all frequency bins. This is due to its low side-lobe attenuation. In contrast, the large side-lobe attenuation of a Blackman window limits the SF-ICI to small a band of neighboring frequencies. In Section 4.4.3, windowing is applied in the design of a detection technique that counter the effects of magnification.

4.3.2 Two-dimensional Windowing

To generate a two-dimensional window, a one-dimensional window in the first dimension is multiplied by a one-dimensional window in the second dimension as follows,

$$w_{2D}[m_1, m_2] = w_{1D}[m_1]w_{1D}[m_2]$$

Since the two-dimensional window is separable in terms of its dimensions, the results in Section 4.3.1 can be used to study the effects of windowing combined with magnification and rotation in the two-dimensional system. Note that from now on, the two-dimensional windowing function is referred to by w, and its spatial frequency response is referred to by W.

Assuming that M_1 and M_2 are chosen to minimize the SF-ICI introduced, i.e.

$$M_1 = \text{round}\left(\frac{\epsilon N_1 D_t}{D_r}\right) \in \mathbb{Z}^+ \tag{4.22}$$

$$M_2 = \text{round}\left(\frac{\epsilon N_2 D_t}{D_r}\right) \in \mathbb{Z}^+ \tag{4.23}$$

The equation in (4.15) can be rewritten as,

$$\begin{aligned} X_R[\tilde{k}_1, \tilde{k}_2] &= X_T[\tilde{k}_1, \tilde{k}_2]U[\tilde{k}_1, \tilde{k}_2; \tilde{k}_1, \tilde{k}_2] \\ &+ \underbrace{\sum_{k_1=0}^{M_1-1}\sum_{k_2=0}^{M_2-1} X_T[k_1, k_2]U[\tilde{k}_1, \tilde{k}_2; k_1, k_2]\Lambda[k_1, k_2]}_{\text{SF-ICI}} \end{aligned} \tag{4.24}$$

where,

$$\Lambda[k_1, k_2] = \begin{cases} 0 & k_1 = \tilde{k}_1 \text{ AND } k_2 = \tilde{k}_2 \\ 1 & \text{o.w.} \end{cases} \tag{4.25}$$

From (4.24), the data in the received spatial frequency bin $[\tilde{k}_1, \tilde{k}_2]$, is equal to the transmit signal in the same bin, plus interference terms from other frequencies. As

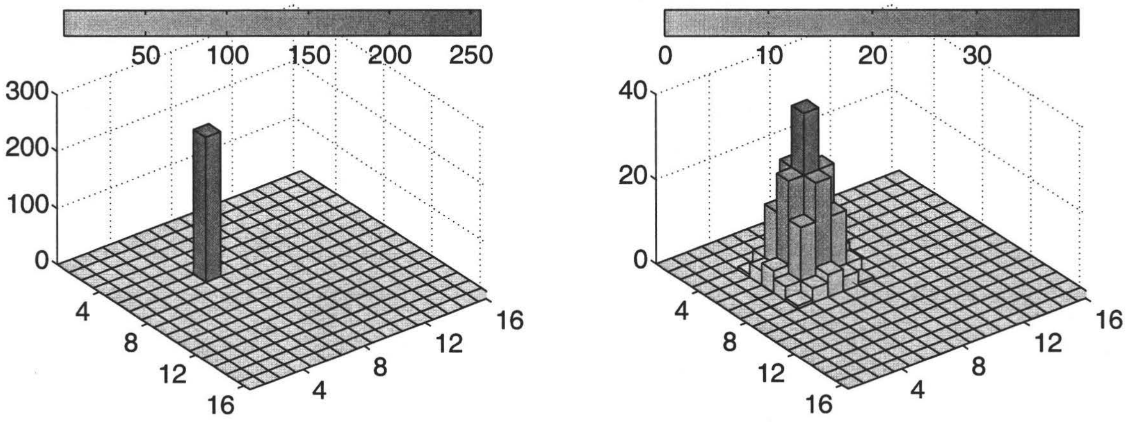

Magnification = 1, Rotation = 0^o Magnification = 1, Rotation = 0^o

FIGURE 4.9: A plot of the absolute value of coefficient matrix, $|U[\tilde{k}_1, \tilde{k}_2; k_1, k_2]|$, when $\tilde{k}_1 = \tilde{k}_2 = 5$. (left) Rectangular window, (Right) Blackman window.

before, the SF-ICI depends on the windowing function used, as well as the spatial transformations. Figures 4.9, 4.10 and 4.11, illustrate the effects of a rectangular window and a Blackman window for different spatial transforms. Notice that the SF-ICI in the case of the rectangular window spans many frequency bins due to its low side-lobe attenuation. In the case of the Blackman window, the SF-ICI is limited in a band of neighboring spatial frequency bins due to the high side-lobe attenuation. From the examples presented, it can clearly be seen that the SF-ICI can be significant in the presence of magnification and rotation.

Note that it is not possible to design a single windowing function that can equalize the SF-ICI in all frequency bins when multiplied with a received frame. This is due to the spatial frequency varying nature of the SF-ICI. In the next section, different equalization schemes are introduced and compared. These schemes rely on windowing and signal processing to equalize the SF-ICI in a manner that is suitable for practical implementation.

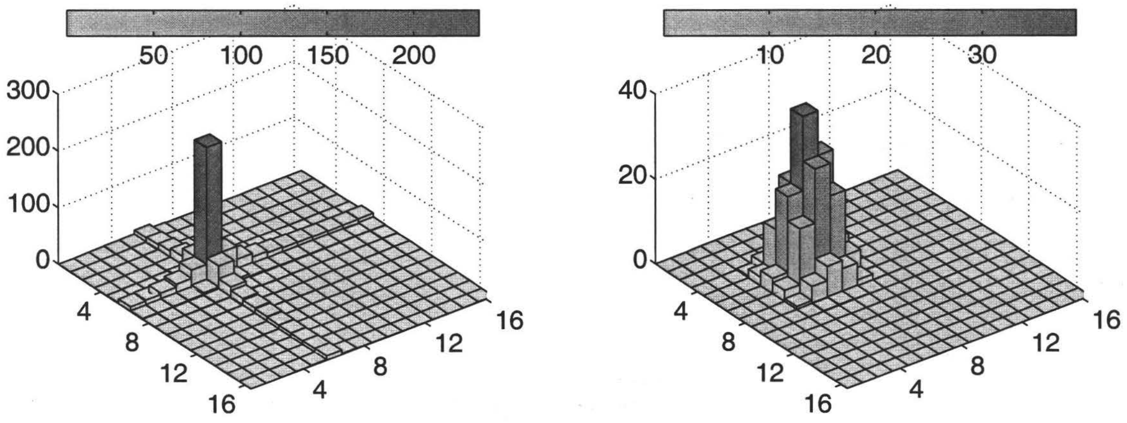

Magnification = 1/1.03, Rotation = 0^o Magnification = 1/1.03, Rotation = 0^o

FIGURE 4.10: A plot of the absolute value of coefficient matrix $|U[\tilde{k}_1, \tilde{k}_2; k_1, k_2]|$ when $\tilde{k}_1 = \tilde{k}_2 = 5$. (left) Rectangular window, (Right) Blackman window.

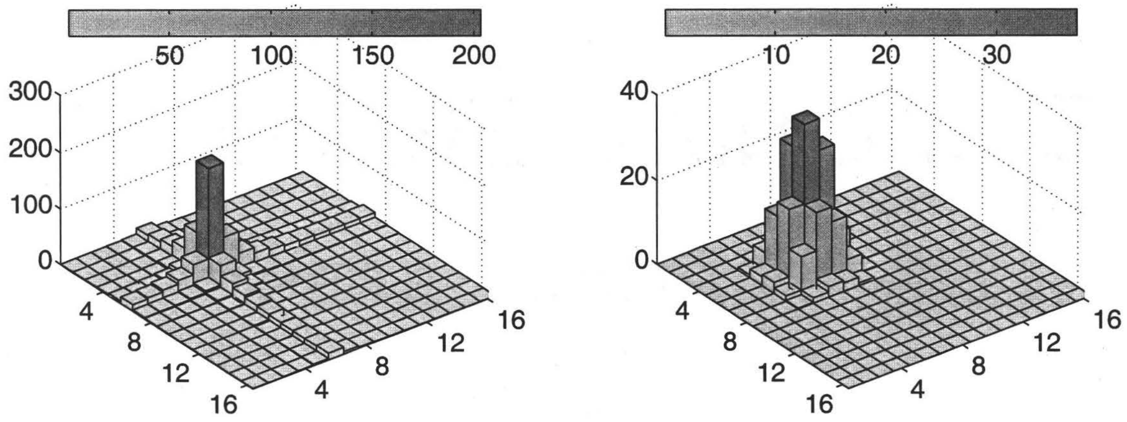

Magnification = 1, Rotation = 3^o Magnification = 1, Rotation = 3^o

FIGURE 4.11: A plot of the absolute value of coefficient matrix $|U[\tilde{k}_1, \tilde{k}_2; k_1, k_2]|$ when $\tilde{k}_1 = \tilde{k}_2 = 5$. (left) Rectangular window, (Right) Blackman window.

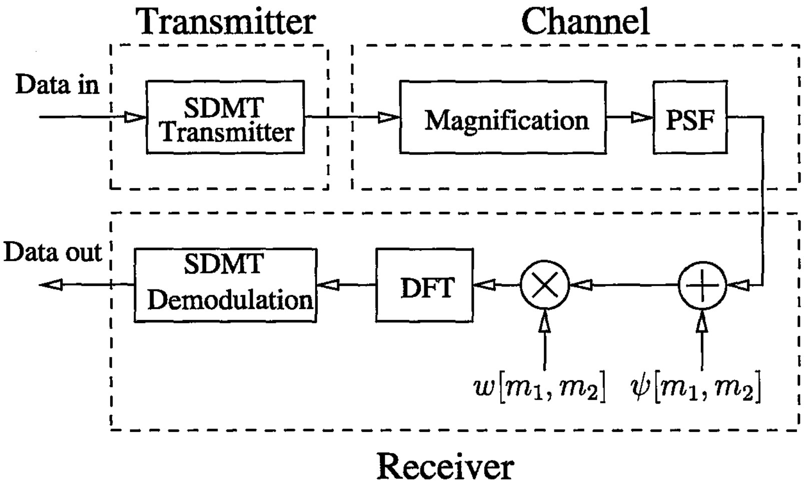

FIGURE 4.12: A block diagram of a wireless optical MIMO communication link with magnification.

4.4 SDMT Demodulation in 2D SF-ICI Channels

In Section 4.2.3, a model was developed to encompass the effects of magnification and rotation on SDMT modulated frames. In this section, the model is applied in the design of a wireless optical MIMO receiver. To simplify the design, it is assumed that the system undergoes magnification only, i.e. the angle of rotation, θ, is set to zero. Note that it is possible to extend the methods developed in this section to consider systems with rotation since magnification and rotation affect the system in a similar manner.

A block diagram of the wireless optical MIMO system considered is given in Figure 4.12. From the figure, the data are multiplexed in the spatial frequency using continuous-tone SDMT modulation. The transmitter forms and projects intensity images corresponding to the modulated data. From the assumptions in Section 4.2.1, transmit images are transformed at the transmitter side since the receiver is the point of reference. Then, the transmitted images are magnified then convolved with the channel PSF. At the receiver, thermal noise ψ is added to the received images. The images are then multiplied in electrical domain by a window. The DFT of the windowed data is computed and the data are demodulated. Mathematically, the received SDMT frame in discrete spatial domain $[\tilde{k}_1, \tilde{k}_2]$ can be expressed as follows,

$$X_R[\tilde{k}_1, \tilde{k}_2] = H[\tilde{k}_1, \tilde{k}_2] \sum_{k_1=0}^{M_1-1} \sum_{k_2=0}^{M_2-1} \left(X_T[k_1, k_2] U[\tilde{k}_1, \tilde{k}_2; k_1, k_2] \right) + \tilde{\Psi}[\tilde{k}_1, \tilde{k}_2] \tag{4.26}$$

where X_R is the received frame, X_T is the transmitted frame, H is the channel OTF, C is a weighing factor given by (4.14), and $\tilde{\Psi}$ is the discrete Fourier transform of the windowed thermal noise. i.e.

$$\tilde{\Psi}[\tilde{k}_1, \tilde{k}_2] = \sum_{m_1=0}^{M_1-1} \sum_{m_2}^{M_2-1} w[m_1, m_2] \psi[m_1, m_2] \exp\left(-i2\pi \left(\frac{m_1 \tilde{k}_1}{M_1} + \frac{m_2 \tilde{k}_2}{M_2} \right) \right),$$

As in (4.24), the equation in (4.26) can be rewritten as,

$$\begin{aligned} X_R[\tilde{k}_1, \tilde{k}_2] &= X_T[\tilde{k}_1, \tilde{k}_2] H[\tilde{k}_1, \tilde{k}_2] U[\tilde{k}_1, \tilde{k}_2; \tilde{k}_1, \tilde{k}_2] \\ &+ \underbrace{H[\tilde{k}_1, \tilde{k}_2] \sum_{k_1=0}^{M_1-1} \sum_{k_2=0}^{M_2-1} X_T[k_1, k_2] U[\tilde{k}_1, \tilde{k}_2; k_1, k_2] \Lambda[k_1, k_2]}_{\text{SF-ICI}} + \tilde{\Psi}[\tilde{k}_1, \tilde{k}_2] \end{aligned} \tag{4.27}$$

From (4.27), the received data symbol equals to the scaled transmit symbol contaminated by SF-ICI and channel noise. Notice also that the SF-ICI introduced is not causal. In this work, causality is defined relative to a decoding path in spatial frequency as shown in Figure 4.13. From Figure 4.13(a), a channel is non-causal if the SF-ICI in the current spatial frequency being decoded, $[\tilde{k}_1, \tilde{k}_2]$, is caused by previous and subsequent spatial frequency bins relative to the decoding path. From Figure 4.13(b-d), a channel is causal if the SF-ICI in the current spatial frequency being decoded, $[\tilde{k}_1, \tilde{k}_2]$, is strictly caused by previously decoded spatial frequency bins relative to the decoding path.

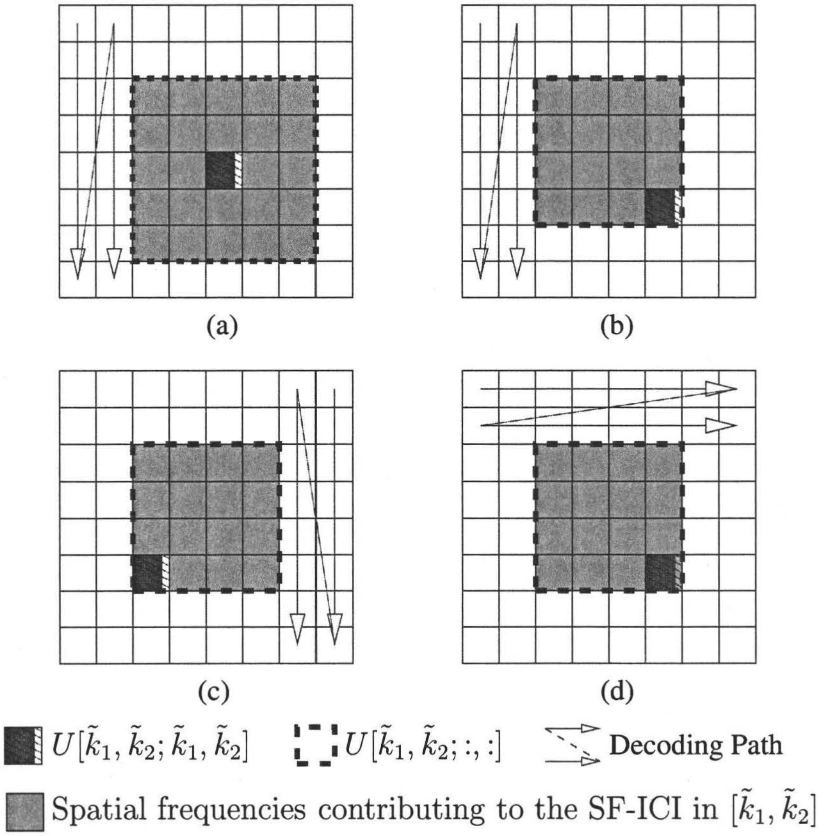

FIGURE 4.13: An illustration of causal and non-causal 2D SF-ICI channels. For a SF-ICI channel, the current frequency denoted by $[\tilde{k}_1, \tilde{k}_2]$ suffer from spatial frequency inter-channel interference from its neighboring bins. Figure (a) illustrates a non-causal system since the interference in the current bin is due to previous and subsequent bins relative to the decoding path. Figures (c-d) illustrate causal systems since the interference in the current bin is strictly from previously decoded bins relative to the decoding path.

Due to the non-causal and the spatially varying nature of the SF-ICI channel, channel equalization is not equalized straight forward. In this section, several equalization techniques are discussed and compared. These techniques focus on the equalization and the demodulation of the received SDMT signal in the presence of SF-ICI.

4.4.1 Joint Equalization

Joint equalization is a well known technique in RF MIMO systems [71, Chapter 10]. This technique is based on solving a system of linear equations. In each equation, the received signal is expressed as a weighted sum of transmit symbols. Solving this system results in the equalization of the ICI introduced by the channel. The equalized signal is then passed through a decision device to determine the constellation symbol transmitted.

In an optical wireless MIMO system, the implementation of joint equalization is expensive in terms of computational and memory resources. This is due to the large number of channels available, and the spatially varying nature of the channel. For example, if the size of the transmit frame is 128 × 128, the system needs to store and solve a linear system of 128^2 variables and a coefficient matrix of size $128^2 \times 128^2$ entries. Consequently, the use of joint equalization in wireless optical MIMO systems is limited.

4.4.2 Zero-Forcing Equalization

In zero-forcing equalization, it is assumed that the contribution of the SF-ICI to the signal is negligible. i.e.

$$\begin{aligned} X_R[\tilde{k}_1,\tilde{k}_2] &= X_T[\tilde{k}_1,\tilde{k}_2]H[\tilde{k}_1,\tilde{k}_2]U[\tilde{k}_1,\tilde{k}_2;\tilde{k}_1,\tilde{k}_2] \\ &+ \underbrace{H[\tilde{k}_1,\tilde{k}_2]\sum_{k_1=0}^{M_1-1}\sum_{k_2=0}^{M_2-1} X_T[k_1,k_2]U[\tilde{k}_1,\tilde{k}_2;k_1,k_2]\Lambda[k_1,k_2]}_{\text{SF}-\text{ICI}\approx 0} + \tilde{\Psi}[\tilde{k}_1,\tilde{k}_2] \end{aligned} \tag{4.28}$$

This assumption is valid if the effect of magnification is small or the channel is dominated by noise. In this technique, a rectangular window is used to filter the signal.

Consequently, most of the signal energy is concentrated in one frequency bin. Using this techniques, the received signal in (4.28) can be approximated by,

$$X_R[\tilde{k}_1, \tilde{k}_2] \approx X_T[\tilde{k}_1, \tilde{k}_2] H[\tilde{k}_1, \tilde{k}_2] U[\tilde{k}_1, \tilde{k}_2; \tilde{k}_1, \tilde{k}_2] + \tilde{\Psi}[\tilde{k}_1, \tilde{k}_2] \tag{4.29}$$

From (4.29), the equalization process is reduced to a division by a constant. The equalized signal is then passed though a decision device to estimate the transmit signal as follows,

$$\hat{X}_T[\tilde{k}_1, \tilde{k}_2] = \mathcal{D}^{-1}\left\{ \frac{X_R[\tilde{k}_1, \tilde{k}_2]}{H[\tilde{k}_1, \tilde{k}_2] U[\tilde{k}_1, \tilde{k}_2; \tilde{k}_1, \tilde{k}_2]} \right\} \tag{4.30}$$

where $\hat{X}_T$ is the estimated transmit signal at the receive side, and $\mathcal{D}^{-1}\{.\}$ is a function that de-maps the equalized data into a constellation symbol. The de-mapping is performed by a decision device implemented as a maximum likelihood detector, where the estimated transmit data is chosen to minimize the probability of symbol error. Since the wireless optical MIMO channel consists of a number of sub-channels in spatial frequency domain, each of which is modeled as an additive white and Gaussian noise channel, the maximum likelihood detector is the optimal detector for each spatial frequency sub-channel [69, Chapter 5].

4.4.3 Decision Feedback Equalization

Due to the finite size of the receiver, the wireless optical MIMO channel is seen as a SF-ICI channel as explained in Section 4.4. As a result, a decision feedback equalizer (DFE) can be used to equalize the received SDMT signal in spatial frequency domain. The use of a DFE in the 2D SF-ICI channel considered is not straight forward since the channel is non-causal, and spatial frequency varying. To develop further insight into the application of DFE in the 2D SF-ICI channel, the DFE is applied to the one-dimensional spatial frequency channel as an example. In Section 4.4.3.2, the results from the one-dimensional spatial frequency channel are extended to the two-dimensional case.

4.4.3.1 Decision Feedback Equalization for the 1D SF-ICI Channel: An Example

In the presence of noise, the one-dimensional spatial frequency ICI channel in (4.21), can be rewritten as follows,

$$\begin{aligned} X_R[\tilde{k}] &= X_T[\tilde{k}]H[\tilde{k}]U[\tilde{k};\tilde{k}] + \underbrace{\sum_{k=0}^{\tilde{k}-1} X_T[k]H[\tilde{k}]U[\tilde{k};k]}_{\text{precursor SF}-\text{ICI}} \\ &\quad + \underbrace{\sum_{k=\tilde{k}+1}^{M-1} X_T[k]H[\tilde{k}]U[\tilde{k};k]}_{\text{postcursor SF}-\text{ICI}} + \tilde{\Psi}[\tilde{k}] \end{aligned} \tag{4.31}$$

where the precursor SF-ICI refers to the **interference of previous spatial frequency bins** on the current spatial frequency bin, while the postcursor SF-ICI pertains to the **interference of subsequent spatial frequency bins**. For the 1D channel in (4.31), causality is defined relative to a decoding path in the direction of increasing $\tilde{k}$. Figure 4.14 shows the post/pre cursor SF-ICI relative to the decoding path in spatial frequency.

Figure 4.15 show a block diagram of a decision feedback equalizer. Notice that a DFE consists of three main sections, the feedforward section, the feedback section, and a decision device. The purpose of the feedforward section is to equalize the postcursor SF-ICI, while, the feedback section is used to equalize the precursor SF-ICI.

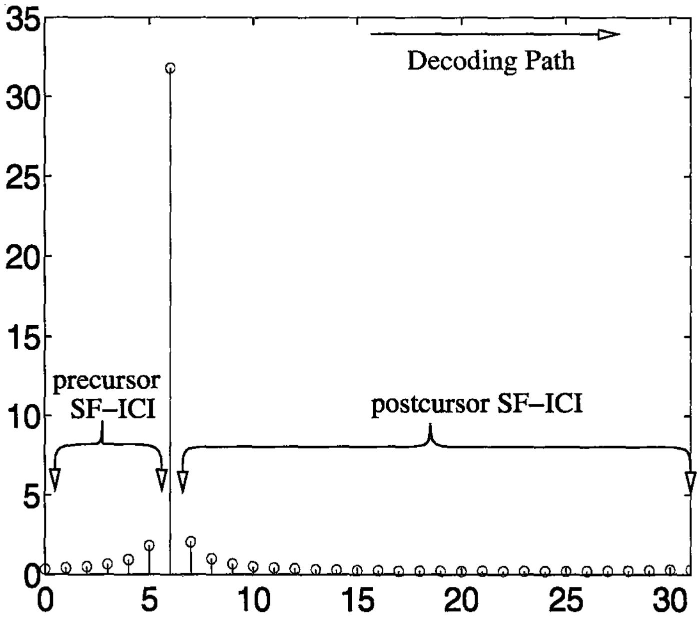

FIGURE 4.14: Precursor and Postcursor SF-ICI.

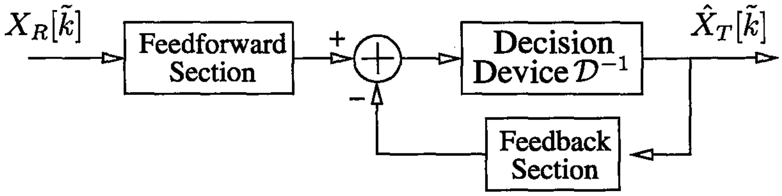

FIGURE 4.15: A block diagram of a decision feedback equalizer.

For the one-dimensional channel considered, windowing the received signal is analogous to feedforward equalization in the sense that it limits the extent of the postcursor SF-ICI, i.e. make the SF-ICI causal with respect to the decoding direction. Referring back to Figure 4.7 and Figure 4.8, notice that in the case of a rectangular window the postcursor SF-ICI spans many frequency bins. On the other hand, by using a Blackman window, most of the postcursor SF-ICI was equalized.

Since the ICI in the windowed signal is limited to a small number of frequency bins, the received signal in (4.31) can be approximated by,

$$\begin{aligned} X_R[\tilde{k}] \approx\ & X_T[\tilde{k}]H[\tilde{k}]U[\tilde{k};\tilde{k}] + \underbrace{H[\tilde{k}] \sum_{k=\tilde{k}-\tau_L}^{\tilde{k}-1} X_T[k]U[\tilde{k};k]}_{\text{precursor SF-ICI}} \\ & + \underbrace{H[\tilde{k}] \sum_{k=\tilde{k}+1}^{\tilde{k}+\tau_H} X_T[k]U[\tilde{k};k]}_{\text{postcursor SF-ICI}} + \tilde{\Psi}[\tilde{k}] \end{aligned} \tag{4.32}$$

where τ_L and τ_H define the width of the frequency band around the desired frequency $\tilde{k}$ where most of the energy is concentrated. In the case of a Blackman window τ_L and τ_H are equal to 2, as can be seen from Figure 4.8. From the approximation in (4.32), notice that the transmit data in frequency bin $\tilde{k}$ can not be estimated from the received data in the corresponding bin due to non-zero postcursor SF-ICI. By exploiting the properties of the transmit signal, the finite extent of the postcursor SF-ICI it is possible to write the detection problem as follows,

$$\hat{X}_T[\tilde{k}+\tau_H] = \mathcal{D}^{-1}\left\{ \frac{X_R[\tilde{k}] - H[\tilde{k}]\sum_{k=\tilde{k}-\tau_L}^{\tilde{k}+\tau_H-1} \hat{X}_T[k]U[\tilde{k};k]}{H[\tilde{k}]U[\tilde{k};\tilde{k}+\tau_H]} \right\} \tag{4.33}$$

where $\hat{X}_T$ is the estimated transmit data, and $\mathcal{D}^{-1}\{.\}$ is a function that de-maps the equalized data into a constellation symbol. The de-mapping is performed using a maximum likelihood detector, where the estimated transmit data is chosen to minimize the probability of symbol error. From (4.33), the data in a subsequent spatial frequency bin, $\hat{X}_T[\tilde{k}+\tau_H]$, is estimated based on observing its effect on the received data in current spatial frequency bin, $X_R[\tilde{k}]$. Notice that a shift was introduced to make the SF-ICI causal with respect to the decoding path. In order to estimate $\hat{X}_T[\tilde{k}+\tau_H]$ from $X_R[\tilde{k}]$, the SF-ICI introduced by the preceding transmit frequency bins is removed using their previously estimated values from the received data $X_R[\tilde{k}]$, then passing the equalized data though the decision device $\mathcal{D}^{-1}\{.\}$.

In order for this technique to work, $\hat{X}_T$ must be known for all values preceding the desired bin. To satisfy this condition, the structure of transmit signal is exploited. From Chapter 2, it is known that for a 2D continuous-tone SDMT signal, the data is loaded in the low-band frequency spectrum, while zeros are transmitted in the high-band spectrum. For one-dimensional system, SDMT modulation can be applied in the same manner, i.e. data to be transmitted is loaded in the low-pass spectrum, while zeros are transmitted in the high-band spatial frequency spectrum. Since the transmit signal in the high frequency is known, the DFE algorithm can be started from the high-frequency bins and ending at DC. Figure 4.16 shows the application of the DFE described in (4.33) to a one-dimensional SDMT signal.

From the previous equations, notice that the windowing function used, can greatly affect the performance of the decision feedback equalizer. To achieve a high performance, in terms of low probability of error, the following design criteria can be deduced :

(a) From (4.33) it was shown that the transmit signal in spatial frequency bin $[\tilde{k} + \tau_H]$ is estimated from its SF-ICI contribution in the current frequency bin $[\tilde{k}]$. To develop an understanding of how this process affects the probability of error, a measure of the signal interference to the noise ratio (SINR) is defined as follows,

$$\mathrm{SINR}[\tilde{k}] = \frac{|H[\tilde{k}]U[\tilde{k}; \tilde{k} + \tau_H]|^2 \sigma^2_{\tilde{k}+\tau_H}}{\sigma^2_{\tilde{\Psi}}[\tilde{k}]} \tag{4.34}$$

where $\sigma^2_{\tilde{k}+\tau_H}$ is the power of the signal to be estimated, $|H[\tilde{k}]U[\tilde{k}; \tilde{k} + \tau_H]|^2$ is a scaling factor reflecting the interference of the data to be estimated in the current frequency bin $[\tilde{k}]$, and the denominator represents the noise power. Equation (4.34), represents a measure of the signal interference power used to estimate the data in spatial frequency bin $[\tilde{k} + \tau_H]$, relative to the channel noise

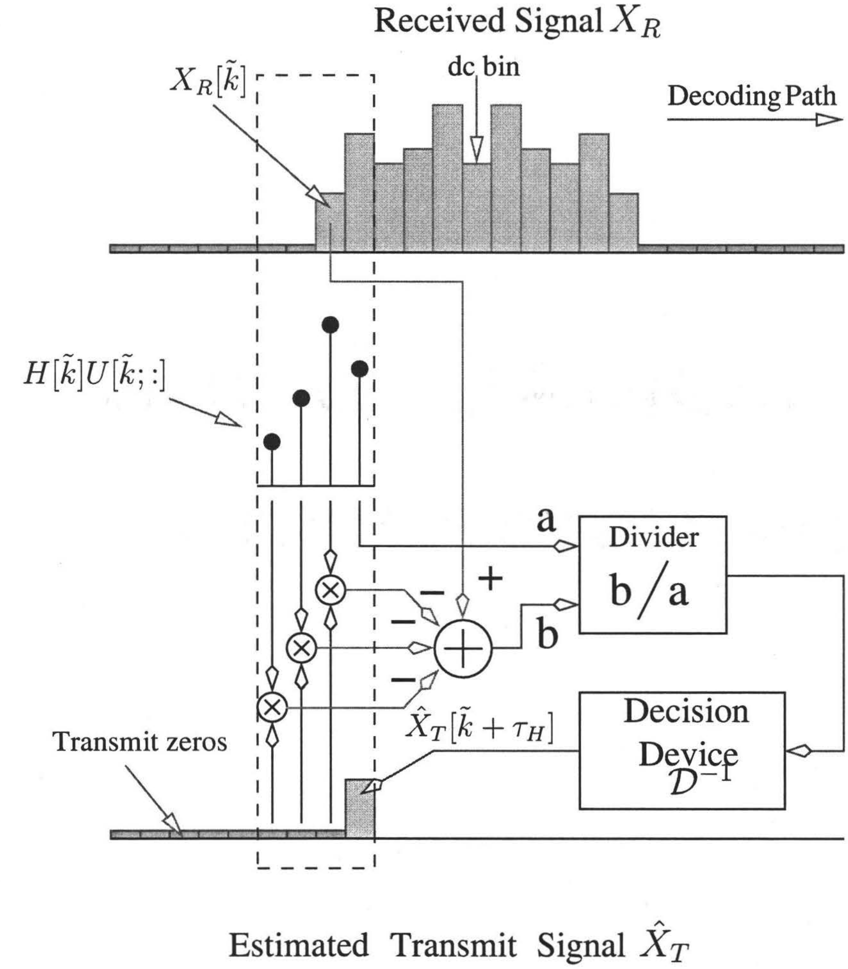

FIGURE 4.16: An illustration of a decision feedback equalization for one-dimensional SDMT signal as described in equation (4.33). In this illustration $\tau_L = 2$ and $\tau_H = 1$.

power in the current frequency bin $[\tilde{k}]$. This ratio directly affects the probability of error. If the signal interference power is large relative to the noise power, i.e. SINR is high, then the probability of erroneous detection is low since there is low ambiguity when decoding the signal. However, if the signal interference power is small relative to the noise power, i.e. the SINR is low, the probability of error is high due to the high ambiguity when decoding the signal. From (4.34), notice that the SINR is directly affected by the design of the window. Therefore, this condition can be used to design a windowing function that achieves a low probability of error.

(b) The implementation of decision feedback equalization is based on approximating the receive signal as in (4.32). Assume that, $\Omega_{\tilde{k}}$, is the set of all frequency bins used in equalization, i.e. $\{\tilde{k}-\tau_L,\dots,\tilde{k}+\tau_H\} \in \Omega_{\tilde{k}}$. Then, the received signal can be expressed as,

$$X_R[\tilde{k}] = \underbrace{H[\tilde{k}]\sum_{k\in\Omega_{\tilde{k}}} X_T[k]U[\tilde{k};k]}_{\text{Used in DFE}} + \underbrace{H[\tilde{k}]\sum_{k\notin\Omega_{\tilde{k}}} X_T[k]U[\tilde{k};k]}_{\text{Not used in DFE}} + \tilde{\Psi}[\tilde{k}] \tag{4.35}$$

From (4.33) and (4.35), it can be shown that the decision feedback equalizer does not equalize the interference from bins that are not used in the approximation. To study the impact of the approximation on the probability of error, a measure of the Feedback to Total Energy Ratio is defined as follows,

$$\mathrm{FTER}[\tilde{k}] = \frac{\sum_{k\in\Omega_{\tilde{k}}} |H[\tilde{k}]U[\tilde{k};k]|^2}{\sum_{k=0}^{M-1} |H[\tilde{k}]U[\tilde{k};k]|^2} \tag{4.36}$$

To reduce this interference, a designed window should have high attenuation for frequencies not used in the DFE, or equivalently, most of the feedback window energy must be used in detection. Mathematically, this condition can be expressed as follow,

$$\mathrm{FTER}[\tilde{k}] = 1-\gamma, \qquad ,\forall\tilde{k} \tag{4.37}$$

where γ is chosen to be small. From (4.36) and (4.37), a good window design results in most of the energy of the weighing factor $H[\tilde{k}]U[\tilde{k};k]$ be inside the region $\tilde{k}-\tau_L \le k \le \tilde{k}-\tau_L$, for all frequency bins $\tilde{k}$. If this condition is satisfied, then the undesired SF-ICI is fully equalized, thus reducing the probability of error when decoding the signal.

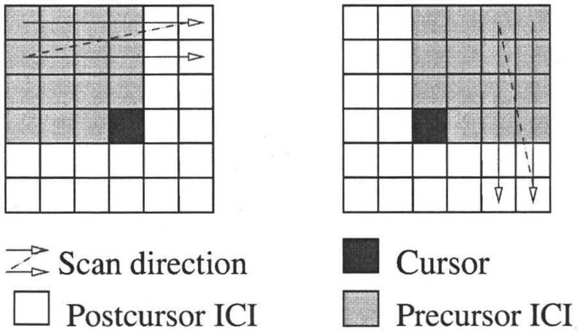

FIGURE 4.17: Precursor and postcursor spatial frequency inter-channel interference for two-dimensional interference channels. Notice that pre/post-cursor SF-ICI can only be defined relative to a decoding path.

4.4.3.2 Decision Feedback Equalization for the 2D SF-ICI Channel

In Section 4.4.3.1, windowing was used to implement decision feedback equalization in the one-dimensional channel. In this section, the same concept is extended to the two-dimensional SF-ICI channel. For the 2D SF-ICI channel, precursor and postcursor SF-ICI are defined with respect to predefined path as shown in Figure 4.17.

By multiplying the received signal with a windowing function, the data in each received frequency bin can be approximated as follows,

$$X_R[\tilde{k}_1, \tilde{k}_2] \approx H[\tilde{k}_1, \tilde{k}_2] \sum_{k_1=\tilde{k}_1-\tau_{L1}}^{\tilde{k}_1+\tau_{H1}} \sum_{k_2=\tilde{k}_2-\tau_{L2}}^{\tilde{k}_2+\tau_{H2}} X_T[k_1, k_2] U[\tilde{k}_1, \tilde{k}_2; k_1, k_2] + \tilde{\Psi}_{[}\tilde{k}_1, \tilde{k}_2] \tag{4.38}$$

Equation (4.38) implies that by choosing a window with high side-lobe attenuation, as in Figure 4.10, the interference in each frequency bin $[\tilde{k}_1, \tilde{k}_2]$ can be ascribed to its neighboring bins. The extent of the neighboring bins is defined by the parameters $[\tau_{L1}, \tau_{H1}]$ and $[\tau_{L2}, \tau_{H2}]$. However, as in the one-dimensional case, windowing the signal does not fully equalize the postcursor SF-ICI. Consequently, the transmit signal in frequency bin $[\tilde{k}_1, \tilde{k}_2]$ can not be estimated from the received data in the

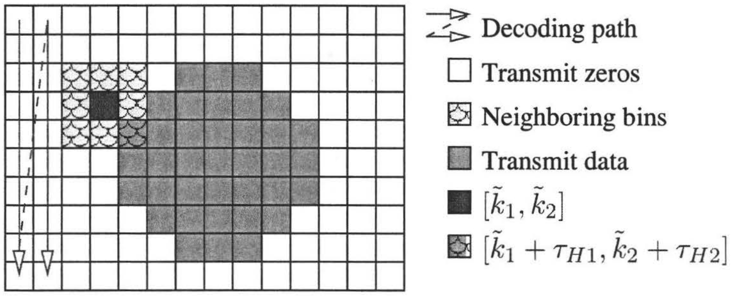

FIGURE 4.18: The decision feedback equalizer is started from the high frequency spectrum, since the transmit data is known to be zero.

corresponding spatial frequency bin. To overcome this problem, the structure of the SDMT signal, and the finite nature of the SF-ICI can be used to implement decision feedback equalization. As in (4.33), the decision feedback equalizer can be described as follows,

$$\hat{X}_T[\tilde{k}_1+\tau_{H1},\tilde{k}_2+\tau_{H2}] = \mathcal{D}^{-1}\left\{ \frac{1}{H[\tilde{k}_1,\tilde{k}_2]U[\tilde{k}_1,\tilde{k}_2;\tilde{k}_1+\tau_{H1},\tilde{k}_2+\tau_{H2}]} \left(X_R[\tilde{k}_1,\tilde{k}_2] - H[\tilde{k}_1,\tilde{k}_2]\sum_{k_1=\tilde{k}_1-\tau_{L1}}^{\tilde{k}_1+\tau_{H1}-1}\sum_{k_2=\tilde{k}_2-\tau_{L2}}^{\tilde{k}_2+\tau_{H2}-1}\hat{X}_T[k_1,k_2]U[\tilde{k}_1,\tilde{k}_2;k_1,k_2]\right)\right\} \tag{4.39}$$

From (4.39), the estimated transmit signal, $\hat{X}_T[\tilde{k}_1+\tau_{H1},\tilde{k}_2+\tau_{H2}]$, is estimated by observing its SF-ICI contribution to the received signal $X_R[\tilde{k}_1,\tilde{k}_2]$. For this approach to work, $\hat{X}$ must be known for all frequencies preceding the spatial frequency bin $[\tilde{k}_1+\tau_{H1},\tilde{k}_2+\tau_{H2}]$ relative to a decoding path. To fulfill this requirement the structure of the SDMT signal can be utilized. In Chapter 2, it was shown that in continuous-tone SDMT modulation, the data is loaded in the low-band spatial frequency spectrum, while zeros are transmitted in the high spatial spectrum. Therefore, the DFE can be started from the high frequency region and ending at the low frequency. Figure 4.18, shows a possible decoding path for a decision feedback equalizer in a 2D channel.

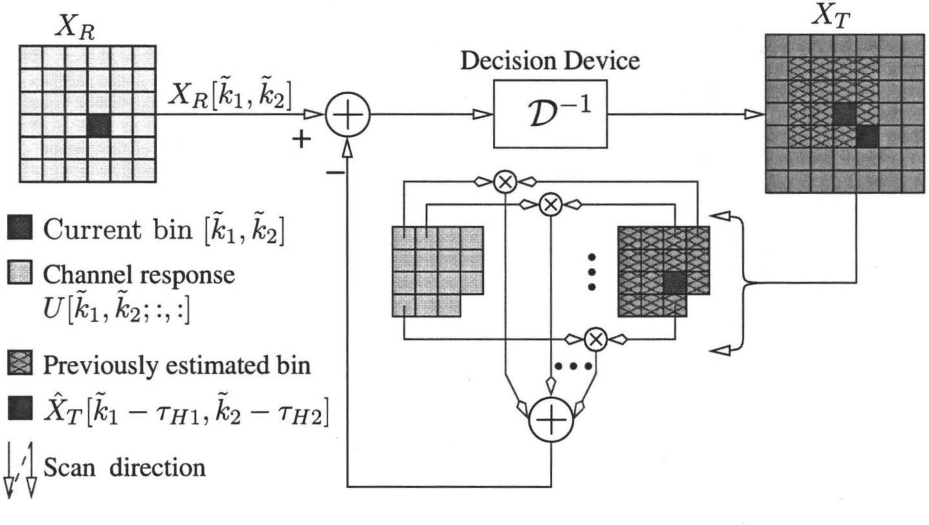

FIGURE 4.19: Decision feedback equalization implemented in a 2D ICI channel. The channel is assumed to be causal in the decoding direction, Moreover, it is has a finite extent.

Figure 4.19 show an illustration of the decision feedback equalizer described in (4.39). From Figure, notice that previously estimated data is used to eliminate their interference from the current received data. The equalized data is then passed though a decision device to estimate the transmit symbol.

In the previous section, two window design criteria, (4.34) and (4.37), were deduced to better the performance of a DFE. These criteria can be extended to the two-dimensional case without loss of generality. The first criterion is to design a window with high SINR. For the two-dimensional case, this ratio is defined as follows,

$$\mathrm{SINR}[\tilde{k}_1, \tilde{k}_2] = \frac{|H[\tilde{k}_1, \tilde{k}_2]U[\tilde{k}_1, \tilde{k}_2; \tilde{k}_1 + \tau_{H1}, \tilde{k}_2 + \tau_{H2}]|^2 \sigma^2_{\tilde{k}_1 + \tau_{H1}, \tilde{k}_2 + \tau_{H2}}}{\sigma^2_{\tilde{\Psi}}[\tilde{k}_1, \tilde{k}_2]} \tag{4.40}$$

The second criterion for a good window design is to ensure that most of the window energy is used in the feedback loop. Mathematically, this criterion can be expressed as follows,

$$\mathrm{FTER}[\tilde{k}_1, \tilde{k}_2] = 1 - \gamma \qquad , \forall [\tilde{k}_1, \tilde{k}_2] \tag{4.41}$$

where,

$$\mathrm{FTER}[\tilde{k}_1, \tilde{k}_2] = \frac{\sum_{k_1=\tilde{k}_1-\tau_{L1}}^{\tilde{k}_1+\tau_{H1}} \sum_{k_2=\tilde{k}_2-\tau_{L2}}^{\tilde{k}_2+\tau_{H2}} |H[\tilde{k}_1, \tilde{k}_2]U[\tilde{k}_1, \tilde{k}_2; k_1, k_2]|^2}{\sum_{k_1=0}^{M_1-1} \sum_{k_2=0}^{M_2-1} |H[\tilde{k}_1, \tilde{k}_2]U[\tilde{k}_1, \tilde{k}_2; k_1, k_2]|^2}, \tag{4.42}$$

is the ratio of the feedback energy used in the DFE approximation to the total energy, and γ is chosen to be small. In general, there is a trade-off between increasing the SINR in (4.40), and using most of the window energy in equalization, as in (4.41). The trade-off arises from the properties of the spatial frequency response of the window. Mainly, the width of the main-lobe, and the attenuation of the side-lobes as discussed in Section 4.3. To satisfy the condition in (4.41), the side lobe attenuation must be high. But as the side lobe attenuation is increased, the width of the main lobe is increased. As the width is increased the energy of the transmit signal is spread over many frequencies, consequently, reducing the SINR in (4.40).

To satisfy the design criteria simultaneously, the class of complex windowing functions is considered. The benefit of using a complex window, is that its spatial frequency response is not symmetric. As a result, it is possible to design a window that can have a good balance between both design criterions. In this work, a heuristic approach was used to design a window suitable for DFE implementation. To design a complex window, the following steps were performed:

Step 1 Choose a real window with high side-lobe attenuation, $\tilde{w}$. In this work, a discrete prolate spheroidal sequence (dpss) window of order five was used. The class of dpss windows was chosen because it represents the windows with the maximal energy concentration in the lobe identified by the order of the window [93, 94]. For example, a dpss window of order zero is a window that has the maximal energy concentration in the main lobe. Figure 4.20(a) illustrates a dpss window of order 5. Figure 4.20(b), shows the spatial frequency response of the dpss window. From the figure, it can be seen that for the DFE approximation,

$\tau_{L1} = \tau_{L2} = 2$ and $\tau_{H1} = \tau_{H2} = 2$. Using this approximation, the SINR is low due to the wide main-lobe and high side-lobe attenuation. However, most of the energy is used in the feedback loop, thus satisfying (4.41).

Step 2 Truncate the spatial frequency response of the real window to get the desired spatial frequency response. Care must be taken when truncating the window since truncation can violate the condition in (4.41). In this work, the desired window response was chosen to be,

$$W[\tilde{k}_1, \tilde{k}_2] = \begin{cases} \widetilde{W}[\tilde{k}_1, \tilde{k}_2] & -3 \leq \tilde{k}_1 \leq 1, -3 \leq \tilde{k}_2 \leq 1 \\ 0 & \text{o.w.} \end{cases} \tag{4.43}$$

where W is the spatial frequency response of the desired complex window, and $\widetilde{W}$ is the spatial frequency response of the chosen real window. Figure 4.20(e) shows the spatial frequency response of the desired windowing function. Notice that the DFE approximation is, $\tau_{L1} = \tau_{L2} = 3$ and $\tau_{H1} = \tau_{H2} = 1$. From (e), notice that the contribution of the desired signal is higher, thus reflecting an increase in the SINR. Notice also, that the condition in (4.41) is still satisfied.

Step 3 Take the inverse discrete Fourier transform of the spatial frequency spectrum of the designed window, W, to obtain a complex windowing function w. Notice that since the truncated response is no longer Hermitian symmetric, the windowing function w is complex. Figures 4.20 (c) and (d), show the real and the imaginary parts of the complex window.

It is important to mention that the complex window designed in this section is not optimal in terms of minimizing the probability of error for a given channel.

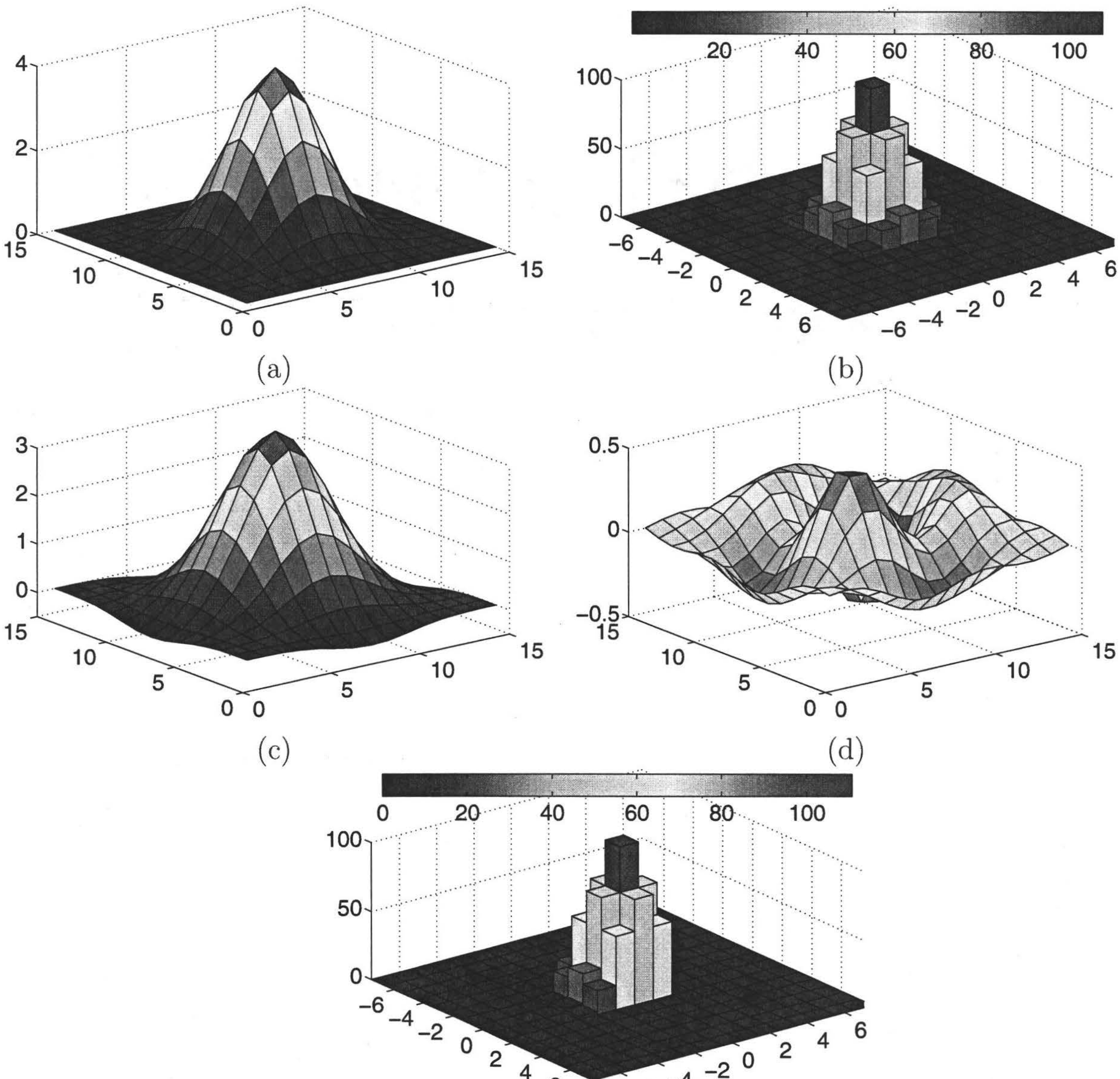

(a) (b) (c) (d) (e)

FIGURE 4.20: An illustration of, (a) Real window $\tilde{w}$, (b) Absolute value of the spatial frequency response of the real window $|\widetilde{W}|$, (c) Real part of the designed complex window $\Re\{w\}$, (d) Imaginary part of the designed complex window $\Im\{w\}$, (e) Absolute value of the spatial frequency response of the complex window $|W|$.

4.5 Simulation Results

In this section, the bit-error rate (BER) for the wireless optical MIMO channel was simulated, and the results are plotted. In the simulation, the BER was evaluated for different magnification levels, and receiver designs. For the first simulation, it is assumed that the receiver implements zero-forcing equalization as in Section 4.4.2. In the second simulation, the receiver makes use of a dpss window of order 2 with decision feedback equalization. For the third simulation, the designed complex window is used in conjunction with the decision feedback equalization as in Section 4.4.3.2.

For all simulations, it is assumed that the transmit frame size, $N_1 \times N_2$, is equal to 16×16 pixels. The sample spacing at the transmitter and receiver are assumed to be same and are equal to unity, i.e. $D_t = D_r = 1$. Furthermore, the average optical power per channel, σ_x^2, was set to 0.2. Noise measurements from [55], where used in the channel simulation. To simulate the bit-error rate, random data were generated and multiplexed into the spatial frequency spectrum using continuous-tone SDMT modulation, as discussed in Chapter 2. The generated transmit frames were magnified to simulate the magnifying effect of the channel. By expressing the transmit image in spatial domain as a sum of weighted sinusoids, magnification can be achieved by scaling the frequency of each sinusoid. The magnified frames were then filtered and multiplied with the corresponding windowing function. A randomly generated white Gaussian noise was generated and added to each frame, and the signal demodulated.

In Figure 4.21, the simulated BER was plotted versus the magnification for different receiver designs. From the figure, notice the oscillating nature of the BER as the magnification is changed. These oscillations are due to variations in the SF-ICI as the magnification is changed. The variations in the SF-ICI level are caused by approximating the period of the transformed images to nearest integer, as in (4.22)

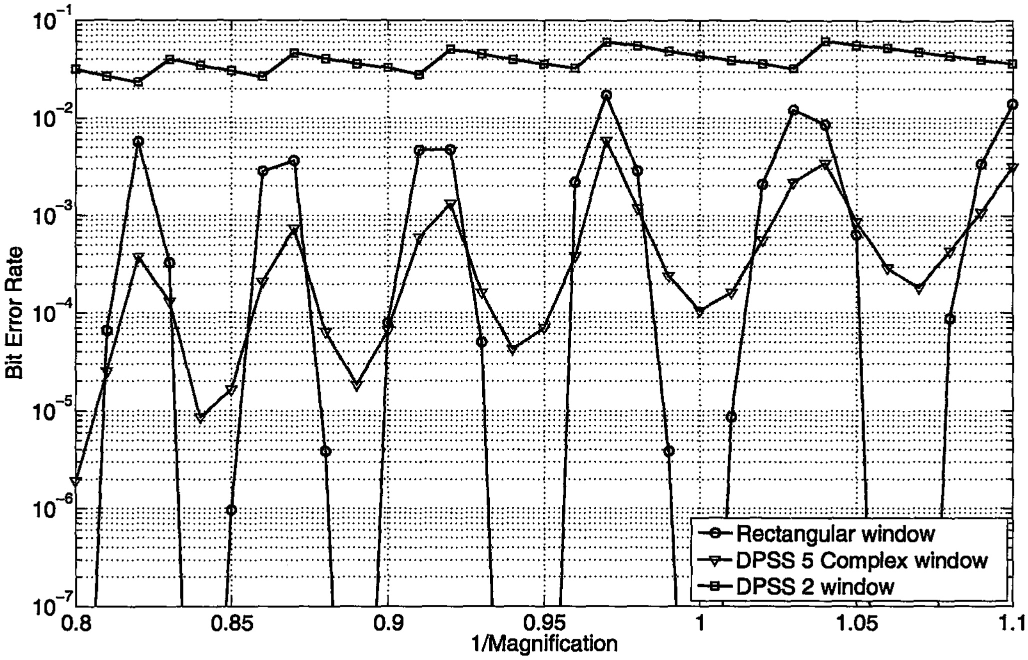

FIGURE 4.21: A comparison between different receiver designs.

and (4.23). Figure 4.22 shows the absolute value of the period approximation error as the magnification is changed. From Figures 4.21 and 4.22, notice the high correlation between the error in the period approximation and the BER. When the magnification is equal to,

$$\hat{\epsilon} = \frac{\text{round}(\epsilon N)}{N}, \qquad N = 16 \tag{4.44}$$

the error in period approximation is zero. This means that the period of the received magnified image is an integer. In this case, the SF-ICI in the channel is low, resulting in a low bit-error rate. However, when the error in approximation is high, the SF-ICI levels are high resulting in a high bit-error rate.

Referring back to Figure 4.21, notice that the BER for zero-forcing equalization with rectangular windowing is sensitive to changes in magnification. The high sensitivity to magnification is attributed to the low feedback to total energy ratio. In zero-forcing equalization, the SF-ICI is assumed to be negligible. However, this assumption does not hold for all values of magnification. Referring back to Figure 4.22,

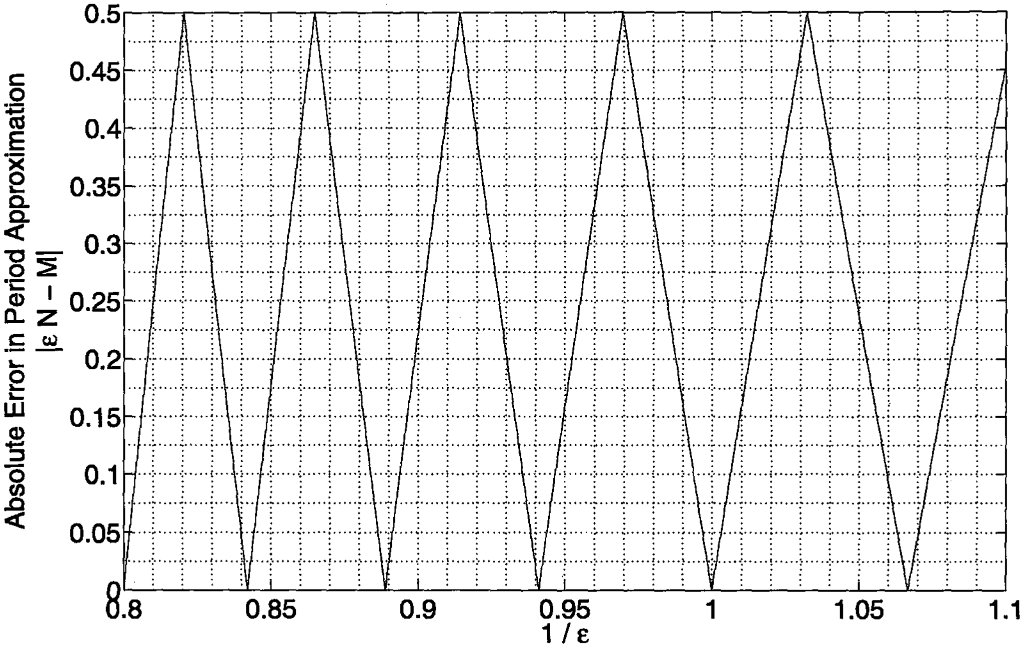

FIGURE 4.22: Absolute error between the integer period approximation, M, and the actual period of the magnified received signal as the magnification is changed.

it can be seen that this assumption only holds when the period of the received signal is closely approximated by an integer, i.e. the error in the period approximation is low, and it is violated otherwise, i.e. when the error in the period approximation is high. For the magnification values where the period of the received signal is closely approximated by an integer, the FTER ratio is high since most of the window energy is concentrated in the frequency bin being equalized. Thus, achieving a low probability of error when demodulating the signal. On the other hand, for values of magnification where the error in period approximation is high, the FTER ratio is low due to the large amount of SF-ICI not used in equalization. The low FTER ratio causes a high probability of error.

For the case of a dpss window of order 2 with decision feedback equalization, the BER is less sensitive to changes in magnification. The low sensitivity to magnification is attributed to high side-lobe attenuation of the chosen window. For a dpss window of order 2, the side-lobes are heavily attenuated, as a result, the SF-ICI in each frequency bin it attributed to a small band of neighboring frequencies. As the magnification is varied, the high side-lobe attenuation maintain the containment of the SF-ICI in a small band around each frequency. Since the SF-ICI is always contained, the application of decision feedback equalization equalizes the majority of the SF-ICI introduced, hence the low sensitivity to changes in magnification. From Figure 4.21 notice that the BER is always high for this system. The high bit-error rate can be explained by the low SINR (4.40). Since the channel SF-ICI is begin equalized by the decision feedback equalizer, the performance of this technique is limited by the channel noise, i.e. for a fixed signal power, the bit-error rate decreases as the channel noise is decreased. Due to the bad performance in terms of low bit-error rate, this window design is not recommended to counter the effects of the magnification in wireless optical MIMO channels.

From Figure 4.21, it can be seen that by changing the windowing function used in decision feedback equalization, the bit-error rate can be lowered drastically. For the complex window design, notice that when the SF-ICI in the channel is low, the bit-error rate is higher than that of the rectangular window with zero-forcing equalization. This is due to the lower SINR used in detecting the signal. For the rectangular window, most of the signal energy is concentrated in one bin. However, for the complex window, the energy of the signal is spread over several bins, as a result reducing the SINR of the data to estimated. But, the SINR in the complex window case is much better that that of the dpss window of the second order. For the values of magnification where the SF-ICI is large, notice that using a complex window with DFE achieves lower probability of error than rectangular windowing with zero forcing equalization. This is due the ability of the DFE to equalize most of the SF-ICI in the channel. From the above discussion, one can say the the performance of the DFE is limited by the channel noise.

Figure 4.23, shows the average ratio of feedback energy used in detection relative to the total energy of the window as the magnification is changed. For a given magnification, this ratio is expressed as,

$$\frac{1}{M_1M_2}\sum_{\tilde{k}_1=0}^{M_1-1}\sum_{\tilde{k}_2=0}^{M_2-1}\sqrt{\mathrm{FTER}[\tilde{k}_1,\tilde{k}_2]} \tag{4.45}$$

where FTER is defined in (4.42).

From Figure 4.21 and Figure 4.23, notice that the energy used in detection is inversely correlated with the BER. This Figure, reflects the effect of SF-ICI equalization of the received signal. For the rectangular window, notice that when the magnification is about 0.915, almost 55% of the signal energy is causing SF-ICI in other frequency bins. Using zero-forcing equalization, the SF-ICI introduced is not equalized, thus causing the high BER. On the other hand, when using DFE with a complex window for the same magnification, only 5% of the SF-ICI is not equalized, hence the lower bit-error rate. Since the performance of the system at this magnification level is limited by the amount of SF-ICI present, i.e. the effect of channel noise is much less than the effect of SF-ICI, the channel is termed a SF-ICI limited channel.

In Figure 4.24, the BER was plotted versus the channel noise for an SF-ICI limited channel. Notice that as the channel noise is decreased, the performance of the designed complex window is improved until it saturates. The saturation is caused by the un-equalized SF-ICI that becomes significant as the noise power is reduced. On the other hand, the performance of the rectangular window does not change due to the presence of large amount of un-equalized SF-ICI.

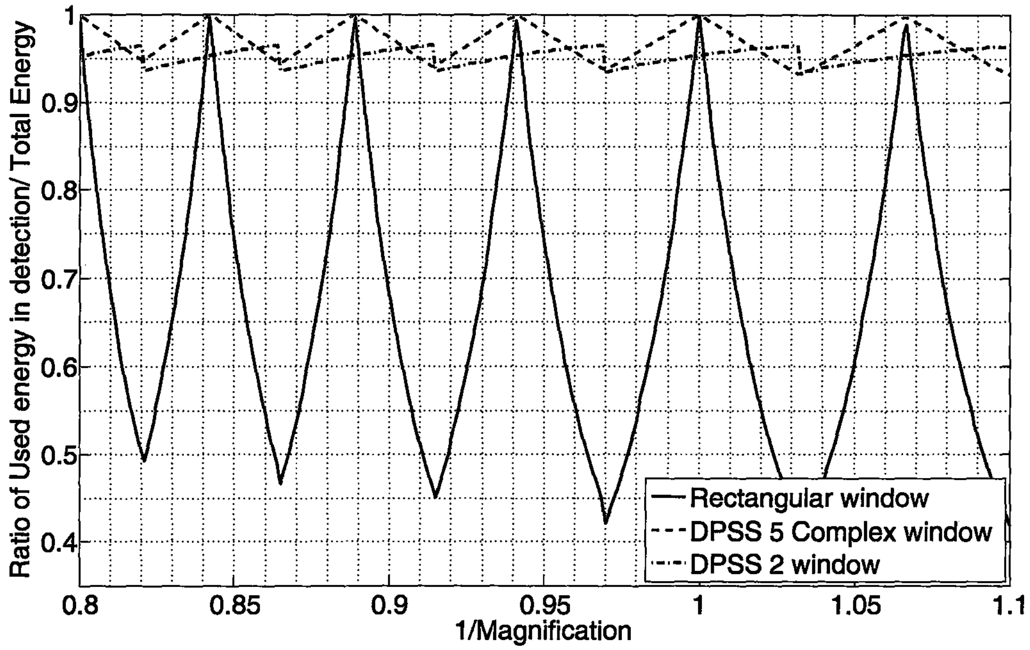

FIGURE 4.23: A plot of the signal energy used in equalization as the magnification is changed.

4.6 Conclusion

In this chapter, the receiver design for wireless optical MIMO channels with magnification is considered. The novelty of this work arise in the consideration of spatial transformations in optical MIMO channels. A model that encompass the effects of magnification and rotation on continuous-tone SDMT modulated frames was derived. From the model, it was shown that magnification and rotation cause spatial frequency varying spatial frequency inter-channel interference. Windowing is introduced as an effective method to equalize the spatial frequency inter-channel interference. To mitigate the effects of magnification on continuous-tone SDMT signaling, two different equalization techniques were devised. The first technique uses zero-forcing equalization with rectangular windowing. The second technique uses a novel complex window design combined with decision feedback equalization. The choice of an equalization

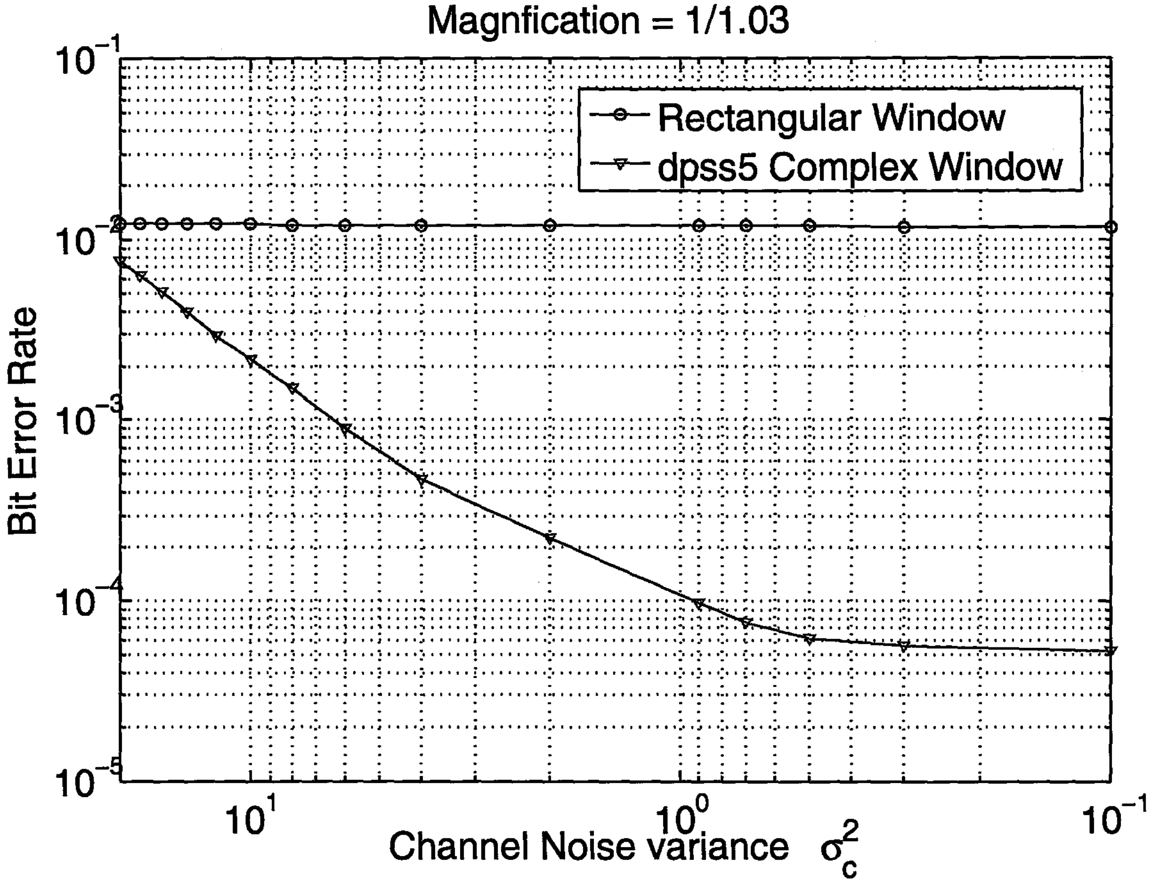

FIGURE 4.24: A comparison between the bit-error rate of decision feedback equalization with a complex window, and a rectangular window with zero-forcing equalization for a SF-ICI limited channel. The magnification, ϵ, is equal to 1/1.03.

technique is directly affected by the channel magnification, and frame size. For magnification values where the channel is limited by the spatial frequency inter-channel interference, decision feedback equalization with a complex windowing is the receiver design of choice since it reduces the bit-error rate. However, for when the channel is noise limited, i.e. the effect of spatial frequency inter-channel interference is negligible, the zero-forcing equalization with rectangular windowing is the best receiver design in terms of low bit-error rate.

It is important to mention that the performance of decision feedback equalization is limited by the design of the windowing function used. In this work, heuristic methods where used to design the windowing function. In a future work, a more rigorous design must be performed to minimize the bit-error rate. Moreover, the receiver design developed in this chapter must be extended to overcome the effects of magnification and rotation on half-toned SDMT modulated frames. Such design could pave the way towards the practical implementation of wireless optical MIMO communication links in many applications.

Chapter 5

Conclusion and Future Work

5.1 Conclusions

The use of multiple transmitters and multiple receivers in the wireless optical channel promise an immense increase in data-rate communication. Although such rates are theoretically possible, their attainment in practice remain illusive. This is mainly due to the complex design of the transmit and receive sides for such a link. The high complexity of the transmitter and receiver, is caused by the algorithms implemented to counter the effects of the channel. Such effects include spatial misalignment between the transmitter and the receiver, and the magnification of transmit frames at the receive side. The work done in this thesis constitute a crucial step towards the practical realization of wireless optical MIMO communication systems. This is done by introducing low complexity designs for both ends of the link. These designs help to enhance the channel capacity and overcome channel impairments.

In the first part of the thesis, two techniques to improve channel capacity for wireless optical MIMO channels are presented. The first technique uses multi-level halftoning to reduce quantization noise power. For quantization noise-limited systems, increasing the number of quantizer levels provides gains in capacity. For example, at a rate of 200fps, a four-level quantizer gives approximately a two-fold increase in capacity over a binary-level quantizer for all frame sizes considered. The second technique uses higher order noise shaping to shape the quantization noise to the out-of-band spatial frequency spectrum, and hence improves capacity. This technique is shown to be useful when the number of levels is small, i.e., near 2.

In the second part of this work, the receiver design was considered for the wireless optical MIMO channel with magnification. In that work, the effects of magnification and rotation in wireless optical MIMO channels were modeled. Different receiver design techniques where discussed. The choice of the receiver used is directly affected by the channel magnification, the frame size, and the channel noise. If the channel is ICI limited, i.e. the error in the period approximation is large. Then, the best design to use is complex windowing with decision feedback equalization. On the other hand, when the channel is channel noise limited, i.e. when the error in the period approximation is small. Then, it is best to use a simple rectangular window with direct detection. Bare in mind that the performance of decision feedback equalization is limited by the design of the windowing function used.

5.2 Future Work

As mentioned previously, the first part of the thesis introduced multi-level halftoned SDMT modulation, while the second part applied DFE with windowing to overcome the effects of magnification. Although both parts were discussed separately, a future work might combine both subjects to realize a more flexible and reliable design. To combine both parts, one might consider applying windowing with decision feedback equalization to a halftoned SDMT modulated signal, instead of its application to the continuous-tone SDMT signal presented in this work.

Through out this work, the inverse discrete Fourier transform was used to generate transmit frames based on SDMT modulation. In a future work, a study of other transforms is required. The use of other transforms to move from spatial frequency to spatial domain might introduce a benefit in reducing the overall system complexity, and increase its robustness. Moreover, the structure of these transforms can potentially be used to reduce the complexity of equalizing the received signal at the receiver.

In the first part of the thesis, the aggregate channel capacity was maximized with respect to the filter parameters. For this optimization problem, the error diffusion filter was assumed to be symmetric. In a future work, one might consider the general case of a non-symmetric filter design. Such a filter design might achieve a higher gain in the channel capacity. One might also consider, the joint optimization problem pertaining to the maximization of the aggregate channel capacity with respect to the error diffusion filter as well as the power allocation matrix.

For the first part of the thesis, gains in channel capacity were achieved by using multi-level halftoned SDMT, instead of binary halftoned SDMT. It is important to note that these promised rates can only be achieved if coding is applied. For a future work, one can consider the design of a capacity achieving code for such a channel. Due to the large number of transmit and receive elements in such a channel, the designed code should have low complexity to allow practical implementation.

In the second part of this work, decision feedback equalization with windowing was implemented to reduce the effect of magnification on the continuous-tone SDMT signal. A future work might consider extending this technique to other types of impairments. Such impairments include rotation and projective distortion. Signal rotation, and projective distortions constitute a serious problem in an in-door wireless optical MIMO communication environment. To apply such techniques, the model derived in this work, need to be extended to account for projective distortion. The resulting model can then be used to design windowing functions that are suitable for DFE implementation. In this work, a heuristic approach was used to design the windowing function. In a subsequent work, a more rigorous design is needed to realize further reductions in the bit error rate.

In the work presented, it was assumed that there is one user transmitting information across the wireless optical MIMO channel. For a subsequent work, one might extend this work to multiple users. This is done by considering the use of spatiotemporal multiplexing techniques. The development of such multiplexing technique will pave the way towards the integration of wireless optical MIMO communication systems, with existing multimedia display technology. For example, it would be possible to use a television set to download information while watching the box.

Another possible direction is to apply SDMT modulation and the detection techniques devised to the coherent channel. Such a channel is present in holographic data storage systems. In a coherent channel, it is known that the Fourier transform and its inverse can be computed optically via a lens. Such a property can be advantageous when applying SDMT modulation to such a channel. Since the optical implementation of the Fourier transform, and its inverse, is much faster compared with the electrical domain implementation. As a result, the computational complexity of this modulation technique is reduced by many folds, thus, making it an attractive choice for many future applications.

Another potential application is the use of wireless optical MIMO systems in free space optical links. So far, the use of wireless optical MIMO in free space optical channels has been limited to a few transmitters and receivers. In the future, it might be advantageous to use large scale wireless optical MIMO links to communicate mass amount of data in metropolitan areas. For such links, large LED billboards can be used to transmit information. The receiver can use an imaging sensor with telescope optics. For this channel magnification, rotation and projective distortions can affect the transmit signal. As a result, the techniques developed in this thesis can be adapted for the use in such a channel.

Appendix A

Mathematical Proofs

In this chapter, a mathematical proof for the following theorem is derived. The theorem states that "A symmetric negative semi-definite matrix Q, with a zero diagonal element must have zeros in the corresponding row and column". Before the proof is presented, some definitions and lemmas are states and proofed. These definitions are then used to prove the stated theorem.

Definition A.1. A square matrix Q is symmetric if

$$Q^T = Q$$

Definition A.2. A square matrix Q is negative semi-definite if and only if

$$x^T Q x \leq 0, \qquad \forall x$$

Definition A.3. If Q is a matrix of size $n \times n$, then, a ***principal sub-matrix*** Q_p is constructed from Q by deleting any $n - m$ rows, and their corresponding columns. Where Q_p is a matrix of size $m \times m$.

Lemma A.4. *If Q is negative semi-definite matrix of size $n \times n$, then, all its diagonal elements must be non-positive, that is, $q_{ii} \leq 0$.*

Proof. The proof follows directly from Definition A.2 by substituting the following value for x^T,

$$x^T = \left[\underbrace{0\,0\,0\ldots0}_{i-1}\quad \underset{i^{th}}{\overset{1}{\uparrow}}\quad \underbrace{0\,0\ldots0}_{n-i}\right]$$

$\square$

Lemma A.5. *If a matrix Q is symmetric and negative semi-definite, then the following inequality is satisfied,*

$$q_{ii} + q_{jj} \leq 2q_{ij}$$

Proof. The proof follows directly from Definition A.2 by substituting the following value for x^T,

$$x^T = \left[\underbrace{0\,0\ldots0}_{i-1}\quad \underset{i^{th}}{\overset{1}{\uparrow}}\quad \underbrace{0\,0\ldots0}_{j-i-1}\quad \underset{j^{th}}{\overset{-1}{\uparrow}}\quad \underbrace{0\,0\ldots0}_{n-j}\right]$$

$\square$

Lemma A.6. *A principle sub-matrix Q_p of a negative semi-definite matrix Q, is also negative semi-definite.*

Proof. To prove the lemma, the following value of x^T is substituted in Definition A.2,

$$x^T = \left[\underbrace{0\,0\ldots0}_{i-1}\quad \underset{i^{th}}{\overset{\alpha}{\uparrow}}\quad \underbrace{0\,0\ldots0}_{j-i-1}\quad \underset{j^{th}}{\overset{\beta}{\uparrow}}\quad \underbrace{0\,0\ldots0}_{n-j}\right]$$

To get the following,

$$\begin{aligned}
x^T Q x &\leq 0 \\
\alpha^2 q_{ii} - \alpha\beta q_{ij} - \alpha\beta q_{ji} + \beta^2 q_{jj} &\leq 0 \\
\underbrace{\begin{bmatrix} \alpha & \beta \end{bmatrix}}_{x_p^T} \underbrace{\begin{bmatrix} q_{ii} & q_{ij} \\ q_{ji} & q_{jj} \end{bmatrix}}_{Q_p} \underbrace{\begin{bmatrix} \alpha \\ \beta \end{bmatrix}}_{x_p} &\leq 0 \\
x_p^T Q_p x_p &\leq 0
\end{aligned}$$

where Q_p is a principal sub-matrix of Q. □

Theorem A.7. *A symmetric negative semi-definite matrix Q, with a zero diagonal element must have zeros in the corresponding row and column.*

Proof. The proof follows directly from Lemma A.6. Since Q is a negative semi-definate matrix, then its principal sub-matrix is also negative semi-definite i.e.,

$$x_p^T Q_p x_p \leq 0$$

where Q_p is constructed as follows,

$$Q_p = \begin{bmatrix} q_{ii} & q_{ij} \\ q_{ji} & q_{jj} \end{bmatrix}$$

The principal sub-matrix, Q_p is negative semi-definite if and only if its eigenvalues are non-positive,

$$\lambda \leq 0$$

The eigenvalues for the principal sub-matrix are computed by solving the characteristic equation,

$$\begin{aligned} \det(\lambda I - Q_p) &= 0 \\ (\lambda - q_{ii})(\lambda - q_{jj}) - q_{ij}q_{ji} &= 0 \end{aligned}$$

Assuming that the diagonal element q_{ii} is zero, then the eigenvalues are given by,

$$\lambda = \frac{q_{jj} \pm \sqrt{q_{jj}^2 + 4q_{ij}q_{ji}}}{2}$$

Since the eigenvalues must be non-positive, the following condition can be obtained,

$$\{\lambda_1 = q_{jj} + \sqrt{q_{jj}^2 + 4q_{ij}q_{ji}} \leq 0\} \longrightarrow 4q_{ij}q_{ji} \leq 0$$

Since the matrix is symmetric $q_{ij} = q_{ji}$, the inequality can be rewritten as follows,

$$4q_{ij}^2 \leq 0$$

Notice that the inequality is satisfied if and only if $q_{ij} = q_{ji} = 0$. □

Bibliography

[1] Online barcode generator. http://www.terryburton.co.uk/barcodewriter/generator/, 12 September 2008.

[2] S. Boyed and L. Vandenberghe. *Convex Optimization.* Cambridge University Press, 2004.

[3] T. G. Zimmerman. "Personal Area Networks: Near-field Intrabody Communication". *IBM Systems*, 35(3-4):609–617, 1996.

[4] Summit Technical Media. "What is a Personal Area Network (PAN)? ". *High Frequency Electronics*, March 2004.

[5] L. Zhong, M. Sinclair, and N. K. Jha. "A Personal-Area Network of Low-power Wireless Interfacing Devices for Handhelds: System and Hardware Design ". In *MobileHCI'05*, Salzburg, Austria, September 19–22 2005.

[6] Wikipedia. http://en.wikipedia.org/bluetooth, 21 August 2008.

[7] S. Cherry. "Wi-Fi taken on Bluetooth". *IEEE Spectrum*, 45(8):14, August 2008.

[8] IEEE Computer Society / LAN/MAN Standards Committe. *"IEEE 802.11g-2003: Further Higher Data Rate Extension in the 2.4 GHz Band"*. 3 Park Avenue, New York, NY, USA, 27 June 2003.

[9] F. R. Gfeller and U. Bapst. "Wireless In-House Data Communication via Diffuse Infrared Radiation". *Proceeding of IEEE*, 67(11):1474–1486, November 1979.

[10] J. R. Barry, J. M. Khan, E. A. Lee, and D. G. Messerschmitt. "High-Speed Nondirective Optical Communication for Wireless Networks". *IEEE Network Magazine*, pages 44–54, November 1991.

[11] E. Teletar. "Capacity of Multi-antenna Gaussian Channels". *European Transactions on Telecommunications*, 10(6):585–595, 1999.

[12] Y. Xiao. "IEEE 802.11n : Enhancements For Higher Throughput in Wireless LANs". *IEEE Wireless Communications*, 12(6):82–91, December 2005.

[13] C. Gomes-Calero, L. Garcia-Garcia, R. Martinez, and L. de Haro. "Comparison of antenna configurations in different scenarios using a wideband MIMO testbed". *IEEE Antennas and Propagation Society International Symposium*, pages 301–304, 9-14 July 2006.

[14] Ramakrishna Janaswamy. "Effect of Element Mutual Coupling on the Capacity of Fixed Length Linear Arrays". *IEEE Antennas and Wireless Propagation Letters*, 1:157–160, 2002.

[15] Da shan Shiu, Gerard J. Foschini, Michael J. Gans, and Joseph M. Kahn. "Fading Correlation and Its Effects on the Capacity of Multi-Element Antenna Systems". *IEEE Transactions on Communications*, 48:502–513, 2000.

[16] Chen-Nee Chuah, David N. C. Tse, Joseph M. Kahn, and Reinaldo A. Valenzuela. "Capacity Scaling in MIMO Wireless Systems Under Correlated Fading". *IEEE Transactions on Information Theory*, 48(3):637–650, March 2002.

[17] Andreas F. Molisch, Martin Steinbauer, Martin Toeltsch, Ernst Bonek, and Reiner S. Thoma. "Capacity of MIMO Systems Based on Measured Wireless Channels". *IEEE Journal on selected areas in communications*, 20(3):561–569, April 2002.

[18] W. Yadum and N. Nakajima. “The correlation of diversity/MIMO antenna for portable terminals”. *Wireless Communications and Mobile Computing*, 7(8): 995–1002, 16 May 2007.

[19] S. Hranilovic and F. R. Kschischang. “Optical Intensity-Modulated Direct Detection Channels: Signal Space and Lattice Codes”. *IEEE Transactions on Information Theory*, 49(6):1385–1399, June 2003.

[20] *“IEC 60825-1, Safety of Laser Products - Part 1: Equipment classification, requirements, and user’s guide”*. International Electrotechnical Commission (IEC), 1.2 edition, 2001.

[21] R. M. Shelby, J.A. Hoffnagle, G. W. Burr, C. M. Jefferson, M. P. Bernal, H. Coufal, R.K.Grygier, R.M.Macfarlane, and G.T. Sincerbox. “Pixel-matched holographic data storage with megabit pages”. *Optics Letters*, 22(19):1509–1511, October 1997.

[22] G. W. Burr, J.Ashley, H. Coufal, R.K.Grygier, J.A.Hoffnagle, C.M.Jefferson, and B.Marcus. “Modulation coding for pixel-matched holographic data storage”. *Optics Letters*, 22(9):639 – 641, May 1997.

[23] S. Nabavi and B. V. K. V. Kumar. “Detection methods for holographic data storage”. In *Proceedings of the IEEE Optical Data Storage*, pages 156–158, Montreal, QC, Canada, April 2006.

[24] D. V. Plant and A. G. Kirk. “Optical interconnects at the chip and board level: Challenges and Solutions”. *Proceeding of the IEEE*, 88(6):806–818, 2000.

[25] J. Bristow, J. Lehman, M. Hibbs-Brenner, and Yue Liu. “Applying optical interconnects to electronic systems: Promise vs. practicality”. *Proceedings of the Fourth International Conference on Massively Parallel Processing Using Optical Interconnections.*, pages 54 – 59, 22-24 June 1997.

[26] R. Villn, S. Voloshynvskiy, O. Koval, and T. Pun. "Multilevel 2-D bar codes: Towards high capacity storage modules for multimedia security and management". *IEEE Transactions on Information Forensics and Security*, 1(4):405–420, December 2006.

[27] W. Claycomb and D. Shin. "Using a two dimensional colorized barcode solution for authentication in pervasive computing". In *Proceeding of IEEE ACS/ IEEE International Conference on Pervasive Services*, pages 173–180, Lyon, France, June 26-29 2006.

[28] J. M. Kahn and J. R. Barry. "Wireless infrared commnications". *Proceedings of the IEEE*, 85(2):263 – 298, February 1997.

[29] D. C. O'Brien, S.Quasem, S.Zikic, and G.E.Faulkner. "Multiple input multiple output systems for optical wireless: Challenges and possibilities". *Proceeding of SPIE*, 6304, 2006.

[30] S. Hranilovic and F. R. Kschischang. "A pixelated MIMO wireless optical communication system". *IEEE journal of Selected Topics in Quantum Electronics*, 12(4):891–895, July / August 2006.

[31] Mohamed D. A. Mohamed and S. Hranilovic. "Two-Dimensional Binary Halftoned Optical Intensity Channels". *IET Communications*, 2(1):11–17, January 2008.

[32] D. Psaltis and G.W. Burr. "Holographic Data Storage". *Computer*, 31(2):52–60, February 1998.

[33] H. Coufal. "Holographic Data Storage or reliability; a status report". In *Optical Data Storage Topical Meeting, 1997. ODS. Conference Digest*, pages 46–47, 7-9 Apr 1997.

[34] InPhase Technologies. http://www.inphase-technologies.com, 2007.

[35] J. F. Heanue, M.C. Bashaw, and L. Hesselink. " Volume Holographic Storage and Retreival of Digital Data". *Science*, 265(5173):749–752, August 1994.

[36] S. S. Orlov, W. Phillips, E. Bjornson, L. Hesselink, and R. Okas. "10 Gigabit/second Sustained Optical Data Transfer Rate From a Holographic Disk Digital Data Storage System". *Presented at the OSA Annual Meeting 2000, Paper MK3.*, 2000.

[37] S. S. Orlov. "Volume holographic data storage". *Communications of the ACM*, 43(11):46–54, 2000.

[38] K. Anderson, E. Fotheringham, A. Hill, B. Sissom, and K. Curtis. "High speed holographic data storage at 500 Gbit/in^2". *InPhase Technologies Whitepapers*, 2006.

[39] J. Ashley, M.P. Bernal, G. W. Burr, H. Coufal, H. Guenther, J. A. Hoffnagle, C. M. Jefferson, B. Marcus, R. M. Macfarlane, R. M. Shelby, and G. T. Sincerbox. "Holographic Data Storage". *IBM Journal of Research and Development*, 44(3): 341–368, May 2000.

[40] E. Bisaillon, D. F. Brosseau, T. Yamamato, M. Mony, E. Bernier, D. Goodwill, D. V. Plant, and A. G. Kirk. "Free-space optical link with spatial redundancy for misalignment tolerance". *IEEE Photonic Technology Letters*, 14(4):859–874, 2002.

[41] J. F. Heanue, K. Gurkan, and L. Hesselink. "Signal Detection for Page-access Optical Memories with Inter symbol Interference". *Journal of Applied Optics*, 35(14):2431–2438, 10 May 1996.

[42] J. K. Nelson, A. C. Singer, and U. Madhow. "Multi-directional Decision Feedback for 2D Equalization". *Proceedings of IEEE International Conference on Acoustics, Speech, and Signal Processing.*, 4:iv (921–924), 17-21 May 2004.

[43] C. Y. Chen and T. D. Chiueh. "A Low-Complexity High-Performance Modulation Code for Holographic Data Storage". In *14th IEEE International Conference on Electronics, Circuits and Systems*, pages 788–791, 11-14 December 2007.

[44] M. Ayres, A. Hoskins, and K. Curtis. "Image oversampling for page-oriented optical data storage ". *Applied Optics*, 45(11):2459 – 2464, 10 April 2006.

[45] H. Ohtoh and M. Yamamoto. "Data Position Detection Analysis for 1.X time Oversampled Image in Holographic Data Storage". In *Conference on Lasers and Electro-Optics*, pages 1–2, Pacific Rim, 26-31 August 2007.

[46] D. A. B. Miller. "Rationale and Challenges for Optical Interconnects to Electronic Chips ". *Proceedings of IEEE*, 88(6):728–749, June 2000.

[47] D. Lammers. "Intel prepares for optical-interconnect future". EE Times, 3 August 2004.

[48] D. V. Plant, B. Robertson, H. S. Hinton, M. H. Ayliffe, G. C. Boisset, W. Hsiao, D. Kabal, N. H. Kim, Y. S. Liu, M. R. Otazo, D. Pavlasek, A. Z. Shang, J. Simmons, K. Song, D. A. Thompson, and W. M. Robertson. "4 x 4 vertical-cavity surface-emitting laser (VCSEL) and metal–semiconductor–metal (MSM) optical backplane demonstrator system". *Applied Optics*, 35(32):6365–6368, 1996.

[49] D. V. Plant, M. B. Venditti, E. Laprise, J. Faucher, K. Razavi, M. Chateauneuf, A. G. Kirk, and J. S. Ahearn. " 256-channel bidirectional optical interconnect using VCSELs and photodiodes on CMOS". *Journal of Lightwave Technology*, 19(8):1093–1103, August 2001.

[50] M. Naruse, S. Yamamoto, and M. Ishikawa. "Real-Time Active Alignment Demonstration for Free-Space Optical Interconnections". *IEEE Photonic Technology Letters*, 13(11):1257–1259, November 2001.

[51] Wikipedia. http://en.wikipedia.org/wiki/barcode, 11 September 2008.

[52] Steve Hranilovic. *Wireless Optical Communication Systems.* Springer, 2004.

[53] Texas Instruments. "Digital Light Projection". http://www.dlp.com/, 11 September 2008.

[54] D. Dudley, W. Duncan, and J. Slaughter. "Emerging Digital Micromirror Device (DMD) Applications ". *Proceeding of SPIE*, 4985, 2003.

[55] Mohamed D. A. Mohamed, A.Dabbo, and S. Hranilovic. "MIMO Optical Wireless Channel Using Halftoning". In *IEEE International Conference on Communications ICC*, pages 1306–1364, Beijing, China, May 2008.

[56] Daisuke Takase and Tomoaki Ohtsuki. "Spatial Multiplexing in Optical Wireless MIMO Communications Over Indoor Enviroment". *The Institute of Electronic, Information, and Communication Engineers (IEICE) Transactions*, E89-B(4): 1364–1371, April 2006.

[57] A. Dabbo and S. Hranilovic. "Multilevel error diffusion for wireless optical MIMO channels". In *24th Biennial Symposium on Communications*, pages 208–211, June 2008.

[58] Y. Ishii. "The World of Liquid-Crystal Display TVs—Past, Present, and Future". *Journal of Display Technology*, 3(4), December 2007.

[59] W. Kowalsky, E. Becker, T. Benstem, T. Dobbertin, D. Heithecker, H.-H. Johannes, D. Metzdorf, and H. Neuner. " OLED matrix displays: technology and fundamentals". *First International IEEE Conference on Polymers and Adhesives in Microelectronics and Photonics*, pages 20–28, 21-24 October 2001.

[60] BOSLab Research Group, Kent State University. "Liquid Crystal on Silicon Devices". http://www.lci.kent.edu/boslab/projects/lcos/, 2008.

[61] Alexander Hornberg, editor. *Handbook of Machine Vision.* Wiley-VCH, 2006.

[62] J. Goodman. *Introduction to Fourier Optics.* McGraw - Hill, 1st edition, June 1968.

[63] Kent H. Lundberg. "Noise Sources in Bulk CMOS". Unpublished, 2002.

[64] Hewlett-Packard Components Group. "Noise Sources in CMOS Image Sensors". *Imaging Products Operations*, 1998.

[65] Jonathan J. Ashely and Brian H. Marcus. "Two-Dimensional Low-Pass Filtering Codes". *IEEE Transactions on Communications*, 46(6):724–727, June 1998.

[66] Dhawat E. Pansatiankul and Alexander A. Sawchuk. "Fixed-length two-dimensional modulation coding for imaging page-oriented optical data storage systems". *Applied Optics*, 42(2):275–290, 10 January 2003.

[67] Dhawat E. Pansatiankul and Alexander A. Sawchuk. "Variable-Length Two-Dimensional Modulation Coding for Imaging Page-Oriented Optical Data Storage Systems". *Applied Optics*, 42(26):5319–5333, 10 September 2003.

[68] S. Hranilovic and F. R. Kschischang. "Short-range wireless optical communication using pixilated transmitters and imaging receivers". In *Proceedings of the IEEE International Conference on Communications*, volume 2, pages 891 – 895, Paris, France, June 2003.

[69] Simon Haykin. *Communication Systems.* Wiley, 4th edition, 2001.

[70] J. M. Cioffi. "A Multicarrier Primer". *ANSI Contribution T1E1.4/91-157*, November 1991.

[71] J. R. Barry, E. A. Lee, and D. G. Messerschmitt. *Digital Communication.* Kluwer Academic Publishers, third edition, 2004.

[72] B. Hirosaki. "An Orthogonally Multiplexed QAM System Using the Discrete Fourier Transform". *IEEE Transactions on Communications*, COM-29(7):982–989, 1981.

[73] A. Peled and A. Ruiz. "Frequency domain data transmission using reduced computational complexity algorithms". *Proceeding of the IEEE Int. Conf. Acoustics, Speech, and Signal Processing*, 5:964–967, 9-11 April 1980.

[74] J. Tellado. *Multicarrier modulation with low PAR: applications to DSL and wireless.* Kluwer Academic Publishers, MA, USA, 2000.

[75] R.G. Gallager. *"Information Theory and Reliable Communication"*. Wiley, New York, 1968.

[76] NEC Inc. http://www.nec.com/, .

[77] Mikrotron GmbH. http://www.mikrotron.de/, .

[78] Matrox Imaging. http://www.matrox.com/., .

[79] NorPix Inc. http://www.norpix.com/, .

[80] National Instruments Inc. http://www.ni.com/, .

[81] R. Ulichney. *Digital Halftoning.* MIT press, Cambridge, MA, USA, 1987.

[82] R. W. Floyed and L. Steinberg. "An adaptive algorithm for spatial gray scale". *Proceedings of the Society of Information Display*, 17:75–77, 1976.

[83] T. Kite, B. Evans, and A. Bovik. "Digital Halftoning as 2-D Delta-Sigma Modulation". *Proceedings of the International Confirence on Image Processing*, 1: 799–802, 26-29 October 1997.

[84] A. B. Sripad and D. L. Snyder. "A necessary and sufficient condition for quantization errors to be uniform and white". *IEEE Transactions on Acoustics, Speech, and Signal Processing*, ASSP-25:442–448, October 1977.

[85] D. A. Jones and K. W. Martin. *Analoge Intergrated Circuit Design.* John Wiley and Sons, November 1996.

[86] S. R. Norsworthy, R. Schreier, and G. C. Temes. *Delta-Sigma Data Converters: Theory, Design, and Simulation.* Wiley IEEE press, NY, USA, October 1996.

[87] Sasan H. Ardalan and John J. Paulos. " An Analysis of Nonlinear Behavior in Delta-Sigma Modulators". *IEEE Transactions on Circuits and Systems*, CAS-34 (6), 1987.

[88] Richard Schreier. "An Empirical Study of High-Order Single-Bit Delta-Sigma Modulators". *IEEE Transactions on Circuits and Systems*, 40(8):461–466, August 1993.

[89] Soren Hein and Avideh Zakhor. "On the Stability of Sigma Delta Modulators". *IEEE Transactions on Signal Processing*, 41(7):2322–2348, July 1993.

[90] Mathworks Inc. Matlab version 7.1.0.183, optimization toolbox version 3.0.3, 2006.

[91] A. V. Oppenhiem, Schafer R. W, and J. R. Buck. *Discrete-Time Signal Processing.* Prentice Hall, NJ, USA, second edition, 1998.

[92] H. Nyquist. "Certain Topics in Telegraph Transmission Theory". *Proceeding of IEEE*, 90(2):280–305, February 2002.

[93] Donald W. Tufts and James T. Francis. "Designing digital low-pass filters–Comparison of some methods and criteria". *IEEE Transactions on Audio and Electroacoustics*, 18(4):487–494, December 1970.

[94] John D. Mathews, J. K. Breakall, and George K. Karawas. "The discrete prolate spheroidal filter as a digital signal processing tool". *IEEE Transactions on Acoustics, Speech, and Signal Processing*, ASSP-33(6):1471–1478, December 1985.

1703 22